Interface Design for Silicon-based Anodes for Lithium-ion Batteries

by

Hongzheng Zhu

A THESIS SUBMITTED IN PARTIAL FULFILLMENT OF

THE REQUIREMENTS FOR THE DEGREE OF

DOCTOR OF PHILOSOPHY

in

THE COLLEGE OF GRADUATE STUDIES

(Mechanical Engineering)

THE UNIVERSITY OF BRITISH COLUMBIA

(Okanagan)

November, 2021

The following individuals certify that they have read, and recommend to the College of Graduate

Studies for acceptance, a thesis/dissertation entitled:

Interface Design for Silicon-based Anodes for Lithium-ion Batteries

submitted by Hongzheng Zhu in partial fulfillment of the requirements of

the degree of Doctor of Philosophy.

Dr. Jian Liu, School of Engineering

Supervisor

Dr. Lukas Bichler, School of Engineering

Supervisory Committee Member

Dr. Dimitry Sediako, School of Engineering

Supervisory Committee Member

Dr. Liwei Wang, School of Engineering

University Examiner

Dr. Douglas Ivey, Dept. Chemical/Materials Engineering, University of Alberta

External Examiner

Abstract

Lithium-ion batteries (LIBs) are promising energy storage systems for electric vehicles (EVs) and hybrid electric vehicles (HEVs). However, to meet the requirements for EVs and HEVs, the performance of commercially available LIBs needs to be greatly improved in energy density, cycling life, rate capability, and safety. It is well known that the LIB performance is highly dependent on the choice of electrode materials. Therefore, it is essential to develop new electrode materials as replacements for graphite anode used in commercial LIBs to achieve high-performance LIBs desirable for EV and HEV applications. Among all potential alternatives to graphite anode, Si-based materials are considered one of the most promising anodes due to their superior gravimetric capacity (4200 mAh g^{-1}) and moderate discharge voltage. However, Si electrodes face several challenging issues, such as large volume changes, thick solid electrolyte interphase (SEI) layer, and electrode swelling. Hence, solving the above problems is crucial for enhancing the overall performance of Si anodes in LIBs for further practical applications.

In this thesis, different coating materials were used to modify Si anode to achieve the above goal. Firstly, a facile and low-cost sol-gel method followed by annealing was developed to form a thin Al_2O_3 coating layer on the graphite/silicon composite anode. At 25 ^{o}C, the Al_2O_3-coated graphite/silicon (G/Si) electrode showed better cycling performance than the uncoated samples. The capacity retention could retain the initial capacity up to 76.4% after 100 cycles, while the uncoated G/Si could only reach 56.4%. Secondly, AlO_xN_y coating by plasma-enhanced atomic layer deposition (PEALD) was developed and applied on the Si electrode. By employing this as a surface modification, the confinement of silicon nanoparticles embedded into the electrode matrix is well achieved, while the kinetics of the charge/discharge process is enhanced due to the electrochemical properties of the AlO_xN_y film. The capacity retention of AlO_xN_y

coated Si electrode was elevated to 72.3% (compared with 13.3% of bare Si electrode), and the capacity remains 1297.2 mAh g^{-1} at 140 cycles. Thirdly, a new hybrid organic-inorganic material, tincone, was developed by molecular layer deposition (MLD), and successfully applied the tincone as a surface coating on the Si electrode. The tincone coating showed excellent protective effects on Si anode. Tincone-coated Si electrode exhibited a discharge capacity of 2487.3 mAh g^{-1} with 70% of capacity retention after 110 cycles. Meanwhile, tincone film possessed good electrochemical activity for Li storage, making it a new organic-inorganic hybrid material in Li-ion batteries.

In summary, this thesis developed three novel materials and processes for surface coating in LIBs, applied these coating materials to engineer electrode-electrolyte interfaces of Si-based anodes, and deepened fundamental understanding of nanoscale surface coating in addressing the problems in Si anodes. It is expected that this research could contribute to the development of a commeically-viable Si anode for higher-energy LIBs for electric vehicle applications.

Lay Summary

Silicon is considered a promising alternative anode material to commercial graphite for lithium-ion batteries (LIBs) due to its high theoretical capacity, low working voltage, and large abundance. However, Si suffers from mechanical pulverization, thick solid-electrolyte-interphase formation, and rapid performance decay in LIBs, resulting from the vast volume change of up to 400% during the Li alloying-dealloying process. To address these challenges, three different surface coating materials (Al_2O_3, AlN_xO_y, and tincone) and methods were developed and applied to modify the Si-based electrode. It was found that surface coating with nanoscale thicknesses (~ 2-10 nm) could significantly improve the cycling stability, efficiency, and lifetime of Si-based anode at both room temperature and high working temperature (55 °C). The main reasons were attributed to suppressed side reactions between Si and the electrolytes, stabilized solid electrolyte interphase, and reduced electrode swelling. The developed surface coating materials are expected to enable high-performance Si anode for high-energy next-generation LIBs for electric vehicles.

Preface

All chapters in the thesis are based on work conducted in UBCO's Advanced Materials for Energy Storage Laboratory by Hongzheng Zhu under the supervision of Dr. Jian Liu. During the whole experiments in the thesis, I was responsible for the majority of the sample preparation and data analysis. The contributions of the main collaborators to each work are described below. My supervisor, Dr. Jian Liu, and the committee members were mentoring and leading me through the thesis direction. A list of any publications arising from work presented in the thesis and the chapters in which the work is located are as follows:

1. Chapter 3: "Facile and Low-Cost Al_2O_3 Coating as an Artificial Solid Electrolyte Interphase Layer on Graphite/Silicon Composites for Lithium-Ion Batteries", Hongzheng Zhu, Mohammad Hossein Aboonasr Shiraz, Liang Liu, Yuhai Hu, Jian Liu. Nanotechnology, 32(14), 144001, 2021.

   Hongzheng Zhu fabricated coating on Si-based electrode completed structural and electrochemical characterizations and manuscript writing; Mohammad Hossein Aboonasr Shiraz, Liang Liu, and Yuhai Hu helped in revising the paper; Jian Liu oversaw and guided the project.

2. Chapter 4: "Atomic Layer Deposited AlO_xN_y Coating for High-Performance Si Anode in Lithium-Ion Batteries", Hongzheng Zhu, Mohammad Hossein Aboonasr Shiraz, Liang Liu, Yue Zhang, Jian Liu. Under review in Journal of Colloid and Interface Science.

   Hongzheng Zhu developed ALD processes for AlO_xN_y, synthesized the Si anode, applied AlO_xN_y coating on Si anode, performed structural and electrochemical characterizations, and wrote the manuscript; Mohammad Hossein Aboonasr Shiraz, Liang Liu and Yue Zhang helped revise the paper. Jian Liu oversaw and guided the

project.

3. Chapter 5: "Molecular-Layer-Deposited tincone: a New Hybrid Organic-Inorganic Anode Material for Three-Dimensional Microbatteries", <u>Hongzheng Zhu</u>, Mohammad Hossein Aboonasr Shiraz, Lu Yao, Keegan Adair, Zhiqiang Wang, Huan Tong, Xueyang Song, Tsun-Kong Sham, Mohammad Arjmand, Xiping Song and Jian Liu**. Chemical Communications, 56, 13221-13224, 2020.

   Hongzheng Zhu deposited MLD coating, completed structural and electrochemical characterizations and manuscript writing; Mohammad Hossein Aboonasr Shiraz helped to revise the paper; Lu Yao helped in data analysis; Keegan Adair, Zhiqiang Wang, and Tsun-Kong Sham performed synchrotron radiation characterizations; Xueyang Song analyzed the synchrotron radiation data; Huan Tong and Xiping Song performed HRTEM characterization; Mohammad Arjmand provided N-CNT samples; Jian Liu oversaw and guided the project.

4. Appendix A: "Spark Plasma Sintering of Lithium Aluminum Germanium Phosphate Solid Electrolyte and its Electrochemical Properties", <u>Hongzheng Zhu</u>, Anil Prasad, Somi Doja, Lukas Bichler and Jian Liu. Nanomaterials, 9(8), 1086, 2019.

   Hongzheng Zhu helped in the synthesis of LAGP powder and pellets, completed the structural and electrochemical characterizations of the experiment, and wrote the manuscript; Anil Prasad and Somi Doja performed the SPS preparation of LAGP pellets; Lukas Bichler and Jian Liu oversaw and guided the project.

Table of Contents

List of Tables

List of Figures

Acknowledgment

Chapter 1: Introduction

Energy storage is now one of the top-rated concerns for further deployment globally in order to reduce the tremendous demand for fossil fuels and CO_2 emissions. Because of the growing environmental concerns caused by nonrenewable energy sources, more advanced renewable energy storage devices require a long cycle life and suitability in electric and hybrid electric vehicles. Thus, secondary batteries have been developed to compensate for this tremendous amount of demand.

A battery is a device that uses an electrochemical oxidation-reduction (redox) cycle to turn the chemical energy contained in its active components directly into electric power. Typically, there are several major components in a battery cell: (1) the cathode, or positive electrode - also referred to as the oxidizing electrode - which absorbs electrons from the external circuit and reduces themselves throughout the electrochemical process; (2) the anode or negative electrode - also known as the reducing electrode-which donates electrons to the external circuit and is reduced during the electrochemical process; and (3) the electrolyte-the ionic conductor-which transfers ions between the anode and cathode of the cell. The electrolyte is primarily a liquid, such as water or other organic solvents, containing dissolved salts, acids, or alkalis to provide ionic conductivity. Among the secondary batteries, Lithium-ion Batteries (LIBs) are regarded as among the most promising options for electric cars, uninterruptible power supplies, renewable energy sources because of their high energy density and cheap cost [1]. Li-ion batteries have a higher energy density or specific energy than the lead-acid cell; when considering the price of battery per energy capacity, the relative cost of lithium batteries has decreased significantly.

1.1 Lithium-ion batteries

Exploration of renewable and clean energy has drawn lots of interest in recent years because of the limited resources of fossil fuels. Although sustainable energy such as wind

turbines [2], photo-thermal receivers and photovoltaic cells [3] have awe-inspiring progress nowadays, batteries as an energy storage technology capable of reserving sustainable power with long-term stability and extended cycle life are still far behind.

The pursuit of energy density has always been the driving force of the continuous development of lithium batteries in the last decades. From lead-acid systems in the 1850s through nickel-metal hydride batteries in the 1960s to LIBs today, the specific energy is increased from 30 Wh kg^{-1} (lead-acid cell) up to 270 Wh kg^{-1} (LIBs). Li-ion battery technology has attracted much interest because of its great promise of increased energy density, more appropriate operating voltages, reduced self-discharge, and fewer maintenance needs. In the last two decades, LIBs have very impressive success. They provide power to most of today's portable devices. It shows great potential as a power source that can lead us to realize the demand for electric vehicles. Figure 1-1 exhibited the current and future LIB systems. As shown, in the current LIB system, carbon is used as the anode material, and lithium metal oxide (LiMO$_2$, M = Mn or Co, *etc.*) is used as the cathode material. The main cell processes are Li-ion intercalation/de-intercalation cycles between two layered materials that are reversible. The electrochemical reactions that happened in LIBs can be expressed as follows:

(Anode) $C_6 + Li^+ + e^- \rightleftharpoons LiC_6$ (Equation 1)

(Cathode) LiMO$_2 \rightleftharpoons 1/2Li^+ + 1/2e^- + Li_{0.5}MO_2$ (Equation 2)
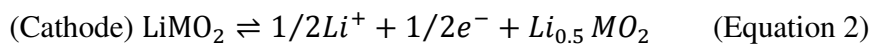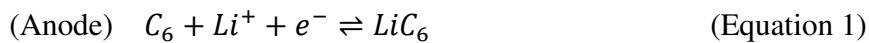
As mentioned, improved progress has been made in developing new battery systems to meet the demand for higher energy consumption devices, but the requirement never ends. For example, graphite as a traditional anode showed a capacity of 375 mAh g^{-1}. However, new anode materials (Si and Sn) based on alloying and conversion mechanisms have grown more interest due to their energy density.
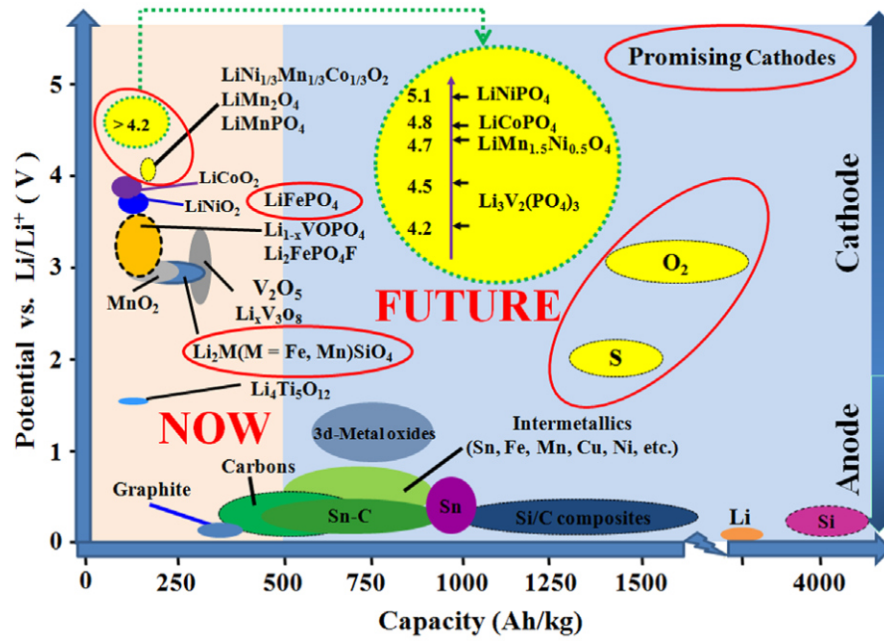
Figure 1-1. A schematic presentation of the current LIBs and the high-performance LIBs in the future [4].

The alloying mechanism means some elements like Si can give rise to Li storage and cycling behavior by alloying and dealloying. As shown in Figure 1-2, element Si will have reaction with Li metal (since Li_xSi adopt distinct crystal structures and exhibit physical properties different from Li and Si). The Li alloying-dealloying reactions, which usually occur at low potentials (preferably below 1.0 V $vs.$ Li/Li$^+$), contribute to the reversible capacity during Li cycling ($Si + 4.4\ Li \leftrightarrow Li_{4.4}Si$). As a result, Si, as an alloying mechanism anode, has a theoretical capacity of 4200 mAh g^{-1}, which is more than 10 times that of graphite. The theoretical capacity and the volume change of different stages of silicon lithiation have been reported in table 1. By applying alloying-based anode such as Si, the energy density of LIBs can be lifted to another new level, which is very meaningful to the battery market.
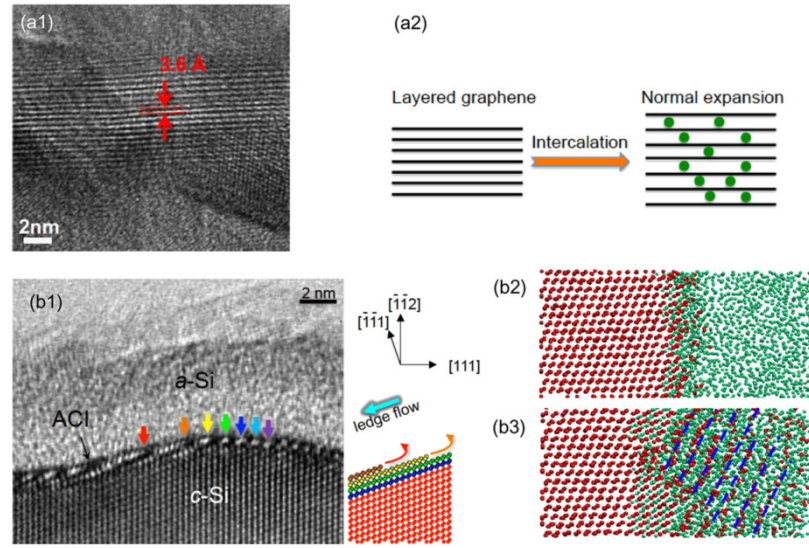
Figure 1-2. Two typical lithiation mechanisms: intercalation (*e.g.*, layered graphene) *vs.* alloying (*e.g.*, Si). (a1) A TEM image shows Li intercalation into the layered graphene, causing interlayer expansion from 3.4 Å to 3.6 Å. (a2) Schematics showing Li intercalation into layered graphene. (b1) A TEM image showing alloying of c-Si during lithiation. (b2 and b3) Two sequential snapshots from atomistic simulations during lithiation [5].

Table 1. Theoretical capacity and the volume change of Si at different stages of lithiation [6].

Stage of lithiation	Theoretical capacity (mAh g^{-1})	Volume (Å^3)
Si	0	19.6
LiSi	954	31.4
$Li_{12}Si_7$	1635	43.5
Li_2Si	1900	51.5
$Li_{13}Si_4$	3100	67.7
$Li_{15}Si_4$	3590	76.4
$Li_{22}Si_5$	4200	82.4

1.2 Silicon anode: merits and challenges

Rechargeable batteries have attracted much interest from academia and industry for applications in vehicular propulsion, portable electronic devices, and stationary energy storage. Compared to other rechargeable batteries, people have an ever-growing demand for high-quality LIBs because of their good features such as higher energy density, higher operating voltages, limited self-discharging, and lower maintenance requirements [7-10]. Graphite electrodes have been utilized as the most common commercial anode due to their appropriate electrochemical

4

characteristics, cheap purchase, and stability. However, graphite anodes exhibit only a mediocre specific capacity (372 mAh g^{-1}), which cannot satisfy the increasing demand for commercial used electrical devices [11].

Among all potential candidate anode for graphite, Si-based materials are considered one of the most promising anodes for many reasons. Firstly, Si has a superior gravimetric capacity of 4200 mAh g^{-1} when lithiated to Li$_{4.4}$Si, which is more than 10 times graphite anode. Secondly, Si anode has a moderate discharge voltage ($\sim$ 0.4 V *vs.* Li$^+$/Li) [12-14] that can remain reasonable open circuit voltage while avoiding lithium planting. Thirdly, Si is abundant on the earth (second richest in earth crust), low cost, environment friendly, and non-toxic [14].

Although Si is one of the best replacement candidates [15] for graphite electrodes, its weak features can still not be ignored. Firstly, Si has a huge volume change of 400% during the charging and discharging. Because of this hurdle, mechanical stress appears on the surface of silicon materials, resulting in cracking and pulverization. Much of the active material loses electrical contact with conductive materials and current collectors due to this reason, leading to a low electrical conductivity [16, 17]. Secondly, unstable solid electrolyte interphase (SEI) issues should also be under consideration. SEI film is a barrier layer on the surface of silicon-based material and allows the penetration of lithium-ion and the insulation to the electron. It is formed by the electrolyte decomposition during the first lithium intercalation and eventually terminated at a certain thickness [18]. A thin SEI layer can protect electrolytes from direct contact with Si and avoid further decomposition. However, due to the expansion of Si, the initial SEI layer will break, and a fresh SEI layer continuously forms on the newly exposed Si surfaces. It causes the consumption of lithium ions and prolongs lithium diffusion distance through the thicker SEI layer, and increases the internal resistance [19] (Figure 1-3).

5
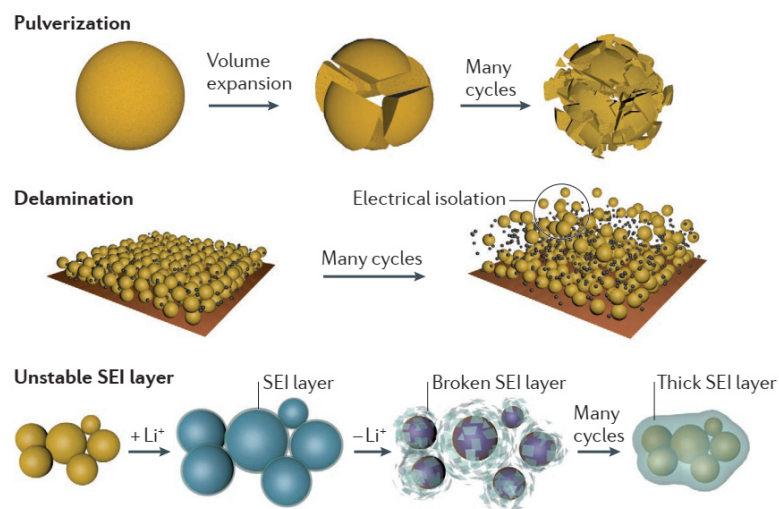
Figure 1-3. Issues of Si swelling accompanied with (a) pulverization, (b) delamination, and (c) unstable SEI layers. [20]

Thirdly, when it comes to practical use, the swelling problem of Si electrodes and its impact on volumetric energy density is another serious issue to be addressed. For the ideal packing density, initial porosity must compromise the volume change issue during lithiation/de-lithiation. When the electrode has a binder and a conductive agent, it imposes numerous additional practical constraints, such as poor manufacturability, low electrical conductivity, and mechanical integrity retention followed by fracture and pulverization. Furthermore, the electrode swelling in the conventional cell also causes other problems such as deforming the separator, blocking the pore, squeezing out the electrolyte, and bulging the battery pack. Hence, solving the electrode swelling issue is crucial to enhancing the volumetric energy density for the further practical implementation of the Si anode.

1.3 Addressing silicon anode issues

Several pathways have been applied to remove the barriers that arise from the silicon anodes and their utilization in battery applications. These strategies consist of, but are not limited to, nano-sizing and void space engineering, surface coating and fabricating composite electrode

6

materials.

1.3.1 Design of Si particles

Because of the high average binding energy and large specific surface area on the surface of nanomaterials, nanostructured or nanoscale Si materials are good at accommodating their volume shift [21]. Therefore, these materials can reduce irreversible potential and improve cycling stability by minimizing stress on Si particles during volume expansion and shrinking and avoiding their structures breaking or pulverizing [22]. Nanoparticles, nanowires (NW), thin films, and hollow structures such as nanotubes and hollow spheres are good candidates for solving Si volume expansion. According to the isoperimetric inequality in geometry, spheres have the least surface area compared to more sophisticated structures with the same volume. Stress on spheres is often considered isotropic. However, higher-dimensional materials such as Si nano thin films and NWs experienced anisotropic volume changes due to morphological features and stress generated by adhesion to the present collector [23, 24].

In Si particles, hollow Si spheres and porous Si particles can accommodate volume shift more effectively due to their larger actual surface area and greater resistance for tensile stress [25]. In Yao and co-workers' research, interconnected Si hollow nanospheres with improved cycle stability and rate efficiency were explored. [26]. Their work produced a template of hollo silica spheres and stainless-steel substrate for the first time. After the chemical vapor deposition (CVD) of SiH_4 at 485 °C for 20 min and etching with HF, the hollo sphere was prepared. The Si spheres semidiameter has been estimated at approximately 175 nm, with the outer Si spheres semidiameter at about 200 nm, and the thickness of Si at approximately 25 nm. For the first discharge, the hollow Si structure delivered a specific capacity of about 2725 mAh g^{-1} at a rate of 0.1 C. The electrode could deliver the capacity of 1420 mAh g^{-1} after 700 cycles at 0.5 C.

To the best of our knowledge, fabricating silicon electrodes with hollow and porous features has been claimed as an effective way to suppress some short-term swelling problems. However, there are still challenges such as restricted space for accumulating large volume expansion, undesired side reactions, and uncontrolled formation of SEI layer on the surface that limit the long-term cycling stability of silicon anode in LIBs and limit the adoption of this approach [27].

1.3.2 Conventional surface engineering of Si electrode

The surface coating has shown to be a realistic strategy for alleviating electrode undesired side reactions and improving electrode capacity retention, rate capability, and even thermal stability. As shown in Figure 1-4, one or more of the following conditions should be met by the surface coating: (i) thin and uniform covering; (ii) lithium-ion and/or electron conductivity; and (iii) high toughness [28]. Surface and interface engineering have shown to be more promising and valuable in silicon anode to stabilize the interface between anode and electrolyte. By coating or assembling nanostructured silicon, direct contact between the silicon and the electrolyte has been blocked, which enhanced the cycling stability of the batteries. Various functions can be applied by designing different coating layers. The coating layer could be flexible to buffer the stress that comes from volume change or be electrochemically stable to prevent the silicon electrode side-reacting with electrolyte and suppress the SEI issues [19].
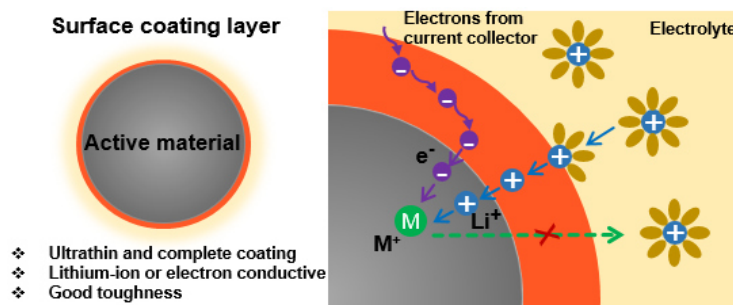
Figure 1-4. Schematic diagram of an ideal surface coating layer on the active materials [28].

1.3.2.1 Native oxide coating

Because of the inevitable presence of water and oxygen in the environment, commercially produced silicon is often covered by a native oxide (amorphous SiO_x) layer on the surface and ended with a hydroxyl group. This layer is inescapable, yet, benefit in the formation of stable SEI film during battery cycling. It is believed that the amorphous SiO_x is recognized as an appealing anode material for LIBs, which has a relatively large theoretical capacity of 1200-1400 mAh g^{-1}. Besides, the stronger bond energy of Si-O than Si-Si results in superior cycling stability for battery performance. Last but not least, the SiO_x can function as a barrier during the lithiation process, preventing electron conduction. SiO_x reacts with the insert lithium-ion and further translates into lithium silicates and Li_2O, which reduce the effects of volume expansion. Therefore, the design of the SiO_x layer enabled the improvements of electrical-chemical performance for Si-based LIBs.

Wu *et al.* assembled a novel double-walled Si-SiO_x nanotube (DWSiNT) anode, which successfully inhibits the SEI issues of silicon-based anodes [29]. The structure of DWSiNT consists of an active silicon inner wall and a silicon oxide shell that is permeable to ions. Thus the electrolyte only contacts the SiO_x shell and is unable to enter the hollow inner space. During both lithiation and de-lithiation, Lithium ions can permeate the outer wall and react with the inside Si. Because the outside wall has mechanical rigidity., only the inner Si expands and contracts in the hollow space. The DWSiNT structure has two merit features: (i) the stable outside SiO_x allows the formation of a steady SEI layer; (ii) The hollow region provides free room for inner silicon expansion without mechanical breakage. The DWSiNT electrode demonstrated a high battery performance with outstanding cycling stability. Half-cells have been cycled over 6,000 times while maintaining over 85% of their original capacity. This structure design with a passivated layer surface and a hollow inner electrode could also be applied in other

battery system suffered volume change issues.

Similar to this research, Chen *et al.* used a low-cost metal-assisted chemical etching approach to create porous Si nanowires with a thin oxide layer (~ 3 nm) on the surface [30]. By annealing, such an oxide coating is purposely created on the surface of porous Si nanowires, limiting the vast volume expansion of the underlying Si. As a result, the cycling performance of LIBs is stabilized. Specifically, the capacity of Si/SiO_x nanowires is 1503 mAh g^{-1} at the 560th cycle, with only a 0.04% drop per cycle compared with its initial capacity. At the same time, the solid-state lithium transportation path was shortened the electrolyte penetration was accelerated due to the highly porous structure. In contrast, the solid-state lithium transportation path was shortened because of the thin Si wall. As a result, stable and satisfactory reversible capacities of 1297, 976, 761, 548, and 282 mAh g^{-1} are delivered at the current densities of 1200, 2400, 3600, 4800 7200 mA g^{-1}, respectively.

1.3.2.2 Carbonaceous coating

It is well established that the use of Si-C composites can address the issues of silicon electrodes because it combines the advantages of carbon anode (long cycle life) and silicon anode materials (high lithium-storage capacity). Conventional Si-C composites, on the other hand, are often made by simple mechanical mixing or ball-milling. Despite thoroughly mixing, silicon particles may also be placed within conformal and homogeneous carbon shells, which is a potential strategy for improving battery performance. [31]. Si electrode coated with carbon layer prepared by a thermal vapor deposition method has already been studied back to 2001. Silicon powder and toluene/benzene vapors were used to create the carbon coating, which successfully protected Si particles. However, due to the small amount of silicon in this experiment, the specific capacity of the electrode is restricted. To overcome this issue, by using the spray-pyrolysis process, Ng *et al.* create spheroidal carbon-coated silicon nanocomposites [32]. This

composite electrode contains a high amount of silicon of 44 wt.% and a large capacity of 1489 mAh g^{-1} after 20 cycles. Unfortunately, the long-term cycling performance is still not satisfied in this work.

Hu *et al.* proposed a simple and straightforward method for obtaining Si@SiO$_x$@C nano-composites [33]. The carbon and SiO$_x$ thin layer are made by one-step hydrothermal carbonization of glucose with silicon nanoparticles. As a result, the Si@SiO$_x$/C nano-composites electrode presented a significant enhancement of lithium storage (large reversible capacity), excellent cycling stability (1100 mAh g^{-1} after 60 cycles at the current density of 150 mA g^{-1}), and high rate capability (600 mAh g^{-1} at a rate of 1000 mA g^{-1}), which can be considered as a promising anode material in LIBs.

Further exploration of other carbon sources such as pitch [34], acetylene [35], citric acid [36], polyvinylidene fluoride [37], glucose [38], and dopamine [39] accompanied with the chemical vapor deposition, pyrolysis carbonization, hydrothermal and sol-gel methods [40] have also been taken. They all have considerable achievements in improving the cycling performance for Si-based anode.

1.3.2.3 Metal oxide coating

Other than carbonaceous coating and the native coating layer, Si may also be protected from direct physical contact with the electrolyte by a metal oxide covering layer. To expand on this concept, Lee *et al.* created a composite with a surface coating layer composed of a 20-30 nm thick Li silicate and Li titanate. They observed a significant battery performance increase [41], and after 1000 cycles at 1 C, the composite continued to have the capacity of 1000 mAh g^{-1} (67% retention). Furthermore, rate testing found that the composite material has the ability to discharge 800 mAh g^{-1} at 10 C. Meanwhile, the capacity of uncoated Si was reduced significantly at only 3 C. Not only do Li-titanate and silicate coatings provide a protective barrier, as do many other

coatings, but they also provide a more efficient Li-ion diffusion pathway. This is because Li-titanate has a few times higher Li-ion diffusivity (8.36×10^{-11} cm^2 s^{-1}) than the SEI coating on pristine Si NPs (1.56×10^{-11} cm^2 s^{-1}). As a result, the composite becomes more conductive when the cell is charged and discharged.

Although researchers have investigated different strategies in protecting Si electrodes with fully understanding, mostly their approach is to use conventional CVD, sol-gel, or hydrothermal methods. These methods usually cannot control the exact thickness and uniform composition based on their reaction mechanism. In this regard, new coating methods are still drawing attention from scholars. In the next part, some advanced surface coating methods and how they improved the Si electrode performance will be introduced.

1.3.3 Advanced surface engineering of Si electrode

1.3.3.1 Atomic Layer Deposition (ALD) and Molecular Layer Deposition (MLD)

Aimed at addressing challenges of Si electrode, new methodologies and technical strategies to synthesize high-quality coating has always been the great interest to researchers [6]. To enhance the interfacial properties of Si anode in LIBs, atomic layer deposition (ALD) and molecular layer deposition (MLD) have been drawn more attention in the past decade. This section briefly introduces the merit and main features of ALD and MLD and reviews various inorganic/organic coatings applying on Si anodes.

ALD is a thin film technique capable of surface modifications of Si electrode designs [42]. It can form conformal and uniform coatings on top of various complex structures with atomic precision. MLD is a technique similar to ALD; it is mainly for organic and organic-inorganic hybrid materials, while ALD is exclusively for inorganics. In regard to Si electrode, ALD and MLD coatings merits can be summarized in three main aspects: (i) restrain the large volume change of Si electrode, (ii) suppress the SEI layer formation to stabilize interfacial properties,

and (iii) improving mechanical integrity of Si materials [43].
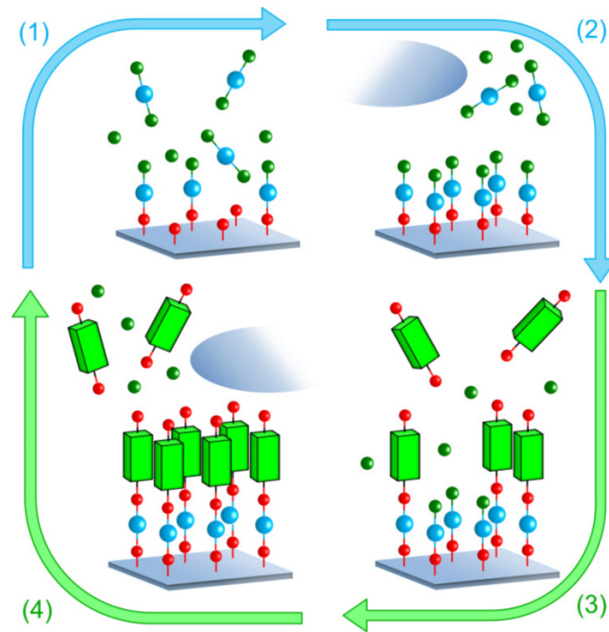
Figure 1-5: A basic schematic of the ALD/MLD cycle consisting of four steps [43].

ALD is a surface-controlled process in which the growth of films is dictated by two self-terminating gas-solid surface reactions, in contrast to its traditional counterparts such as chemical vapor deposition (CVD) and physical vapor deposition (PVD), which are dominated by the supply of precursor sources. Figure 1-5 depicts the mechanics of ALD procedures to show how they work [42].

An ALD/MLD cycle consists of the four phases listed below. [43] As is shown in Figure 1-5: (1) The reactor is pulsed with the first precursor, which interacts with the surface species, (2) the excess precursor and potential byproducts are removed from the reactor by purging with an inert gas such as nitrogen or argon or by evacuation, (3) The reactor is pulsed with the second precursor, which interacts with the surface species, and finally (4) the excess precursor/possible byproducts are removed from the reactor. Step (1) and (2) is called the first half-reaction, and

step (3) and (4) is called the second half-reaction. A monolayer of an inorganic/organic substance is created in an ideal situation. The basic ALD/MLD cycle is repeated as many times as necessary to achieve the desired film thickness to apply thicker coatings.

The first half-reaction relies on the interaction between the reactive surface sites and the first precursor. The reaction terminates with a newly created layer when the reactive surface sites are saturated. In other words, the gas-solid interaction is self-limiting by nature. The new layer provides reactive sites for the following half-reaction while a vacuum system purges the oversupplied precursor and by-products. Similarly, the second half-reaction, which is also self-terminating, produces another new layer with new functional groups for the subsequent reactions. In reality, the two half-reactions unite to create the target material at the atomic level. In the case of MLD process, because of the introduction of organic precursors, the growth per cycle will be controlled at the molecular level.

It should be noted that temperature is one of the main factors influencing the deposition features in an ALD process. On the one hand, a suitable temperature should enable ALD precursors to produce enough vapors, and their concentrations in the gaseous phase must surpass a threshold value to saturate all adsorption sites on a substrate in order to ensure continuous monolayer coverage. A good ALD temperature should also not be higher than any precursor degradation temperature. In that case, the deposition will be a CVD process rather than an ALD one [44].

Based the unique feature of ALD/MLD, these two techniques can improve Si anodes' electrochemical performance, including cycling-ability, Coulombic efficiency, sustainable capacity, and rate capabilities. Furthermore, the ALD and MLD methods may be used on both Si materials and prefabricated Si electrodes. There are also several differences between ALD and

MLD coatings. Generally, because ALD coatings are inorganic coating, they would be more chemically stable when applied in liquid electrolytes. But the electrical and ionic conductivity of ALD coating is relatively lower than MLD coatings. As a comparison, MLD is the flexible result from its organic part, which is more suitable for Si electrodes considering the huge volume changes issue.

1.3.3.2   Plasma Enhanced Atomic Layer Deposition (PEALD)

PEALD is a new energy-enhanced ALD system that is gaining traction rapidly [45]. Allowing for more flexibility in process parameters, a more comprehensive range of material properties, and high reactivity of the plasma species on the deposition surface are several merits that have been derived from PEALD compared to the ALD in recent years. Usually, a normal plasma-enhanced ALD plasma can use oxygen, nitrogen, or a mixture of them as a reactant gas. Such plasmas may be used to deposit metal oxides, metal nitrides, and metal films by replacing ligand-exchange reactions characteristic of H_2O or NH_3. Since the plasma species deliver high reactivity to the deposition surface, less thermal energy is needed at the substrate to drive the ALD surface chemistry. This implies that films with similar material properties may be deposited at lower substrate temperatures than thermal ALD. In our situation, battery content usually includes a binder, which is brittle at higher temperatures. The deposition state is more desirable with the PEALD process. Meanwhile, PEALD has several advantages over thermal ALD, such as film density [46], impurity quality [47], and electronic properties [48]. Due to the high reactivity of the plasma, certain plasma species generate a high density of reactive surface sites. As a result, faster growth per cycle value may be achieved [49].

1.3.3.3   Si anode coating with ALD and MLD

Since ALD, MLD and PEALD method has so many benefits as a coating material, it is a natural result that researchers want to find out how they perform in protecting Si electrode.

ALD coatings on Si electrode: Elmira Memarzadeh Lotfabad and her co-workers studied Si nanotubes ALD coated with TiO_2, TiN, or Al_2O_3 high-performance LIB anodes. In their work, They investigate the application of TiO_2, TiN, and Al_2O_3 on the inner, outer, or both sides of hollow Si nanotubes (SiNTs) to improve their cycling performance. The optimum performance was achieved for nanotubes conformally coated on both sides with 1.5 nm of Li active TiO_2 with substantial improvement in capacity retention to 1700 mAh g^{-1} *vs.* 1287 mAh g^{-1} uncoated baseline, after 200 cycles at 0.2 C. The coating material highly effectively enables rapid lithiation and de-lithiation. The coated composites exhibit little structural degradation and high cycle stability. (7% degradation between 100 and 200 cycles), making them a promising material for LIB anodes [50].

MLD coating on Si-based batteries: Piper *et al.* [51] carried out molecular layer deposition to grow a mechanically robust and flexible coating, produced a high-capacity Si nano-composite anode. Piper's group coated the Si electrode with a polymeric alucone, called aluminum glycerol (AlGL). As a result, the MLD coated electrodes could reach a capacity of nearly 900 mAh g^{-1} with a CE% of > 99% after 150 cycles at 0.1 C. This excellent performance comes from the AlGL coatings infiltrating the electrodes' porous structures and covalently binding to the electrode surfaces (Figure 1-6). In another work, Piper *et al.* [52] further investigated another MLD film using hydroquinone (HQ) and TMA to fabricate an Alucone coating for Si electrodes. In this study, the MLD film was further annealed at different temperatures under both inert and air atmospheres to form 3D cross-linked polymeric hybrid films. As a result, the AlHQ coated Si anodes treated at 200 °C in Ar helped achieve a capacity of 1500 mAh g^{-1} and a CE% of >99% at 0.05 C after 200 cycles, which is much higher than the AlHQ coating without annealing treatment (1000 mAh g^{-1} at 0.05 C after 200 cycles).

Furthermore, the MLD technique results in providing hybrid coatings covalently bonded on the electrode surface with highly elastic property, which improved the adhesion ability of the MLD coating.

Although PEALD has many merits than ALD, the research in using PEALD coating for Si electrodes has been minimal.
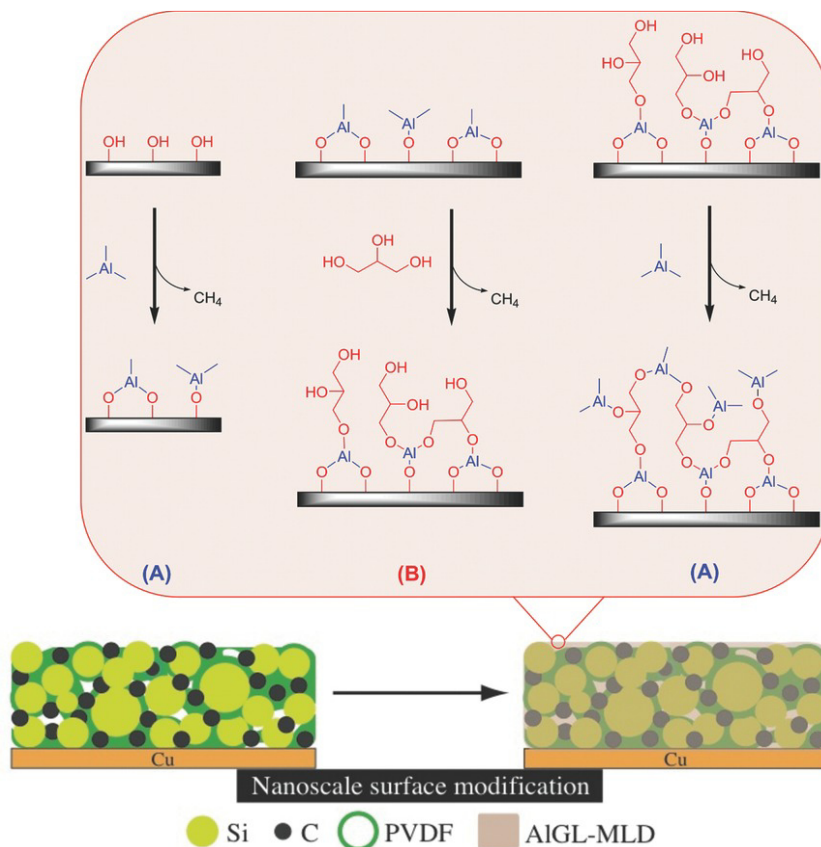
Figure 1-6: Schematic of the controlled layered chemistry structure of the AlGL used to coat the conventional Si nanocomposite electrodes. The AlGL coating is based on sequential, self-limiting reactions of trimethylaluminum ($Al(CH_3)_3$) and glycerol ($C_3H_5(OH)_3$). The growth rate of this MLD reaction is known to be 2.5 Å per AB cycle at a substrate temperature of 140 °C. PVDF represents polyvinylidene fluoride [51].

1.4 Thesis objectives

Silicon electrodes are among promising materials for LIBs because of their high theoretical capacity and energy density. However, the Si volume expansion and SEI layer issues restrict the practical usage of Si electrodes. Surface engineering is known as an effective way to tackle the

17

problem that arises in silicon electrodes. Thus, the thesis objective is mainly focused on minimizing the barriers of Si electrodes by different surface engineering pathways.

Part 1: **The usage of a facile and low-cost method to fabricate Al₂O₃ coating layer on Graphite/Si composite electrode**

In this part, a solution-based method was used to coat Al_2O_3 on the G/Si composite electrode to address the issues. The solution-based approach is a well-known method to deposit a coating agent with a favorable thickness on the target materials. Al_2O_3 is famous for serving as a protective coating film in LIBs. Al_2O_3 can turn into a Li-ion conductor after the first discharge and become an artificial SEI layer, which acts as a physical barrier to prevent the side reactions between the G/Si anode and the electrolyte, facilitates the diffusion of Li^+ through the ion-conductive layer.

Part 2: **The usage of advanced coating techniques to improve Si electrode performance**

In this part, an advanced coating technique was chosen to address the Si electrode problems. ALD is a promising method to form a uniform coating with précised thickness control. Two enhanced categories of the ALD method, MLD and PEALD, were employed to modify the Si electrode.

1) PEALD was applied to coat aluminum oxynitride (AlO_xN_y) on the Si electrode. The coating material AlO_xN_y was chosen because of its excellent physical and chemical properties, resulting in a wide range of electrical and optical responses, which make it invaluable for battery applications.

2) The second experiment is to use tincone coating on Si electrode by MLD technique. Tincone was selected as a coating agent since tin-based materials have Li-ion storage ability. Meanwhile, tincone film made by MLD method have the flexibility to address the Si expansion problem.

1.5   Thesis organization

This thesis consists of 6 chapters: 1-introduction, 2-methodology, 3-5 results and discussion, and chapter 6-conclusion, contribution and perspective, organized in an "Integrated-Article" format. Specifically, this thesis includes the following parts:
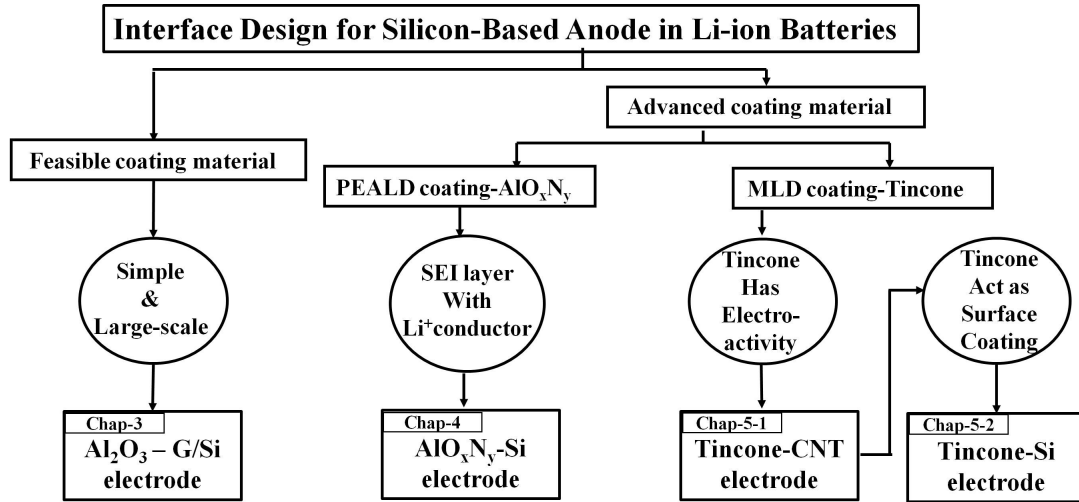
Figure 1-7. Thesis structure and connection between sections

Chapter 1-Introduction: gives an introduction to LIBs, the advantages of employing Si electrodes as anode materials in LIBS, their challenges, and the solutions to address the issues such as particle nano-sizing and surface engineering methods. Specifically, ALD was discussed as an advanced method to remove the problems arise in Si-based electrode. Moreover, the research objectives and the thesis structure are stated clearly.

Chapter 2- Methodology: outlines the procedure of PEALD and MLD method to coat AlO_xN_y and tincone on Si electrode, respectively. A detailed explanation of electrode fabrication and battery assembling has also been stated. Structural and electrochemical analysis used to investigate battery properties were described, and the information that could be derived from them to evaluate battery performance is explained.

Chapter 3-5: Results and discussion:

Chapter 3: In this chapter, the first approach was explored to tackle the Si-based electrode issues. For this purpose, a facile and low-cost sol-gel method was used to form a thin Al_2O_3 coating layer on the G/Si anode. Different post-cycling analysis methods were used to investigate the effect of Al_2O_3 coating on improving the structural integrity of Si electrode, battery life long, and Colulombic efficiency.

Chapter 4: This chapter focuses on the second approach to solve the Si-based electrode issues. PEALD method was employed to coat AlO_xN_y layer on the Si electrode. The confinement of silicon nanoparticles embedded into the electrode matrix is well achieved by the PEALD surface engineering method, showing the enhanced kinetics of the charge/discharge process for the electrode with coating.

Chapter 5: This chapter aims to fabricate tincone by MLD method on Si electrode to suppress the Si-based electrode issues. To understand how tincone protects the Si electrode, a tincone-CNT electrode was fabricated to determine the Li-ion storage ability of tincone in the absence of Si electrode. Then, the tincone was coated on the Si electrode to investigate the electrochemical properties of the elevated electrode.

Chapter 6: This chapter summarizes the results derived from all of the works done in this thesis and mainly discusses the suggestions to continue work in this field of study.

1.6 Novelty and Originality of Research

The following list summarizes the novelty and originality of research from this thesis:

1. In chapter 3, as the first time for the anode, a facile and low-cost solution-based method was applied to coat Al_2O_3 on G/Si in LIBs. Al_2O_3 coating has been used commonly with this method to protect cathode materials in LIBs.

2. In chapter 4, AlO_xN_y was developed with the PEALD method and employed AlO_xN_y as

a coating material on Si anode for LIBs for the first time. The AlO$_x$N$_y$ coating could change to an SEI layer that contains a Li-ion conductor during charge-discharge, which is a great asset and requirement of artificial coating films. This work demonstrated the promising applications of metal oxynitrides as novel surface coating materials in LIBs.

3. In chapter 5, the novelty can be divided into two aspects. First, our findings showed the tincone has Li-ion storage capability at the deposited state and without any further treatment, which is a quite new understanding in this field of study. Second, to the best of our knowledge, no one has reported the tincone coating on the Si electrode to address the issues of the silicon anode. Tincone not only acts as a flexible surface coating material to accommodate the volume change of Si but also contributes to reversible Li-ion storage due to its electrochemical activity. Thus, tincone by MLD is an electrochemically active and flexible organic-inorganic hybrid material for LIB applications.

Chapter 2: Research methodology

The research methodology in this thesis consists of the material synthesis, characterization, and electrochemical test. In this chapter, they will be introduced in general, and the sequence of the methodology is shown in the flow chart of Figure 2-1. The details of the research methodology vary in each work and will be introduced thoroughly in the corresponding chapter.
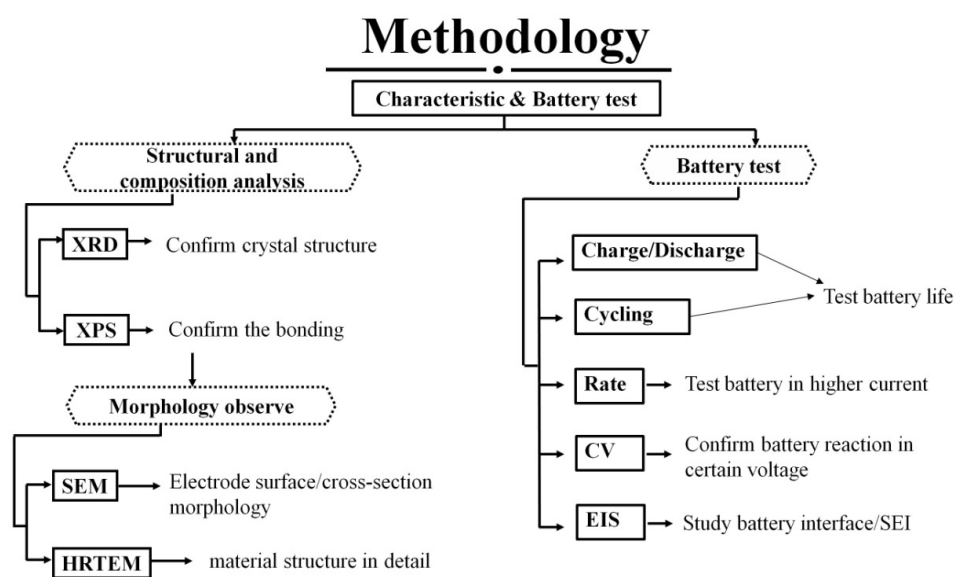
Figure 2-1. Diagram of the methodology used for the preparation and analysis of the samples.

2.1 Materials synthesis

2.1.1 Al₂O₃ coating on G/Si anode

Commercial G/Si powders with a capacity of ~ 600 mAh g^{-1} were supplied by NanoSienergy Inc. and used as received. For a typical Al$_2$O$_3$ coating process, 0.6 g of G/Si powders were dispersed into 50 ml of 0.5 wt% Al(NO$_3$)$_3$ (Sigma Aldrich) aqueous solution under stirring for 30 minutes. After that, 50 ml of 0.5 wt% urea solution was dropwise added into the above solution. The obtained solution was under vigorous stirring to mix thoroughly for an additional 30 minutes. During this process, the addition of urea into the solution increased its PH

to form $Al(OH)_3$ to enhance the adhesion of Al^{3+} on G/Si particles. Then the mixture was placed in a water bath at 70 °C until it became gel-like and concentrated. After the adsorption process, washing was repeated several times to remove all remaining soluble ions. The obtained mixture was transferred into a tube furnace, heated to 900 °C at 5 $^{\circ}$C min^{-1} under a nitrogen protection gas (20 sccm), and calcinated at 900 °C for 6 h. After naturally cooled down to room temperature, gray powders were collected, designated as Al_2O_3-G/Si, and used for further structure and electrochemical characterizations.

2.1.2   Atomic layer deposition

ALD has gained popularity in recent years, and it has tremendous promise for use in next-generation LIBs [53]. ALD is a thin-film deposition method that is saturating and irreversible, also known as self-limiting and self-terminating. Each precursor was exposed to the substrate surface during an ALD procedure. Regardless of the quantity of reactant available, only a specific amount of material was adsorbed on the substrate. The fundamental feature of ALD is the automated control of the quantity of material deposited. This innovative deposition technique offers many benefits because of its unique reaction mechanism. ALD can create a controlled thin layer with a consistent thickness on a complicated surface, such as a three-dimensional (3D) substrate   [54]. Furthermore, the ALD deposition can be performed at relatively low temperatures (< 350 °C), even room temperature (RT) [54, 55]. Unlike the highly temperature-dependent CVD process, the quantity deposited by ALD each cycle is determined by the circumstances under which the reactions occur (reactants, substrate).

As explained in the introduction, MLD and PEALD have the same deposition advantages as ALD, forming conformal and uniform coatings on various complex structures with atomic precision. Meanwhile, they have their merits, such as flexibility and high reactivity. Our

experimental section uses MLD and PEALD as a deposition method for Si electrodes to modify the Si-electrolyte interface and improve the battery performance. Here, the steps of the deposition process will be explained in detail.

2.1.2.1 MLD tincone deposition

The deposition of tincone by MLD was performed at 100°C in a commercial ALD system (GEMStarTM XT Atomic Layer Deposition System, Arradiance, USA) using (tetrakis(dimethylamino)tin (IV), (TDMASn, Strem Chemicals) and Glycerol (GL, Sigma Aldrich) as the precursors. The source temperature for both TDMASn and GL was 60 °C. The precursor pipeline was maintained at 100 °C to avoid precursor condensation. Nitrogen gas (99.999%) was used as the carrier gas at a flow rate of 20 sccm. Base pressure in the ALD reactor was sustained at 200 miliTorr. The MLD procedure was set as follows: (1) a 0.5 s supply of TDMASn; (2) a 5 s extended exposure of TDMASn to the substrates; (3) a 10 s purge of oversupplied TDMASn and any by-products; (4) a 1 s supply of GL vapor; (5) a 5 s extended exposure of GL to the substrates; (6) a 30 s purge of unreacted GL and any by-products. Using this reaction sequence, the thickness of tincone deposited on the Si electrode was controlled by varying the number of MLD cycles. The same procedure was used to coat tincone on CNT.

2.1.2.2 PEALD AlO_xN_y deposition

AlO_xN_y coating was deposited on Si electrodes in a GEMStar XT-P PEALD system (Arradiance, USA). The deposition of AlO_xN_y was performed at 100 °C using trimethylaluminum (TMA) and plasma N_2/H_2 (50/50 sccm) as the precursors. Each ALD cycle consisted of four steps: (1) 0.025-s pulse of TMA, (2) 10-s purge using Ar gas to remove TMA and any by-products, (3) 10-s pulse of N_2/H_2 gases with exposure to plasma under 300W power, and (4) 10-s purge with Ar gas. Using this reaction sequence, the thickness of AlO_xN_y deposited on the Si electrode was controlled by varying the number of PEALD cycles.
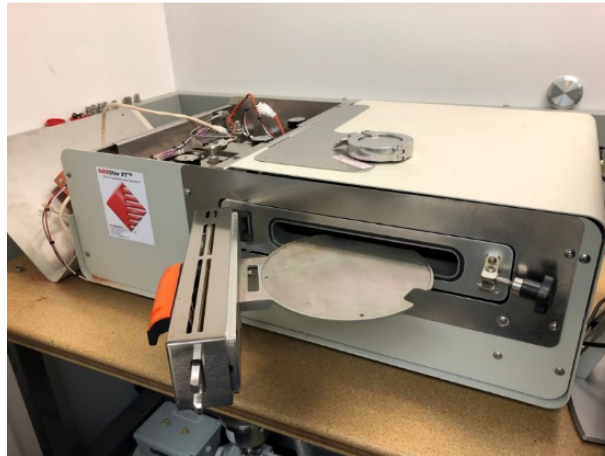
Figure 2-2. The digital picture of the ALD equipment (GEMStarTM XT Atomic Layer Deposition System).

2.2 Structural characterization

Modern batteries are made up of organic, inorganic, and metallic components that vary in size from Å to cm. It is critical to utilize the proper tools to evaluate these components.

2.2.1 Scanning electron microscope (SEM)

SEM is a type of electron microscope that produces images of a sample by scanning the surface with a focused beam of electrons [56]. The electrons interact with atoms in the samples, producing various signals containing information about the sample's surface topography and composition. Secondary electrons (SE) are the primary means of viewing images in the SEM. When electrons hit onto samples, atoms ionize and generate secondary electrons. Since the SE signal used in the SEM is derived from secondaries that escape into the vacuum, the SE image is mainly a property of the specimen's surface structure (topography) rather than any underlying structure. Another type of electron that SEM usually uses is the back-scattered electron (BSE). BSEs are beam electrons that are reflected from the sample by elastic scattering. The intensity of the BSE signal is strongly related to the atomic number (Z) of the specimen. BSE images can provide information about the distribution, but not the identity, of different elements in the

sample. Usually, in battery material investigation, an SEM is used to observe the active material and its morphology change before and after surface modification. For example, the Si particles before and after ALD coating in our case are observed by SEM. Meanwhile, when the active material was made into electrode disk, the electrode surface and cross-section morphology change, such as small cracks on the electrode surface and thickness difference, is meaningful to understand the electrode working mechanism and SEI layer variation.

Energy-dispersive X-ray spectroscopy (EDS), sometimes called energy dispersive X-ray analysis (EDX), is an analytical technique used for the sample's elemental analysis or chemical characterization. Its characterization capabilities are mainly due to the fundamental principle that each element has a unique characteristic X-rays. To stimulate the emission of characteristic X-rays from a specimen, a high-energy beam of charged particles such as electrons is focused on the sample. The target electron is ejected from the atom's inner shell, and the atom is left with a vacant energy level. Outer-shell electrons then fall into the inner shell, emitting quantized photons with an energy level equivalent to the energy difference between the higher and lower states. Each element has a unique set of energy levels, and thus the transition from higher to lower energy levels produces X-rays with frequencies that are characteristic of each element. EDX can provide a fundamental understanding of the elements that exist in the electrode with/without coating.

Figure 2-3. SEM at UBCO.

2.2.2　Transmission electron microscopy (TEM)

Transmission electron microscopy (TEM) is a microscopy technique in which a beam of electrons is transmitted through a specimen to form an image. The image is then magnified and focused onto an imaging device, such as a fluorescent screen. TEM can image at a significantly higher resolution and capture fine detail-even as small as a single column of atoms. Transmission electron microscopy is a primary analytical method in the physical, chemical, and biological sciences. Electrons are emitted in the electron gun. The gun consists of an electron source, also known as the cathode, since it is held at a high negative potential and an electron-accelerating region. The thermionic electron gun contains a V-shaped filament made of tungsten wire. A direct current heats the filament to about 2700 K, at which temperature tungsten emits electrons into the surrounding vacuum by the process known as thermionic emission. Thermionic emission can be increased by applying an electrostatic field to the cathode surface. If the electrostatic field at a tip of a cathode is increased sufficiently, the width of the potential barrier becomes small enough to allow electrons to escape through the potential surface barrier by quantum-mechanical tunnelling, a process known as field emission.

The specimen thickness should be less than about 200 nm in practice, assuming an accelerating potential of 100 kV. Any part of the field of view that contains no specimen (such as a hole or a region beyond the specimen edge) is formed from electrons that remain unscattered, so that part appears bright relative to the specimen. As a result, this central-aperture image is referred to as a bright-field image. Instead of selecting the non-diffracted beam to form an image, the objective aperture can be displaced horizontally so that it admits diffracted electrons. Strongly diffracting regions of the specimen would then appear bright relative to their surroundings, resulting in a dark-field image where any part of the field of view that contains no

specimen appears dark.

In our experiment, TEM was used for testing the coated Si particles to confirm the formation of the coating layer on the particle. For example, in the TEM image of modified Si, it is evident that an amorphous thin film coated the round crystallized Si particle. Usually, the crystallinity of Si particles can be confirmed with its crystal lattice diffraction. The surrounding film usually is having a thickness of about 5-10 nm. Another crystallographic experimental technique can be performed inside a TEM, which is called selected area (electron) diffraction, abbreviated as SAD or SAED. The atoms in the sample act as a diffraction grating to the electrons, which are diffracted. Some fraction of them will be scattered to particular angles, determined by the crystal structure of the sample; the image on the screen of the TEM will be a series of spots-the selected area diffraction pattern.

2.2.3   X-ray diffraction (XRD)

When X-rays propagate through a substance, the occurrence of the following processes should be considered in the phenomenon of diffraction: coherent scattering, which produces beams with the same wavelength as the incident (primary) beam. In other words, the energy of the photons in a coherently scattered beam remains unchanged when compared to that in the primary beam; incoherent scattering, in which the wavelength of the scattered beam increases due to partial loss of photon energy in collisions with core electrons; absorption of the X-rays, in which some photons are dissipated in random directions due to scattering, and some photons lose their energy by ejecting electron(s) from an atom (*i.e.*, ionization) and/or due to the photoelectric effect. X-ray diffraction and X-ray photoelectron spectroscopy are testing methods based on X-ray interaction with the samples.

2.2.3.1   X-ray diffraction

X-ray diffraction analysis is a method used to determine a solid sample's phase and crystal

structure by observing the scattered pattern of an X-ray beam from a lattice plane consisting of a uniform arrangement of atoms.

Bragg's law: when this X-ray beam is incident on the solid crystal, X-rays scattered from each atom interfere with each other to produce a diffraction pattern. Let d (Å) be the spacing between the planes in the atomic lattice and θ be the angle between the incident ray and the scattering planes. Then, $2d \cdot sin\theta$ corresponds to the light path difference with scattered waves, and diffraction occurs when this is equal to the wavelength (λ) multiplied by an integer n. This condition, known as Bragg's law, is expressed as follows in Figure 2-4.
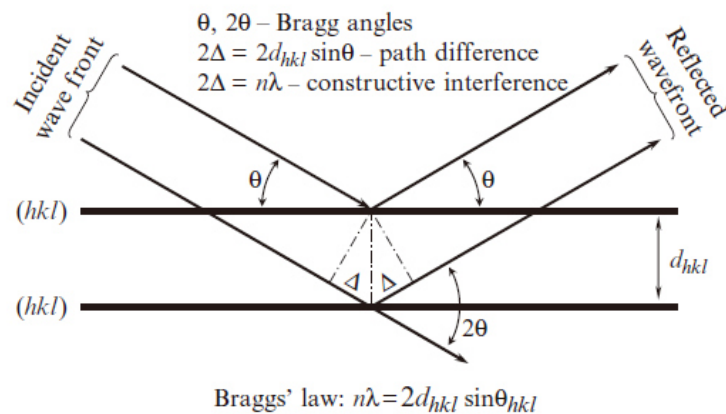
Figure 2-4: Geometrical illustration of the Braggs' law [57].

By analyzing the position of all peaks in the diffraction pattern, the distribution of lattice planes can be predicted in the crystal to learn more about the crystal structure. In general, crystalline phase identification can be obtained from XRD analysis. The crystal structure can be examined by determining the space group and unit cell. The crystalline phase of the sample can be detected using peak positions and peak intensity. A helpful reference is the powder diffraction pattern database assembled by the Joint Committee on Powder Diffraction Standards (JCPDS) and International Center for Diffraction Data (ICDD). The JCPDS card contains information on

the crystalline phase of known substances, space group, unit cell, and peaks of diffraction patterns. Quantitative determination of impurities is also possible.

In battery research, the electrochemical performance of batteries is determined by the composition of electrode materials. Besides, the intercalation and deintercalation of lithium ions cause changes in the crystal structure of electrode materials. The XRD information is essential in battery study, and they can be traced from changes in peak location or intensity in the XRD patterns.

2.2.3.2   X-ray photoelectron spectroscopy

X-ray photoelectron spectroscopy (XPS) is a surface-sensitive quantitative spectroscopic technique that measures elemental composition. It shows what elements are within a film and what other elements they are bonded to [58]. XPS is beneficial for thin surface layers less than 100 $\mathring{A}$. When an X-ray having specific energy (hv) is illuminated on the sample, the photoelectrons are emitted from a surface element. The binding energy of the emitted electron can be obtained by measuring the kinetic energy of the photoelectron. This binding energy is a unique property from which element types can be derived. Quantitative analysis is possible with binding energy measurements, and the bonding state of atoms can be determined from changes in binding energy.

Information obtained from XPS:

(a) Element analysis: the X-ray energy (E_x) illuminated on the sample has the following relationship with electron binding energy (E_B) and photoelectron kinetic energy (E_k). Since E_x and E_k are obtained from measurements, E_B can be calculated to provide information on element type, electrode composition, and impurities existing in small amounts.

$E_B = E_x - E_k$ (Equation 3)

(b) Quantitative analysis: several oxidation numbers can exist for a specific element, and

the peak resolution for that element can derive quantitative information. During this process, the binding energy of compounds containing the specific element and peak shapes. After peak splitting, the relative amount of oxidation numbers can be calculated based on the area percentage of peaks.

XPS is generally used to confirm the bonding in the material. In our experiment, this usage can be divided into two accepts. Firstly, XPS can reveal that whether the coating material is successfully synthesized on the electrode. Secondly, XPS can help us compare the composition difference of the electrode before and after battery cycling. The composition change can give us a better understanding of the mechanism of how the battery works and how the coating film improved the battery performance.

2.3 Electrochemical characterization

The electrochemical test is one of the essential parts of the battery material test. In addition, some other tests were conducted to obtain information about the mechanism of the battery properties [59].

2.3.1 Electrode preparation

Electrodes slurry usually contains active materials (the electrode material), conductive materials (carbon materials such as acetylene black, super P), and binders. It also needs the proper amount of solvent (organic or water) based on which binder is chosen to combine those materials. The slurry was milled in an agate mortar to mix uniformly and then coated onto a copper foil to a specific thickness using a doctor blade (Figure 2-5). The electrode was then placed in a vacuum oven overnight to dry the electrode and stored in an Ar-atmosphere glovebox.
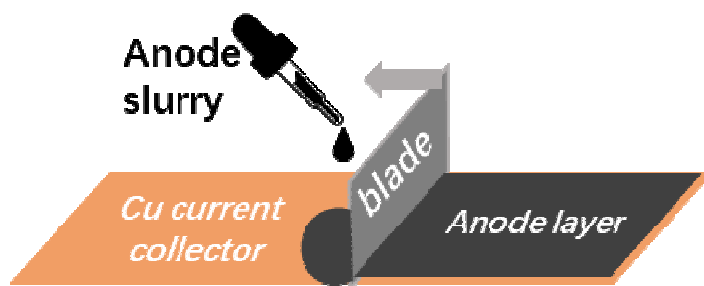
Figure 2-5: The process of anode electrode fabrication.

2.3.2 Battery assembly

CR2032 coin cells were fabricated to study the electrochemical performance of the electrode or the full battery. Firstly, the dried electrode was cut into circular discs with a diameter of 1.27 cm as the anodes. The counter electrode was lithium metal foil in a half cell. At last, electrodes, electrolyte, separator, and supporting part of battery are put in the coin cell and assembled by a crimping machine in argon (99.999%) filled glovebox (Figure 2-6) with H_2O and O_2 level below 0.1 ppm.

Figure 2-6. Glovebox workstation at UBCO.

2.3.3 Battery test

Batteries performance was tested by galvanostatic discharge/charge measurement using a computer-controlled battery tester. (Neware BTS 4000 battery testing system.) After the battery test, capacity, cycling performance, rate performance, and Coulombic efficiency can be obtained. The capacity of a battery is the product of the total amount of charge when completely discharged under given conditions and time. Battery capacity can be measured using gravimetric specific capacity (Ah kg^{-1} or mAh g^{-1}) or volumetric specific capacity (Ah l^{-1} or mAh cm^{3}).

Cycle life is the number of charge and discharge cycles that a battery can achieve before depleting its capacity. A high-performance battery should be able to maintain its capacity even after many charge and discharge cycles. The cycle life of lithium secondary batteries strongly depends on the structural stability of active electrode materials during the charging/discharging process. Irreversible capacity, which is the amount of charge lost, is usually observed after the first charge/discharge cycle and results from the formation of a new layer at the interface of electrodes and electrolytes.

Coulombic efficiency is the ratio of the output of charge by a battery to the input of charge. The internal resistance of a cell determines Coulombic efficiency. Rate capability is the number of ampere-hours a battery can deliver under specific conditions (rate of discharge, end voltage, temperature). Usually, batteries are tested at high current densities to measure their fast charge ability.

2.3.4 Electrochemical test

Electrochemical Impedance Spectroscopy (EIS) test is an electrochemical method used to examine current response under AC voltage to obtain resistance, capacitance, and inductance values. In an EIS test, information such as batteries' inner resistance can be acquired. The EIS

test of the battery was performed on an electrochemical workstation (Biologic VSP Potentiostat/ Galvanostat Station).

Figure 2-7: 80-Channel battery tester and VSP potentiostat.

A schematic of an electrode immersed in an electrolyte is shown in Figure 2-8. In this case, the charge transfer resistance (R_{ct}) represents the resistance at the interface of the electrode and electrolyte. R_e and R_{sol} represent the resistance of electron transfer in electrode and the resistance of solution (in our case, electrolyte), respectively. EIS test helps us to measure the R_{ct} and understand the reaction mechanism of the electrode. Figure 2-8b is an example of an EIS test result, which is called the Nyquist plot. Different part of the Nyquist plot is related to the reaction of the electrode. As is shown in Figure 2-8b, a high-frequency range is for charge transfer control, and a middle frequency range is for diffusion control. Figure 2-8c shows an example of the equivalent circuit of the Nyquist plot.
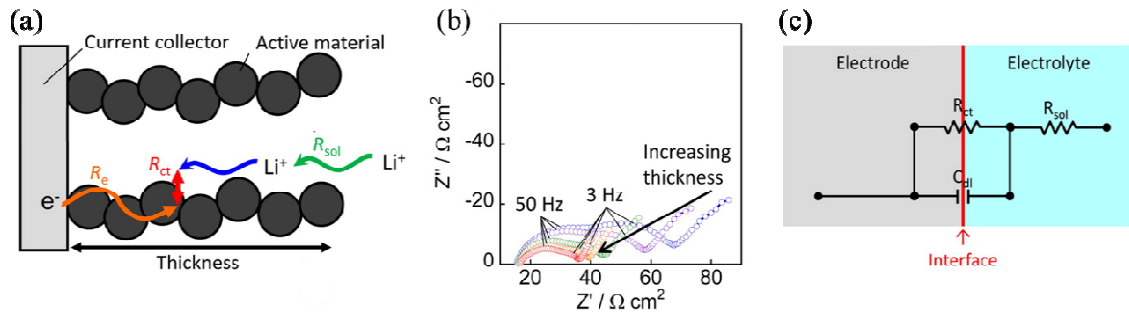
Figure 2-8. (a) Schematic illustration of the typical respective internal resistances in LIBs, (b) dependence of Nyquist plots, and (c) the equivalent circuit models, respectively [60].

Cyclic voltammetry is an electrochemical analysis method that scans voltage with a constant scan rate of voltage for a given potential range of an electrochemical cell. Cyclic voltammetry observes changes in current by applying voltage under a constant scan rate. It repeats the same experiment for each cycle. Current-voltage curves obtained from cyclic voltammetry provide information on redox reactions occurring within the cell, including (1) potential, (2) quantity of electricity, (3) reversibility, and (4) continuity (sustainability of reversible electrochemical reaction). While the scan rate differs depending on the purpose of experiments, a low scan rate is used for a detailed analysis of electrochemical reactions.

Chapter 3: Facile and Low-Cost Al$_2$O$_3$ Coating as an Artificial Solid Electrolyte Interphase Layer on Graphite/Silicon Composites for Lithium-Ion Batteries[*]

This chapter dealt with the first coating material (Al$_2$O$_3$) and method (sol-gel) to address Si-based electrode problems for practical applications. A commercial graphite/Si (G/Si) was used as the anode material for LIBs. G/Si composites are considered as a prospective alternative anode material to the commercial graphite anode due to their higher specific capacities than graphite only and relatively stable performance than pure Si. However, the unstable solid electrolyte interphase (SEI) on G/Si particles could result in rapid capacity decay, impeding its practical applications. Herein, a facile and low-cost Al$_2$O$_3$ coating was developed to fabricate stable artificial SEI layers on the G/Si composites. The amorphous Al$_2$O$_3$ coating with 10-15 nm in thickness was synthesized by a facile sol-gel method following by high-temperature annealing. Furthermore, the Al$_2$O$_3$ coating was found to be more effective in improving the stability of G/Si at high working temperatures (55 °C). The improvement was due to that the Al$_2$O$_3$ coating suppressed the continuous growth of SEI on G/Si and reduced the charge transfer resistances at the G/Si-electrolyte interface. It is expected that the Al$_2$O$_3$ coating prepared by the sol-gel process can be applied to other Si-based anodes to fulfill the practical high-performance LIBs.

The increasing demand for long-range electric vehicles has stimulated continuously to improve the energy density of LIBs [22, 61]. Over the past years, the energy density of LIBs has been marvelously increased as a result of advances in manufacturing processes and materials

science. However, the conventional LIB system, consisting of lithium transition metal oxide cathode and graphite anode, is approaching to their theoretical limits of capacities [62, 63]. For example, as the dominant anode material, graphite has advantages of good electronic conductivity and structure stability, but only offers a theoretical capacity of 372 mAh g^{-1} [22, 61-63]. Enriching electrode materials with high capacity is of significant influence but highly challenging towards achieving higher performance LIBs [64, 65].

Among the several high capacity potential anode materials, silicon (Si) has been widely investigated due to its high theoretical gravimetric capacity (4200 mAh g^{-1} vs. 372 mAh g^{-1} of graphite) [16], low working voltage (~ 0.28 V vs. 0.18 V of graphite) [66], and large abundance (second-most abundant element on earth) [67]. However, Si has its intrinsic hurdle, which is the vast volume change of up to 400% during Li alloying-dealloying process [15, 68, 69]. This poses significant challenges towards practical usage in LIBs. Firstly, the repeated volume change results in mechanical fracture and pulverization, leading to the loss of electrical contact of active Si anode from current collectors [70]. Secondly, the solid electrolyte interphase (SEI), as a protecting layer formed on the surface of Si anode, is break down and exposes the fresh Si surface, where new SEI layers continuously grow upon cycling by consuming the limited Li resources [14, 71]. Thirdly, on the cell level, the swelling of the Si electrode caused by the volume change with 50% or more exhibits lower volumetric energy density than the graphite electrode [69]. In order to tackle the volume expansion in Si, as well as similar massive volume changes electrode (such as Sn), the co-utilization has been deemed as the most appropriate approach [72]. In this regard, graphite has multiple advantages in compatibility with Si anode for commercialization [73-76]. The addition of graphite can compensate for the defect of Si anode by imparting their great electrochemical properties, such as improving the electrical conductivity

of Si anode with its higher electrical conductivity, mitigating the severe electrode swelling with its lower volume expansion (~ 10%), and improving the whole performance even with its lower price [77-79]. Finally, the most attractive advantage for commercialization in is that the co-utilization approach is readily adaptable to the established battery technology and manufacturing process for commercial graphite anode.

Nevertheless, graphite/Si (G/Si) electrodes have been reported to degrade in half- and full-cell testing, even with FEC-containing electrolytes [80-82]. Besides compositing with a carbon matrix, the surface coating is essential to stabilize the SEI layers on Si-based anode and address the electrode swelling problem. Among various surface coating materials, Al_2O_3 has been reported to be effective as an artificial SEI layer on the anode and cathode materials in LIBs, due to its proper bandgap and Li-ion conducting ability upon lithiation [51, 83-89]. For example, Xiao et al. showed that Al_2O_3 films on Si via an ALD method yielded the creation of Li-ion conductive $LiAlO_2$ on the surface, suppressing the chemical reaction between the Si and the electrolyte [85]. He et al. also deposited an Al_2O_3 film as a protecting layer on patterned Si anode by ALD using trimethylaluminum and H_2O as the precursors and the Al_2O_3-coated silicon electrodes exhibited remarkably improved cycling performance compared to the uncoated electrode [86]. In addition to ALD, the aluminothermic reduction method has also been developed to fabricate thin Al_2O_3 on the Si anode [88]. During the aluminothermic reduction process, SiO_2 was reduced and Al metal was simultaneously thermal oxidized to aluminum oxide [89]. The nano silicon coated with 2-4 nm Al_2O_3 showed a more stable cycling performance and a higher CE than the uncoated one [80]. Nevertheless, the aforementioned Al_2O_3 coating methods have some limitations for practical applications. The ALD method is still relatively costly for mass production, while the aluminothermic reduction involved complex processes. A

scalable and low-cost approach for Al_2O_3 coating is desired for G/Si anode applications.

In this work, a facile and low-cost sol-gel method followed by annealing to form a thin Al_2O_3 coating layer was developed on the G/Si anode. At 25 ^{o}C, the Al_2O_3 coated G/Si electrode showed better cycling performance than the uncoated samples. The capacity retention could retain the initial capacity up to 76.4% after 100 cycles, while the uncoated G/Si could only reach 56.4%. The post-cycling analysis by electrochemical impedance spectroscopy and SEM revealed that the Al_2O_3 coating improved Coulombic efficiency and cycling stability of the G/Si anode. The improvement is because Al_2O_3 coating reduced the solid-electrolyte-interphase (SEI) and charge transfer resistances at the G/Si-electrolyte interface and suppressed the continuous growth of the SEI layer. More importantly, this work found that the influence of Al_2O_3 coating was more profound at higher temperatures (55 ^{o}C), suggesting the importance of surface coating for Si-based anode in a broad working temperature range. It is expected that the Al_2O_3 coating developed by the sol-gel method could be used as a scalable and effective artificial SEI for Si-based anode in enabling high-performance LIBs.

3.1 Experimental Section

3.1.1 Al_2O_3 coating on G/Si anode

Commercial G/Si powders with a capacity of ~600 mAh g^{-1} were supplied by NanoSienergy Inc. (Ontario, Canada) and used as received. For a typical Al_2O_3 coating process, 0.6 g of G/Si powders were dispersed into 50 ml of 0.5 wt% $Al(NO_3)_3$ (Sigma Aldrich) aqueous solution under stirring for 30 minutes. After that, 50 ml of 0.5 wt% urea solution was dropwise added into the above solution. The obtained solution was under vigorous stirring to mix thoroughly for an additional 30 minutes. During this process, the addition of urea into the solution increased its PH to form $Al(OH)_3$ to enhance the adhesion of Al^{3+} on G/Si particles. Then the mixture was placed in a water bath at 70 °C until it became gel-like and concentrated.

After the adsorption process, washing was repeated several times in order to remove all remaining soluble ions. The obtained mixture was transferred into a tube furnace, heated to 900 °C at 5 °C min^{-1} under a nitrogen protection gas (20 sccm), and calcinated at 900 °C for 6 h. After naturally cooled down to room temperature, gray powders were collected, designated as Al_2O_3-G/Si, and used for further structure and electrochemical characterizations. The Al_2O_3 coating process was schematically shown in Figure 3-1.
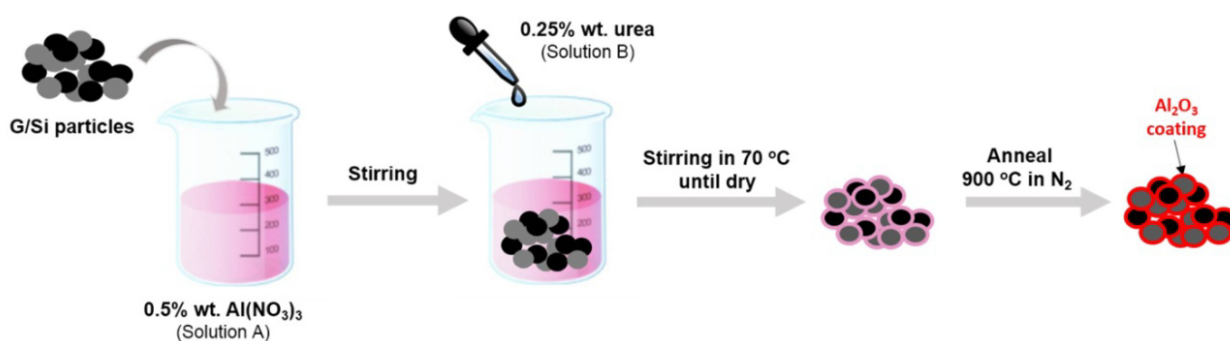
Figure 3-1: Schematic illustration of the sol-gel method for Al_2O_3 coating on G/Si particles.

3.1.2 Structural characterizations

The morphology and structure of G/Si and Al_2O_3-G/Si were characterized by using a SEM (Tescan MIRA3 FEG-ESEM) and high-resolution transmission electron microscopy (HRTEM, JEOL 2010F) equipped with energy dispersive X-ray (EDX) analysis. The HRTEM test is done by Carmen Andrei at McMaster University. The phase was analyzed using X-ray diffraction (XRD, Bruker D8-Advance X-ray diffractometer) with Cu Kα_1 & Kα_2 radiation sources. The XRD test is done with the help of Anita Lam at UBC Vancouver Chemistry.

3.1.3 Electrochemical measurements

To prepare the anode electrode, 95 wt% of G/Si or Al_2O_3-G/Si powders, 2.5 wt% of carbon black, and 2.5 wt% of carboxymethyl cellulose/styrene-butadiene rubber (CMC/SBR) were

mixed thoroughly in an aqueous solution to form a uniform slurry. The slurry was then pasted on a copper foil using a doctor blade with a thickness of 80 µm, and dried under vacuum at 80 $^{\circ}$C for 12h. The obtained electrode was cut into a round shape with a diameter of 1.27 cm. The loading of G/Si and Al_2O_3-G/Si active materials was about 2.7 mg cm^{-2}. To assemble the coin cells (CR2032), the G/Si or Al_2O_3-G/Si was used the cathode, Li metal as the anode, and polyethylene (Celgard) as the separator. The electrolyte was 1.3 M $LiPF_6$ in ethylene carbonate: diethyl carbonate (EC:DEC, 3:7, *v/v*) with 10 vol.% of fluoroethylene carbonate as the additive. The coin cells were assembled in an argon-filled glovebox workstation with oxygen and water levels below 1 ppm. The cycling performance of the coin cells was evaluated on a Neware BTS 4000 battery tester, and electrochemical impedance spectroscopy (EIS) was measured on a potentiostat/galvanostat station (SP-150, Biologic). The G/Si or Al_2O_3-G/Si electrode was cycled in a voltage range of 0.01-1.5 V (1C = 600 mA g^{-1}).

3.2 Results and discussion

Figure 3-2 shows the morphology and structure of as-received G/Si and Al_2O_3-G/Si prepared by the sol-gel method. The G/Si and Al_2O_3-G/Si composite possess irregular shapes and have sizes ranging from 1 to 15 μm (Figure 3-2a, b). After Al_2O_3 coating, Al_2O_3-G/Si particles have no apparent morphological change compared to the original G/Si. Moreover, both the G/Si and Al_2O_3-G/Si exhibit a strong diffraction peak at 26.6°, corresponding to the (002) peak of graphite (JCPDS No: 75-2078), and diffractions peaks at 28.4°, 47.3°, and 56.1°, assignable to the (111), (220) and (311) planes of silicon (JCPDS No: 75-0589), respectively. EDX elemental mapping (Figure 3-2d) discloses the uniform distribution of Al and O elements on the surface of G/Si particles, confirming the successful coating of Al_2O_3. Nevertheless, the Al_2O_3 coating layer is not detected in the XRD patterns (Figure 3-2c) due to the limited amount and low crystallinity.
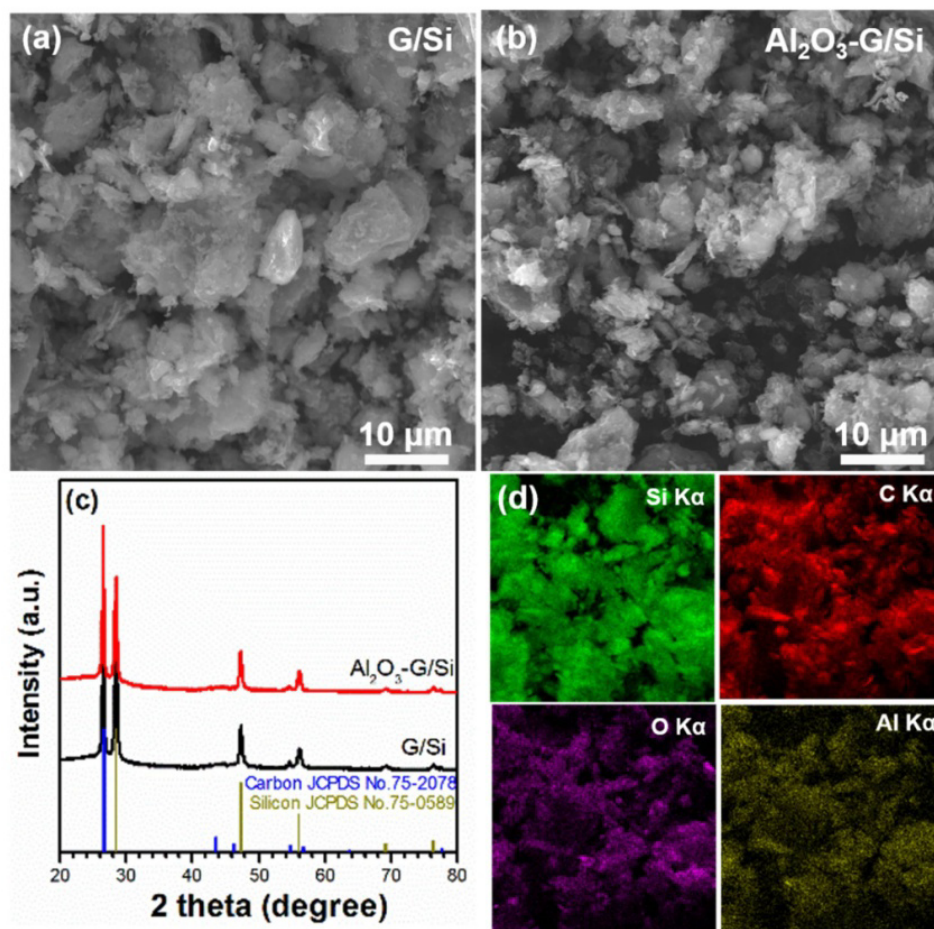
Figure 3-2: SEM images of (a) pristine G/Si and (b) Al$_2$O$_3$-G/Si; (c) XRD patterns of G/Si and Al$_2$O$_3$-G/Si; and (d) EDX elemental mapping of Al$_2$O$_3$-G/Si.
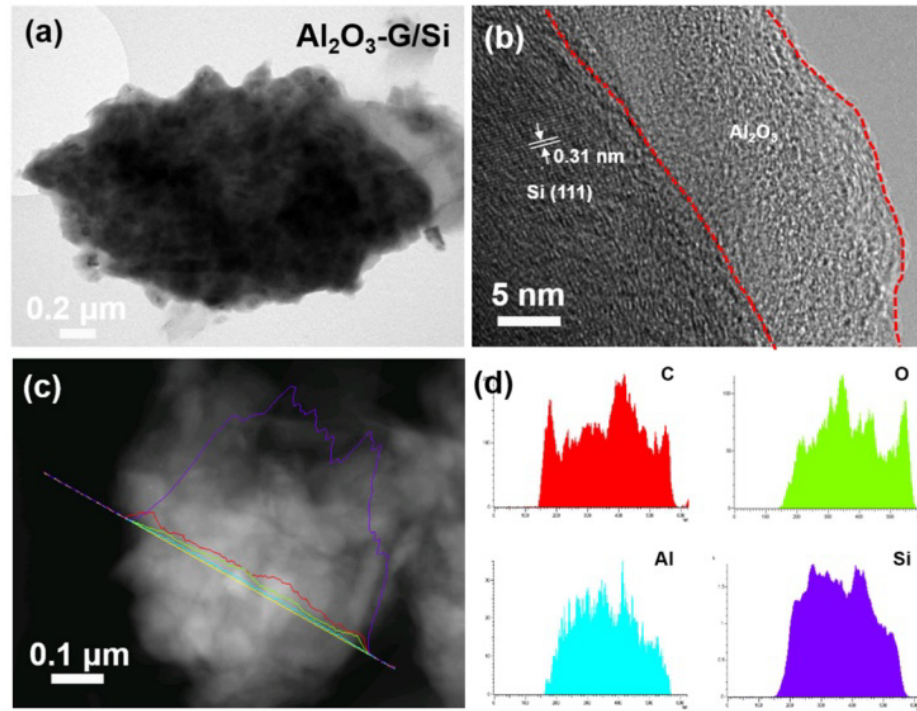
Figure 3-3: (a) TEM, (b) HRTEM, (c) STEM images, and (d) line scanning elemental mapping of Al_2O_3-G/Si.

The microstructure of Al_2O_3-G/Si was further analyzed by transmission electron microscopy (TEM), and the images are shown in Figure 3-3. Figure 3-3a indicated the microsized Al_2O_3-G/Si particles, which helps improve the tap density of the electrode. Tapped density is the density measured after the powder has consolidated. Due to the limited internal space of the battery, high tap density leads to high volumetric capacity when the gravimetric capacity is the same [90]. HRTEM images disclose the Si (111) plane with an interplanar distance of 0.31 nm and an Al_2O_3 coating layer on the G/Si surface. The thickness of Al_2O_3 layers is measured to be 10-15 nm from multiple HRTEM images. Despite short-range fringes in some locations, the Al_2O_3 coating layer exhibits a mostly disordered structure, a typical amorphous feature of Al_2O_3. Further EDX line-scanning under STEM mode (Figure 3-3c, 3-3d) verifies the distribution of Al and O elements across the G/Si particle. The above results suggest

the successful coating of the Al_2O_3 layer on G/Si particles by the sol-gel method. This conclusion is further suggested by the weak Si XPS spectrum (Figure 3-4), which is fitted into Si^{3+} peak at 103.3 eV (SiO_x) probably due to the oxidation of surface Si during the sol-gel and calcination process.

The influence of Al_2O_3 coating on the electrochemical performance of G/Si anode is studied in half cells using Li metal as the counter electrode, and the results are shown in Figure 3-5. As shown in Figure 3-5a, the initial capacity of Al_2O_3-G/Si is 659 mAh g^{-1}, similar to that of the uncoated G/Si. However, in the following few cycles, Al_2O_3-G/Si exhibits lower specific capacities than G/Si. For example, the discharge capacity in the 2nd, 3rd, 4th, and 5th cycle is 629, 635, 601, and 600 mAh g^{-1}, respectively for G/Si, and 585, 586, 538, and 541 mAh g^{-1}, respectively for Al_2O_3-G/Si. The discharge (lithiation) specific capacity loss from the 1st discharge capacity - the 2nd discharge capacity could be ascribed to the formation of SEI film with the decomposition reaction of electrolytes on the surface of the G/Si anode. The lower capacity of Al_2O_3-G/Si in the following few cycles is probably due to the activation process of the insulating Al_2O_3 coating layer. Similar activation phenomena have been observed in previous studies [85, 86]. Upon lithiation, the artificial Al_2O_3 coating layer turned into an ion-conductive Li-Al-O layer, which not only served as a physical barrier to prevent the side reactions between the G/Si anode and the electrolyte but also facilitates the diffusion of Li^+ through the ion-conductive layer [85, 86]. Overall, the Al_2O_3 coating improves the cycling stability and capacity retention of G/Si. For G/Si, the specific capacity gradually dropped from 576 mAh g^{-1} in the 10th cycle to 390 mAh g^{-1} after 100 cycles. In contrast, Al_2O_3-G/Si could still deliver a specific capacity of 530 mAh g^{-1} after 100 cycles. The capacity retention is calculated as 76.4% for Al_2O_3-G/Si and only 56.4% for G/Si. Moreover, the Coulombic efficiency (CE) of the Al_2O_3-

G/Si is higher than that of G/Si (Figure 3-5b). The initial CE is 88.2% and 87.8% for Al_2O_3-G/Si and G/Si, respectively. After stabilization in 10 cycles, Al_2O_3-G/Si exhibits an average CE of 99.3%, in comparison to 98.7% for G/Si. Both the cycling and CE results suggest that the Al_2O_3 coating reduces the side reaction between the G/Si electrode and the electrolyte.
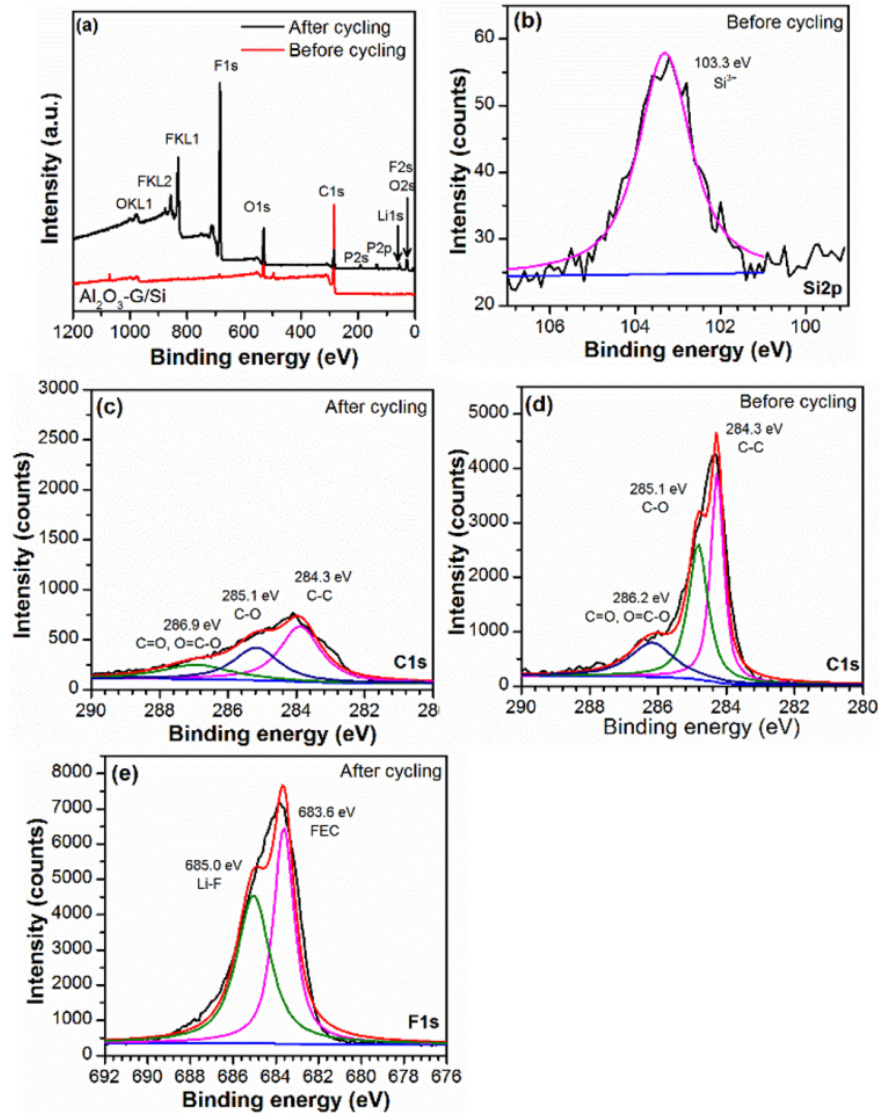
Figure 3-4: (a) XPS full spectra of Al_2O_3-G/Si before and after cycling; high-resolution spectra of (b) Si2p before cycling, (c) C1s after cycling; (d) C1s before cycling, and (e) F1s after cycling. Note: Si2p peak is not detected in Al_2O_3-G/Si before the electrode is covered with SEI. F1s is absent in Al_2O_3-G/Si before cycling because CMC/SBR is used as the binder.

Figure 3-5c and 3-5d present the charge/discharge curves of G/Si and Al_2O_3-G/Si in

different cycles at 0.1 C. As can be seen, both G/Si and Al_2O_3-G/Si exhibit similar charge and discharge curves, suggesting Al_2O_3 do not change the reaction mechanisms of Li with graphite and Si. In the 2nd discharge curve, the Li insertion into the G/Si composite occurs between 0.4 V and 0.01 V, while in the 2nd charge process, the two plateaus at 0.28 V and 0.45 V correspond to Si de-alloying [91, 92]. Moreover, it is found from 50th cycle profiles that the voltage step at ~ 0.3 V, corresponding to Li alloying with the silicon, remains in Al_2O_3-G/Si, while shifts towards a lower capacity for non-coated G/Si, suggesting that the Al_2O_3 coating decrease the capacity loss over cycling. Furthermore, Al_2O_3-G/Si displays better charge/discharge overlapping and reaction reversibility than G/Si anode, implying enhanced reaction stability of Al_2O_3-G/Si composite. The improved capacity and kinetics in Al_2O_3-G/Si could result from the protective effect of Al_2O_3 coating, which alleviates the exposure of Si to the electrolyte and reduces the formation of thick SEI film on the electrode. The coating with the proper thickness could act as a preformed SEI to reduce the regeneration of SEI and consumption of Li ions during cycling. When there is no Al_2O_3 coating, the massive volume change of Si can cause the breakage of SEI film and expose fresh Si surface to the electrolyte during repeated cycling. From the above discussion, the Al_2O_3 coating can be expected to improve the cycling stability of the G/Si anode.
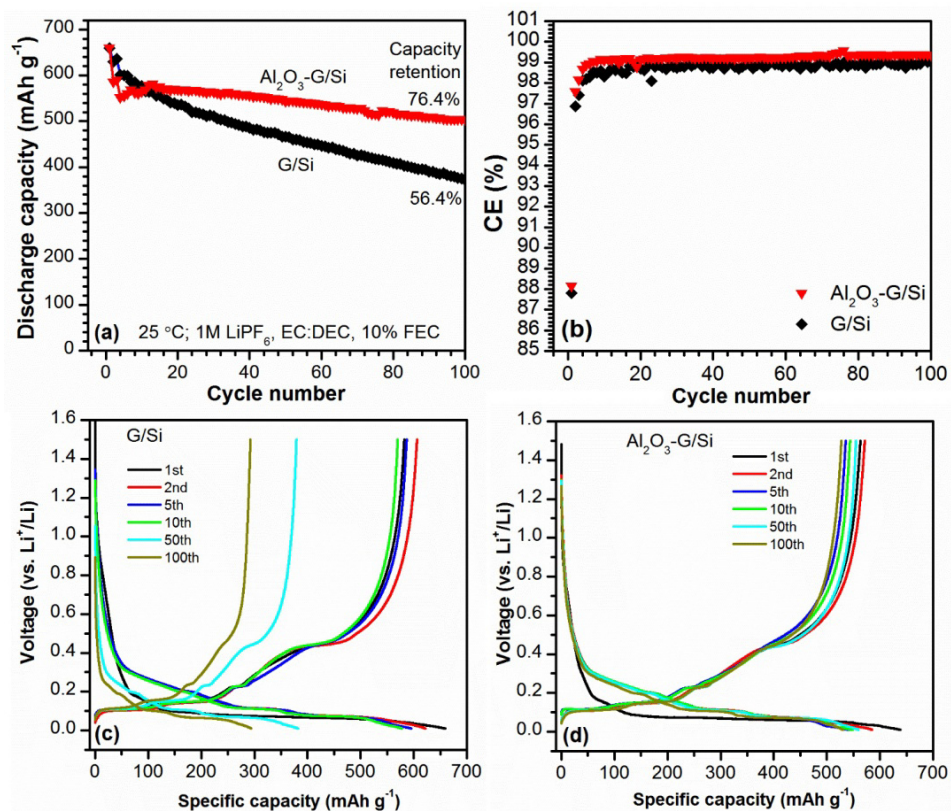
Figure 3-5: (a) Cycling stability and (b) CE of G/Si and Al_2O_3-G/Si; Charge-discharge profiles of (c) G/Si and (d) Al_2O_3-G/Si measured in a voltage range of 0.01-1.5 V at 25 °C. The current density is 0.05C in the initial three formation cycles, and 0.1C afterward (1C = 600 mA g^{-1}).

To understand the effect of Al_2O_3 on the internal resistance of G/Si, electrochemical impedance spectroscopy (EIS) analysis was performed on G/Si and Al_2O_3-G/Si after cycling, and the Nyquist plot is presented in Figure 3-6. G/Si and Al_2O_3-G/Si display two semicircles in the high- and medium-frequency regions, which correspond to the resistance at the SEI layer (R_{SEI}) and the charge transfer resistance (R_{CT}) at the electrode-electrolyte interface, respectively. The interception of the Nyquist plot with the *x*-axis represents ohmic resistance (R_o) contributed from the electrolyte and electrode-current collector interface. The inclined line in the low-frequency region is interpreted as the finite length Warburg impedance. These resistance values are extracted by fitting the Nyquist plot using the equivalent circuit inserted in Figure 3-6 (CPE

represents the constant phase element). The R_{SEI} is determined to be 7.5 Ω and 29.1 Ω for Al$_2$O$_3$-G/Si and G/Si, respectively, while the R_{CT} is calculated as 22.2 Ω and 26.3 Ω for Al$_2$O$_3$-G/Si and G/Si, respectively. EIS analysis indicates that Al$_2$O$_3$ surface coating reduces the SEI and charge transfer resistance at the electrode-electrolyte interfaces.
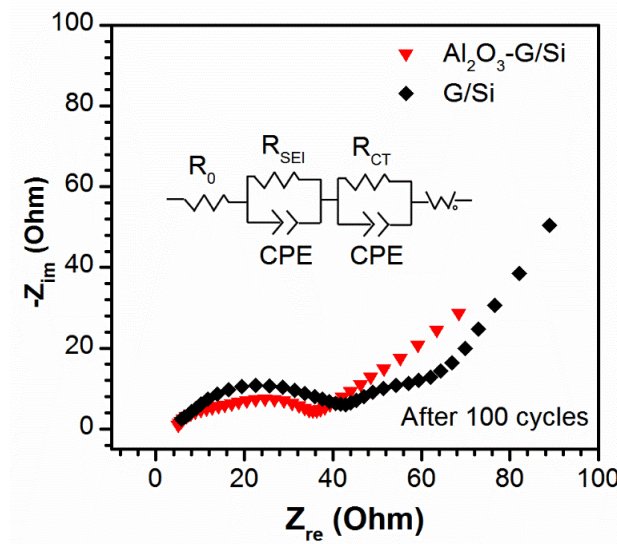
Figure 3-6: Nyquist plot of G/Si and Al$_2$O$_3$-G/Si after 100 cycles.

The morphologies of G/Si and Al$_2$O$_3$-G/Si after 100 cycles are checked by SEM, and the typical images are depicted in Figure 3-7. From Figure 3-7a, it can be found that for the G/Si composite, the thick SEI layer has formed on the G/Si particles. Additionally, the particle shape of Al$_2$O$_3$-G/Si (Figure 3-7b) still remains after cycling. The thickness of the G/Si layer is measured as 32 μm, which is much higher than that of Al$_2$O$_3$-G/Si (26 μm) (Figure 3-7c and 3-7d), proving the contribution of Al$_2$O$_3$ coating to suppressing the side reaction of electrolyte and G/Si composite and consequently maintaining the composite structure of and delivering higher gravimetric capacity. In order to make the data more credible, the electrode thickness was measured at different sites, calculated the average value, and shown in Figure 3-7 (e-j). Figures 3-7 e, f and g show the cross-section of G/Si electrode after the cycling, with the average

48

thickness of the electrode around 32.7μm. Figures 3-7 h, i and j show the cross-section of Al_2O_3-G/Si electrode after cycling and the average thickness of around 26.4μm. Also, XPS analysis on C1s peaks (Figure 3-4c and 3-4d) indicates the C-C bond (284.3 eV) from graphite is still present in the Al_2O_3-G/Si electrode after cycling, due to the relatively thin SEI layer. Furthermore, the Al_2O_3-G/Si electrode after cycling is found to contain the Li-F component, as indicated by F1s at 695.0 eV in Figure 3-4e. The Li-F results from the decomposition of FEC and helps form stable SEI layers with the artificial Al_2O_3 coating. Figure 3-8 shows the EDX elemental mapping of (a) G/Si electrode and (b) Al_2O_3 G/Si electrode after 100 cycles. There was no Al element on the Al_2O_3 G/Si electrode because of the thin layer of Al_2O_3 on the surface.
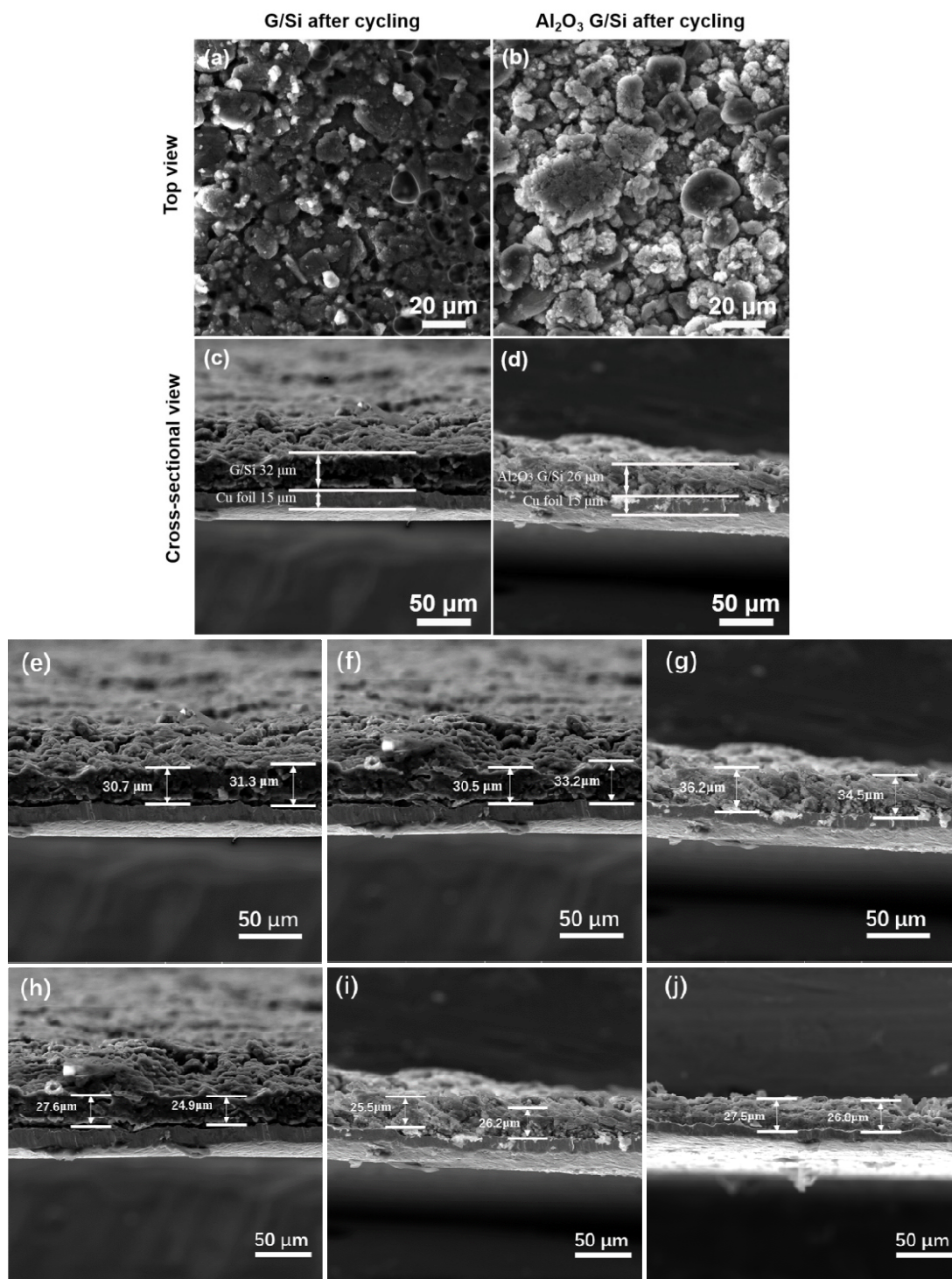
Figure 3-7: Morphologies of (a, c) G/Si and (b, d) Al$_2$O$_3$-G/Si after cycling at 25 °C. (e-j) electrode thickness at different sites.
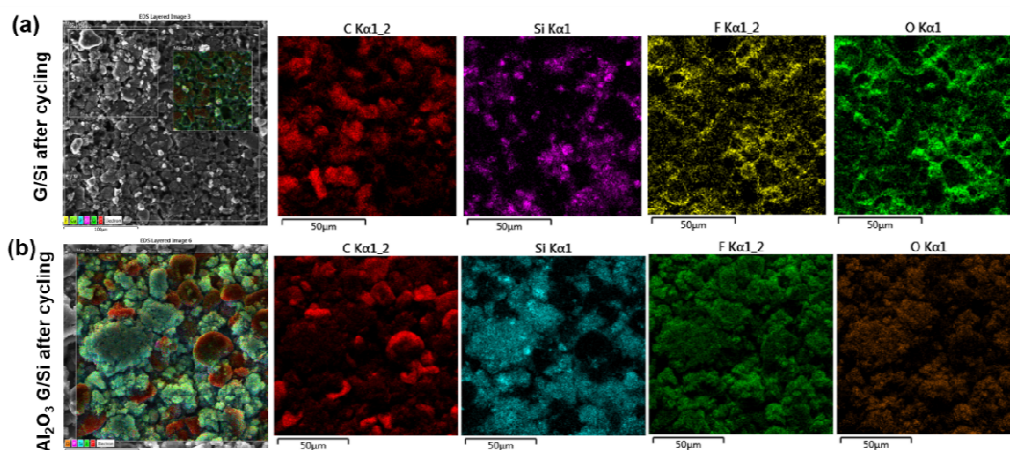
Figure 3-8: SEM and EDX elemental mapping of (a) G/Si electrode and (b) Al$_2$O$_3$ G/Si electrode after 100 cycles.

It is well known that when the temperature of a battery system increases, there will be severe side reactions in the battery. The cycling stability of the G/Si with and without Al$_2$O$_3$ was further examined at 55 °C. The reason for choosing 55°C as the highest testing temperature is that the temperature range of -20 °C~60 °C is the suggested working temperature for LIBs. Once the temperature is out of this region, LIBs will degrade with an increased risk of safety problems such as fire and explosion [93]. It can be seen in Figure 3-9a that both the Al$_2$O$_3$-G/Si and G/Si showed a higher initial capacity than they do at room temperature due to the increased diffusivity of lithium ions at higher temperatures [94]. The G/Si shows a rapid capacity decay in 80 cycles, which is caused by the harsh side reaction between G/Si and the electrolyte at elevated temperatures. As a result, the un-coated G/Si has a capacity retention of 27.6%. In sharp contrast, Al$_2$O$_3$-G/Si exhibits much-improved cycle stability and capacity retention of 66.8% over 80 cycles. Furthermore, Al$_2$O$_3$-G/Si possesses a relatively stable CE of 98-99% over cycling, while G/Si experiences a high fluctuation in the CE. The charge-discharge profiles of G/Si and Al$_2$O$_3$-G/Si at 55 °C are compared. As can be seen from Figures 3-9c and 3-9d, the charge and discharge plateaus for G/Si are gradually polarized from the 1st cycle to the 80th cycle, probably due to the

51

continuous formation of SEI layers and increased resistances. The charge and discharge curves for Al_2O_3-G/Si have good overlapping and show less polarization over cycling, suggesting the stable SEI layers enabled by Al_2O_3 coating. These results confirm the importance of Al_2O_3 coating to the performances of G/Si anode at higher temperatures.
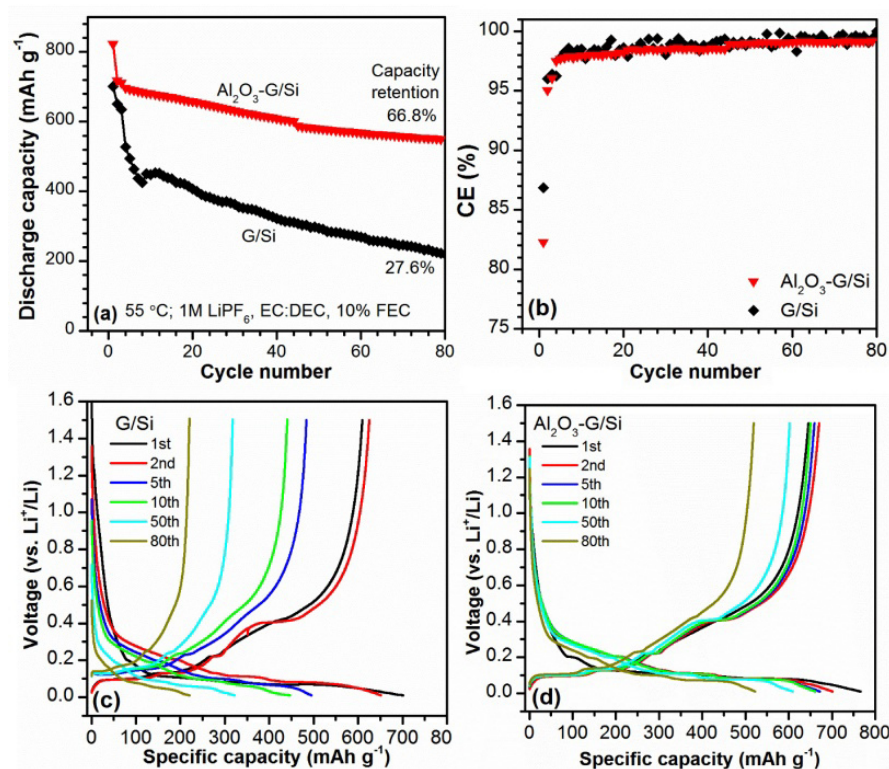
Figure 3-9: (a) Cycling stability and (b) CE of G/Si and Al_2O_3-G/Si; Charge-discharge profiles of (c) G/Si and (d) Al_2O_3-G/Si measured in a voltage range of 0.01-1.5V at 55 °C. The current density is 0.05 C in the initial three formation cycles, and 0.1 C afterward.

In summary, an Al_2O_3 coating as artificial SEI layers was conducted on a G/Si anode by a facile and low-cost sol-gel process. The results showed that the Al_2O_3 coating effectively improved the cycling stability and Coulombic efficiency of the G/Si anode in Li-ion batteries. The capacity retention of Al_2O_3-coated G/Si anode after 100 cycles could retain 76.4% at 25 °C, while the uncoated one reaches only 56.4%. At 55 °C, the Al_2O_3-coated G/Si anode also exhibited much higher capacity retention (66.8%) than the pristine anode does (27.6%). The

Al$_2$O$_3$ coating effectively prevents the growth of SEI layers and lithium-ion consumption during cycling. The sol-gel synthetic process for Al$_2$O$_3$ coating is low-cost, easy to scale up, and thus promising for practical industrial applications.

Chapter 4: Atomic Layer Deposited AlO$_x$N$_y$ Coating for High-Performance Si Anode in Lithium-Ion Batteries[†]

In the previous chapter, Al$_2$O$_3$ coating on Si electrodes was applied with a cost-efficient and straightforward method, and the coating could reduce the swelling and thick SEI issues of Si in LIBs. Meanwhile, some advanced surface engineering methods were explored for Si protection. As explained in chapter 1, ALD is one of the most state-of-the-art methods for engineering surface and interface in LIBs. In this chapter, the PEALD technique was used to fabricate a novel surface coating material, aluminum oxynitride (AlO$_x$N$_y$), on Si electrode. The effects of AlO$_x$N$_y$ surface coatings on the electrochemical properties of Si electrodes were investigated. With the optimal AlO$_x$N$_y$ coating (~ 2 nm), the reversible capacity after 140 cycles was improved from 331 mAh g^{-1} for bare Si electrode to 1297 mAh g^{-1} for AlO$_x$N$_y$-coated one, and the capacity retention (140th-cycle capacity/2nd-cycle capacity) was elevated from 13% to 72%. Post-cycling analysis revealed that the AlO$_x$N$_y$ coating significantly suppressed the charge transfer and SEI resistances and maintained the structural integration of Si electrodes by suppressing continuous electrolyte decomposition and electrode delamination from the current collector. X-ray photoelectron spectroscopy study indicated that the AlO$_x$N$_y$ coating led to the formation of Li-Al-O and Li-N ion conductors in the SEI and contributed to enhanced charge/discharge kinetics of the Si electrode. This study provides a new perspective on designing advanced functional coating materials for ALD for LIBs.

Nowadays, the demand for lithium-ion batteries (LIBs) is increasing in many different

fields, such as electronic devices, electric vehicles, and grid storage, due to their relatively high energy density and long lifetime among energy storage technologies available today. However, the ever-increasing need from end-users calls for LIBs with higher energy densities. In current commercial LIBs, graphite is used as the anode and possesses a theoretical capacity of 372 mAh g^{-1}, corresponding to 1-mol Li-ion per 6-mol C atoms. The low specific capacity of graphite results in limited energy densities of current LIBs and becomes one of the main limiting factors towards higher-performance LIBs [10, 22, 95]. Besides, present LIBs have serious safety concerns due to potential lithium plating on the graphite surface, and graphite anode needs to be replaced with a better anode with a higher specific capacity and working voltage [30]. Among all anode alternatives, Silicon (Si) has drawn the most attention because of its superior gravimetric capacity of 3590 mAh g^{-1} ($Li_{15}Si_4$) and high abundance on earth. It provides a tremendous increment to graphite [12-14].

However, Si experiences considerable volume change (~ 300%) during the charge and discharge process and thus suffers from severe cycling stability, unstable solid electrolyte interphase (SEI), and low efficiency. For example, Si active material will pulverize due to the stress-induced by alloying and dealloying, causing rapid material degradation. The pulverization of Si materials also causes detachment and isolation of the Si electrode from the current collector. The successive formation-breaking-reformation procedure of SEI also leads to low Coulombic efficiency (CE), permanent consumption of electrolytes, and severe capacity drop for extended cycling [14, 23, 32, 96-99]. All of the issues stem from the volume expansion of different phases of Li_xSi_y alloys and side reactions between these Li_xSi_y alloys with electrolytes during the lithiation/de-lithiation process. Several methods have been employed to tackle these issues, such as surface coating, nanosizing, and Si/graphite compositing. Utilizing surface

coating on nanostructured Si to construct a physical compartment to buffer the volume expansion has been shown as a practical approach [100, 101].

Among various surface coating methods, ALD has been an effective approach to create a protective layer on Si electrodes. ALD provides consecutive, separated, and self-terminating reactions between different chemical precursors and thus excellent control over the uniformity and thickness of thin films at an atomic level. ALD enables highly uniform and conformal films on the complex surface due to its surface-controlled nature. The coating material usually serves as an artificial SEI to prevent unexpected side reactions at the Si electrode/electrolyte interface and enhance battery performance. Many different types of coating have been applied on Si electrodes using ALD, such as metal oxides (Al_2O_3 and TiO_2) and metal nitride (TiN) [102]. In addition to these materials, metal oxynitride is another group of new materials with various properties, making it promising as surface coatings in batteries. For example, aluminum oxynitride (AlO_xN_y) has many excellent physical and chemical properties, which result in a wide range of electrical and optical responses [103]. AlO_xN_y has excellent mechanical and dielectric properties, as well as structure stability in high temperatures [104]. These properties make AlO_xN_y potentially invaluable for many different areas, such as temperature sensors, transparent armor, military aircraft lenses and missile domes, and semi-conductor processing applications [105-107]. However, there is little research work on the development of surface chemistry and deposition process by ALD and applications in batteries.

Herein, PEALD was adopted to deposit AlO_xN_y coating on the Si electrode for the first time. PEALD has been known as an enabler for a wide range of rapidly gaining applications in popularity. Several merits have been derived from PEALD compared to the thermal ALD. PEALD allows more flexibility in processing conditions and material properties and provides a

high reactivity of the plasma species on the deposition surface. An AlO_xN_y coating was developed by PEALD and applied on the Si electrode in our work. By employing it as a surface modification, the confinement of silicon nanoparticles embedded into the electrode matrix is well achieved, while the kinetics of the charge/discharge process is enhanced due to the unique mechanical and electrical properties of AlO_xN_y films. The capacity retention of the Si electrode was elevated from 13.3% to 72.3% with the AlO_xN_y coating. The AlO_xN_y-coated Si electrode remains a reversible capacity of 1297 mAh g^{-1} after 140 cycles.

4.1 Experimental section

4.1.1 Materials preparation

Si electrode was prepared by mixing Si nanoparticles (50-nm diameter, Alfa Aesar), Super P, and carboxymethyl cellulose/styrene-butadiene rubber (CMC/SBR) with a weight ratio of 7:2:1 in an aqueous solution to form a uniform slurry. Then the slurry was cast on a copper (Cu) foil and dried overnight in a vacuum oven at 80 °C. AlO_xN_y coating was deposited on Si wafer and Si electrodes in a GEMStar XT-P PEALD system (Arradiance, USA). The details of the PEALD process were described in chapter 2 in complete. AlO_xN_y on the Si substrate was used for growth per cycle (GPC) and X-ray photoelectron spectroscopy (XPS) measurements. The thickness AlO_xN_y thin film shows a linear dependence on ALD cycles, yielding a growth per cycle (GPC) of 0.73 $\mathring{A}$ on Si wafer (Figure 4-1). Si electrode coated with AlO_xN_y by 10, 30, and 50 ALD cycles were denoted as Si-AlO_xN_y-10, Si-AlO_xN_y-30, and Si-AlO_xN_y-50, respectively. Si wafer was also adopted as the substrate during the deposition for reference.
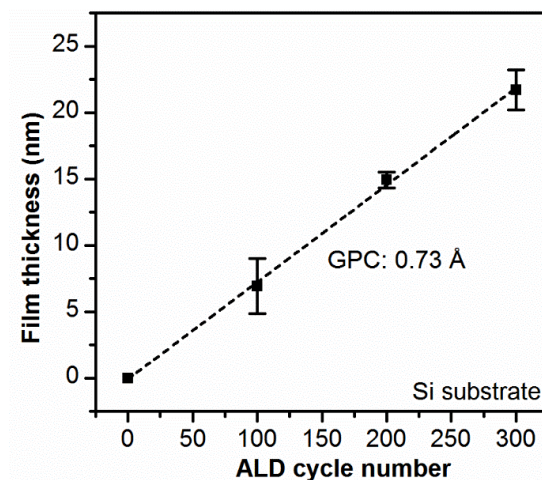
Figure 4-1: AlO$_x$N$_y$ film thickness as a function of ALD cycle number at a deposition temperature of 150 °C. A linear fitting yields a growth per cycle (GPC) of 0.73 Å.

4.1.2 Structural characterizations

Morphology and structure of Si electrode and AlO$_x$N$_y$-coated Si electrodes were characterized by using a SEM (Tescan MIRA3 FEG-ESEM) and high-resolution transmission electron microscopy (HRTEM, JEOL 2010F). The HRTEM test is done by Carmen Andrei at McMaster University. X-ray photoelectron spectroscopy (XPS) was measured on an Axis Ultra DLD (Kratos Analytical). The XPS test is done with the help of Michael Wang in 4D labs at Simon Fraser University.

4.1.3 Electrochemical characterizations

After AlO$_x$N$_y$ coating, the electrode was cut into a round shape with a diameter of 12 mm and loaded into CR2032 cell configuration cells for electrochemical testing. The bare Si electrode and Si electrodes with AlO$_x$N$_y$ coatings have used the cathode, Li metal as the anode, and polyethylene (Celgard) as the separator. The electrolyte was 1.3 M LiPF$_6$ in ethylene carbonate: diethyl carbonate (EC: DEC, 3:7, *v/v*) with 10 *vol.%* of fluoroethylene carbonate (FEC) as the additive.

The coin cells were assembled in an Ar-filled glove box with H$_2$O and O$_2$ concentrations

58

below 0.1 ppm. The cycling performance of the coin cells was evaluated in a voltage range of 0.01-1.5 V and with five formation cycles at 0.05 C and subsequent cycles at 0.1 C, on a Neware BTS 4000 battery tester. Cyclic voltammetry (CV) and electrochemical impedance spectroscopy (EIS) were measured on a potentiostat/galvanostat/EIS workstation (SP-150, Biologic).

4.2   Results and Discussion
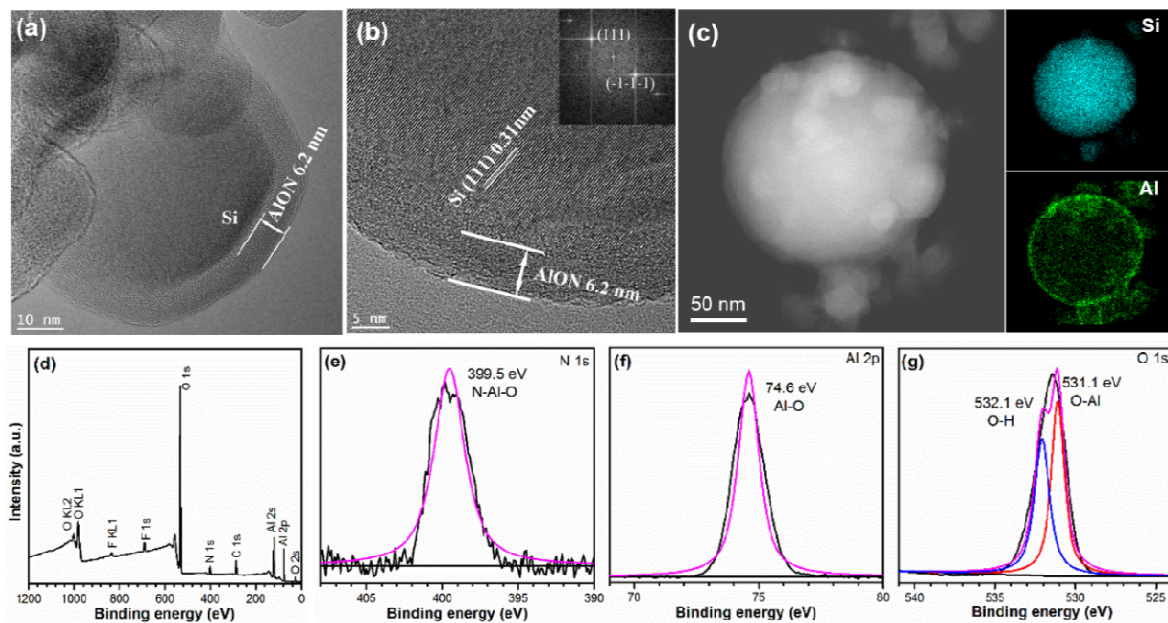
Figure 4-2: (a) TEM image, (b) HRTEM image, and (c) STEM image with EDX mapping of Si and Al elements for Si particles with AlO_xN_y coating deposited by 100 ALD cycles, (d) XPS full survey and deconvolution of (e) N 1s, (f) Al 2p, and (g) O 1s spectra of AlO_xN_y thin film on a Si substrate. (Inset in (b) is the Fast Fourier transform (FTT) image of the Si particle).

Figure 4-2 shows the structure and composition of Si nanoparticles coated with the AlO_xN_y layer with 100 PEALD cycles. The TEM image in Figure 4-2a reveals a uniform and conformal coating of AlO_xN_y film on the Si nanoparticles. The AlO_xN_y layer thickness is measured to be about 6.2 nm, slightly thinner than the value (7.3 nm) calculated based on a growth per cycle (GPC) of 0.73 Å on Si wafer substrate (Figure 4-1). HRTEM observation discloses that the interplanar distance of the Si nanoparticle is 0.31 nm, corresponding to the (111) plane of Si (JCPDS No. 27-1402), as confirmed by the fast-Fourier-transform image in Figure 4-2b inset.

59

The AlO$_x$N$_y$ layer on the Si nanoparticle surface possesses an amorphous structure and has no long-range order due to the low PEALD deposition temperature (150 °C). Figure 4-2c presents a STEM image of Si nanoparticles with 100-cycle AlO$_x$N$_y$-coating and corresponding EDX mapping of Si and Al elements. STEM and EDX analysis demonstrated the even distribution of AlO$_x$N$_y$ coating on the surface of Si nanoparticles, suggesting the benefit of PEALD in achieving high-quality ultrathin layers on electrode materials. X-ray photoelectron spectroscopy (XPS) analysis confirms the existence of Al, O, and N elements from the AlO$_x$N$_y$ coating on Si nanoparticles (Figure 4-2d). Deconvolution of N1s peak leads to one peak located at 399.5 eV (Figure 4-2e), ascribed to the N-Al-O bonding in aluminum oxynitride [108]. Al 2p spectrum is decomposed into one prominent peak at 74.6 eV, which corresponds to the Al-O bond and is verified by the 531.1 eV peak in the O 1s spectrum (Figure 4-2e). The deconvolution of the O 1s spectrum resolves another peak centered at 532.1 eV, which could be assigned to the O-H bond. The residual O-H bond could result from incomplete removal of ligands from TMA on the outer surface during the PEALD process. The incorporation of the O element into AlO$_x$N$_y$ might occur when the thin films are removed from the reaction chamber and exposed to the air. Previous work has suggested that metal nitrides can be quickly oxidized once direct exposure to air [109, 110]. The oxidation of AlN could happen because of exposure to air when the samples were taken out of the ALD reaction chamber. The same phenomena were observed in PELAD TiN, which was shown as TiN$_x$O$_y$ due to air exposure [111].
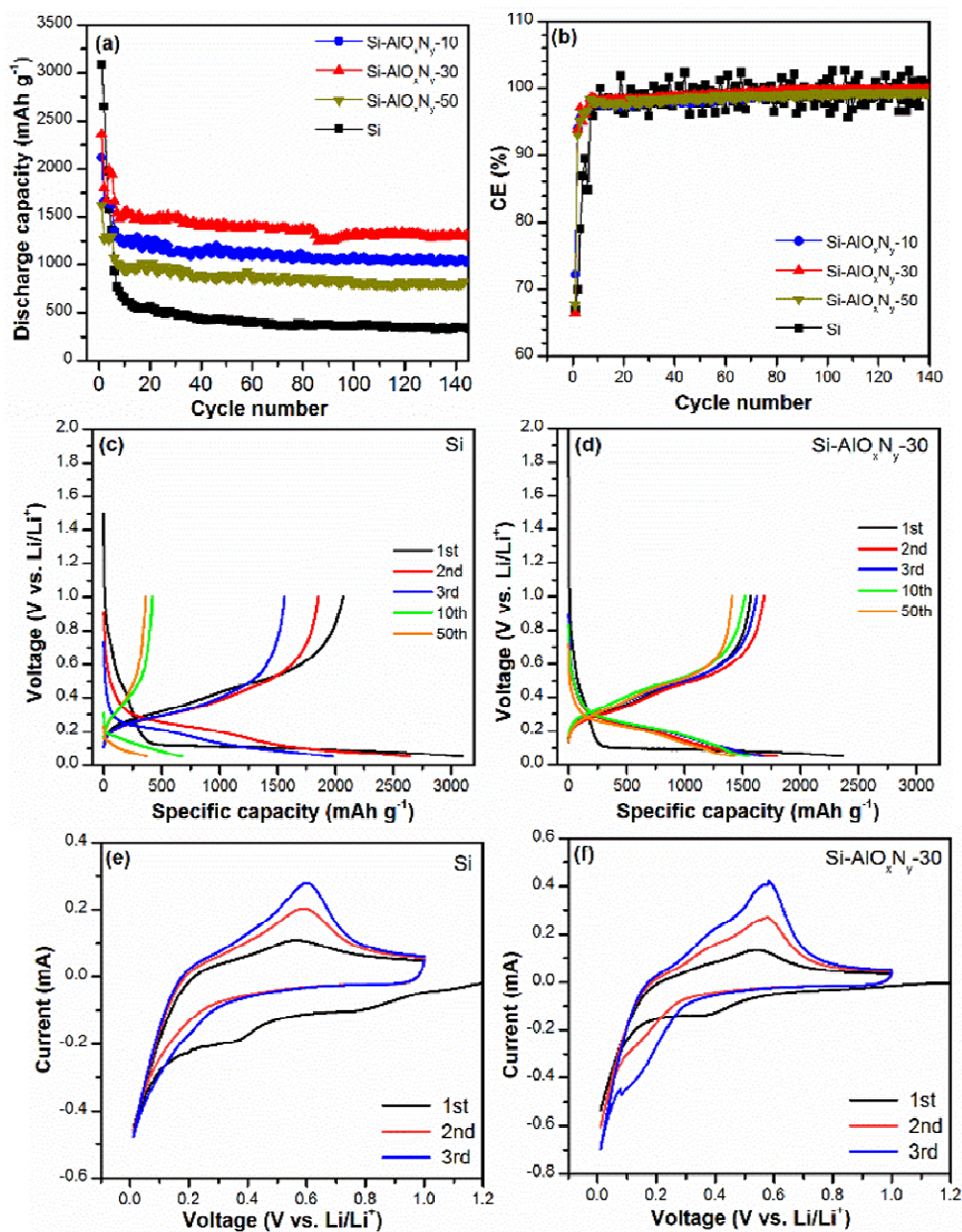
Figure 4-3: (a) Cycling stability and (b) Coulombic efficiency (CE) of bare Si electrode and Si electrode coated with AlO_xN_y layers by 10, 30, and 50 ALD cycles, measured between 0.01 and 1.5 V at 0.05 C during the initial five cycles and 0.1 C in the subsequent cycles; (c, d) charge-discharge profiles and (e, f) Cyclic voltammetry (CV) curves measured at 0.2 mV s^{-1} for Si and Si-AlO_xN_y-30 electrodes.

Figure 4-3 depicts the effect of AlO_xN_y coatings (10, 30, and 50 ALD cycles) on the electrochemical performance of Si electrodes as an anode in LIBs. All cells are tested between 0.01 and 1.5 V at 0.05 C in the initial five cycles (formation) and 0.1 C in the subsequent cycles.

61

As seen in Figure 4-3a, the initial discharge capacity is 3094 mAh g^{-1} for bare Si, and 2108, 2357, and 1624 mAh g^{-1} for the Si electrodes with 10-cycle, 30-cycle, and 50-cycle AlO$_x$N$_y$ coating, respectively. The higher discharge capacity of bare Si than the others in the initial cycles can be attributed to the higher availability of Si particles to react with Li-ion than those of coated ones. In the AlO$_x$N$_y$-coated electrode, Li-ions need to interact with AlO$_x$N$_y$ first to pass through the coating layer and then undergo alloying reactions with Si particles. From the 6th cycle, the Si electrodes with and without AlO$_x$N$_y$ coatings exhibit a dramatic difference in the specific capacity and cycling stability. The discharge capacity of Si-AlO$_x$N$_y$-10, Si-AlO$_x$N$_y$-30, and Si-AlO$_x$N$_y$-50 stabilizes at 1355, 1664, and 1070 mAh g^{-1}, respectively, while the specific capacity of bare Si rapidly drops to 937 mAh g^{-1} in the 6th cycle. The bare Si undergoes much more degradation during the initial ten cycles than those with AlO$_x$N$_y$ coatings, probably due to continuous breakdown and formation of SEI layers on the Si surface [112]. Among all the samples, Si-AlO$_x$N$_y$-30 maintains the highest specific capacity of 1297 mAh g^{-1} after 140 cycles, in contrast to 331 mAh g^{-1} of bare Si, demonstrating enhanced electrochemical properties of Si electrode using thin AlO$_x$N$_y$ coating (~ 2 nm thick) by PEALD. The capacity retention of Si electrodes (140th-cycle capacity/2nd-cycle capacity) is elevated from 13% to 72% by using AlO$_x$N$_y$ coating. From Figure 4-3a, it can be found that the electrochemical performance of Si electrodes has a strong dependence on the thickness of AlO$_x$N$_y$ coatings. The optimal one is Si electrode with 30-ALD cycle AlO$_x$N$_y$ coating (~ 2 nm). Si electrode with 50-ALD cycle AlO$_x$N$_y$ layer still shows stable cycling stability but experiences a noticeable decrease in its specific capacity compared to Si-AlO$_x$N$_y$-30. The reason could be that AlO$_x$N$_y$ coating is too thick and reduce the diffusion rate of Li ions through the artificial SEI layer, leading to suppressed redox reactions in the Si anode.

CE in the 2nd cycle is calculated as 69.9% and 93.9% for the pristine Si and Si-AlO$_x$N$_y$-30, respectively, implying that AlO$_x$N$_y$ coating reduces the side reaction between the Si electrode and the electrolyte. In general, AlO$_x$N$_y$-coated Si electrodes show improved and stabilized CE over repeated cycling, while pristine Si electrode exhibits high fluctuation in the CE (Figure 4-3b). A direct comparison between the charge-discharge curves for pristine Si and Si-AlO$_x$N$_y$-30 is presented in Figures 4-3c and 4-3d. Pristine Si experiences gradual degradation in the specific capacity and increased polarization, as evidenced by the enlarged charge-discharge plateaus. In contrast, the charge-discharge profiles for Si-AlO$_x$N$_y$-30 have good overlap in the 1st, 2nd, 3rd, 10th, and 50th cycles, suggesting the importance of surface coating in preventing side reactions on the Si surface.

To investigate the improved electrochemical properties of Si electrode by AlO$_x$N$_y$ coating, the CV test was applied on the electrodes at the scan rate of 0.2 mV s^{-1}, and the result is shown in Figures 4-3e and 4-3f. In the first cycle, it is clear that the reduction curve of bare Si has a shoulder peak at 0.8 V, corresponding to the formation of the SEI layer on the non-coated electrode in the initial cycle. This SEI formation is the direct consequence of the electrolyte decomposition and active Si loss, leading to the lower capacity of the pristine Si electrode. In contrast, the AlO$_x$N$_y$-coated electrode shows a significantly suppressed shoulder, indicating the effective role of thin AlO$_x$N$_y$ film to suppress the direct contact of active Si metal with electrolyte while providing a facile Li-ion pathway to react with Si particles in lithiation/de-lithiation. Meanwhile, the separation between oxidation and reduction peaks of Si is reduced with a 30-cycle AlO$_x$N$_y$ coating, indicating better kinetics in the Si-AlO$_x$N$_y$-30 electrode. A better overlapping of oxidation-reduction peaks, especially at the charge/discharge switch point, is observed in Si-AlO$_x$N$_y$-30, suggesting a better kinetic and suppressing thick SEI layer

formation-repeated silicon exfoliation with AlO$_x$N$_y$ coating. This good overlapping is consistent with the charge-discharge curves in Figure 4-3d. Thus, this rigid coating layer is crucial for alloying/dealloying electrodes, which are accompanied by dramatic volume change upon lithiation/de-lithiation.
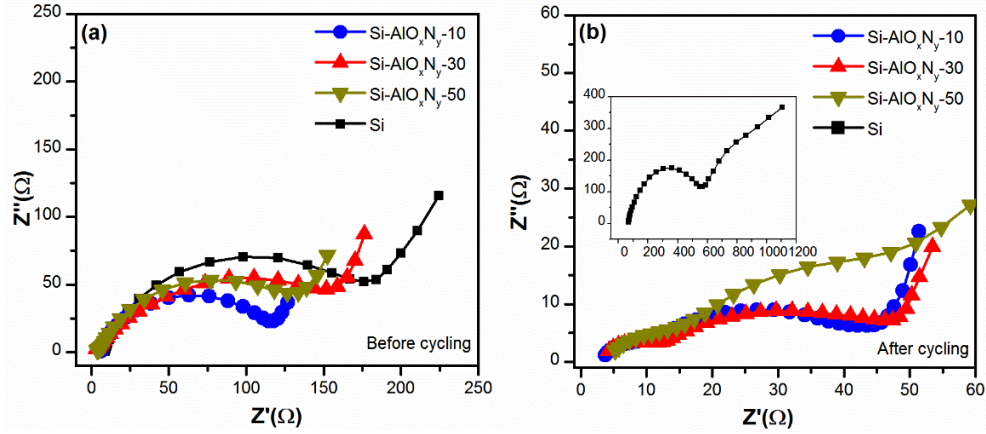
Figure 4-4: Nyquist plots of bare Si electrode and Si electrodes coated with AlO$_x$N$_y$ layers by 10, 30, and 50 ALD cycles (a) before cycling and (b) after 100 charge/discharge cycles.

Table 2: Fitting result of Nyquist plots in Figure 4-4 for Si electrodes with different AlO$_x$N$_y$ layers before and after 100 charge/discharge cycles.

Electrode	Before cycling		After cycling		
	$R_s(\Omega)$	$R_{ct}(\Omega)$	$R_s(\Omega)$	$R_f(\Omega)$	$R_{ct}(\Omega)$
Si	8.0	142.0	65.9	485.1	370.6
Si- AlO$_x$N$_y$-10	5.5	100.0	3.1	30.0	6.4
Si- AlO$_x$N$_y$-30	2.0	134.0	3.1	30.0	7.3
Si- AlO$_x$N$_y$-50	3.0	114.0	3.6	12.1	18.4

To have a better understanding of the mechanism of AlO$_x$N$_y$-coating on Si electrodes, the electrochemical impedance spectroscopy (EIS) analysis was performed on Si electrodes with different AlO$_x$N$_y$ coatings before and after 100 battery cycles. As shown in Figure 4-4a, before cycling, the cell displays a single semicircle at the high frequency, corresponding to the charge-

transfer resistance of the anode surface and the electrolyte, and a straight line at the low frequency, representing the Warburg resistance. Compared to the pristine Si electrode, AlO_xN_y-coated Si electrodes show reduced charge transfer and solution resistances (Figure 4-4), probably due to the good electrical conductivity of the AlO_xN_y coating layer. Si-AlO_xN_y-10 exhibits the smallest charge-transfer resistance of 100 Ω, compared to 142 Ω for bare Si electrodes (Table 2). In Figure 4-4b, all the electrode after cycling shows two semicircles in the high-frequency range, which represent the charge-transfer resistance and SEI resistance, respectively. As seen, AlO_xN_y coated Si electrodes display significantly smaller semicircles in the medium frequency range, suggesting the decreased SEI resistances with AlO_xN_y coating. As a result, in the coated sample, the artificial SEI layer improved the kinetic of the coated Si electrode, which leads to better cycling performance, CE, and capacity retention. The Nyquist profiles are fitted by using the equivalent circuit before cycling ($R_s(R_{ct}Q)W$) and after cycling ($R_s(R_fQ)(R_{ct}Q)W$) to obtain EIS parameters (Table 2). R_s, R_f and R_{ct} represent the resistance of solution (electrolyte), SEI layer, and charge transfer, respectively. Q and W parameters are constant-phase element and Warburg resistance, respectively.
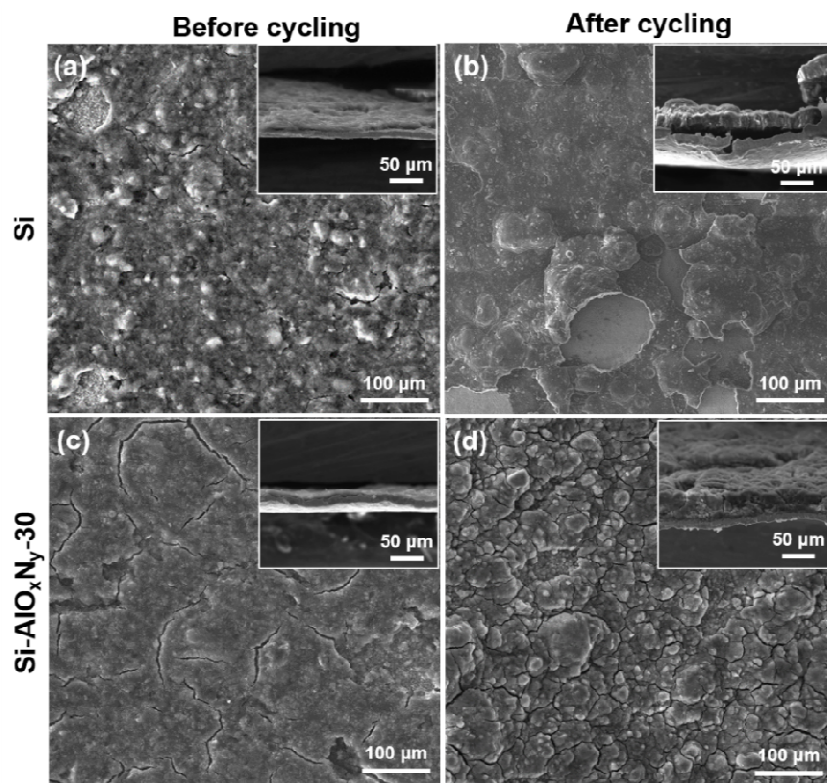
Figure 4-5: The top-view and cross-section -view SEM images of (a, b) pristine Si electrode and (c, d) Si-AlO$_x$N$_y$-30 electrodes (a, c) before and (b, d) after 100 charge-discharge cycles.

Figure 4-5 shows the morphologies of the Si electrodes with and without AlO$_x$N$_y$ coating before and after 100 charge-discharge cycles. Figures 4-5a and 4-5c show that the surface of cycled Si electrode has serious delamination because of Si swelling during the repeated battery charge and discharge processes. Figure 4-5c shows that the Si active material has been detached from Cu current collector, responsible for the fast decay in its electrochemical battery performance. In contrast, the surface morphology of the cycled AlO$_x$N$_y$-coated electrode (Figure 4-5b and 4-5d) maintains the original structure of the fresh electrode, with only little cracks. In the cross-section image, it can be found that the Si active material is still well attached to the Cu current collector, leading to the stable and excellent electrochemical performance of the AlO$_x$N$_y$ coated electrode due to the confinement effect of AlO$_x$N$_y$ in Si volume expansion.
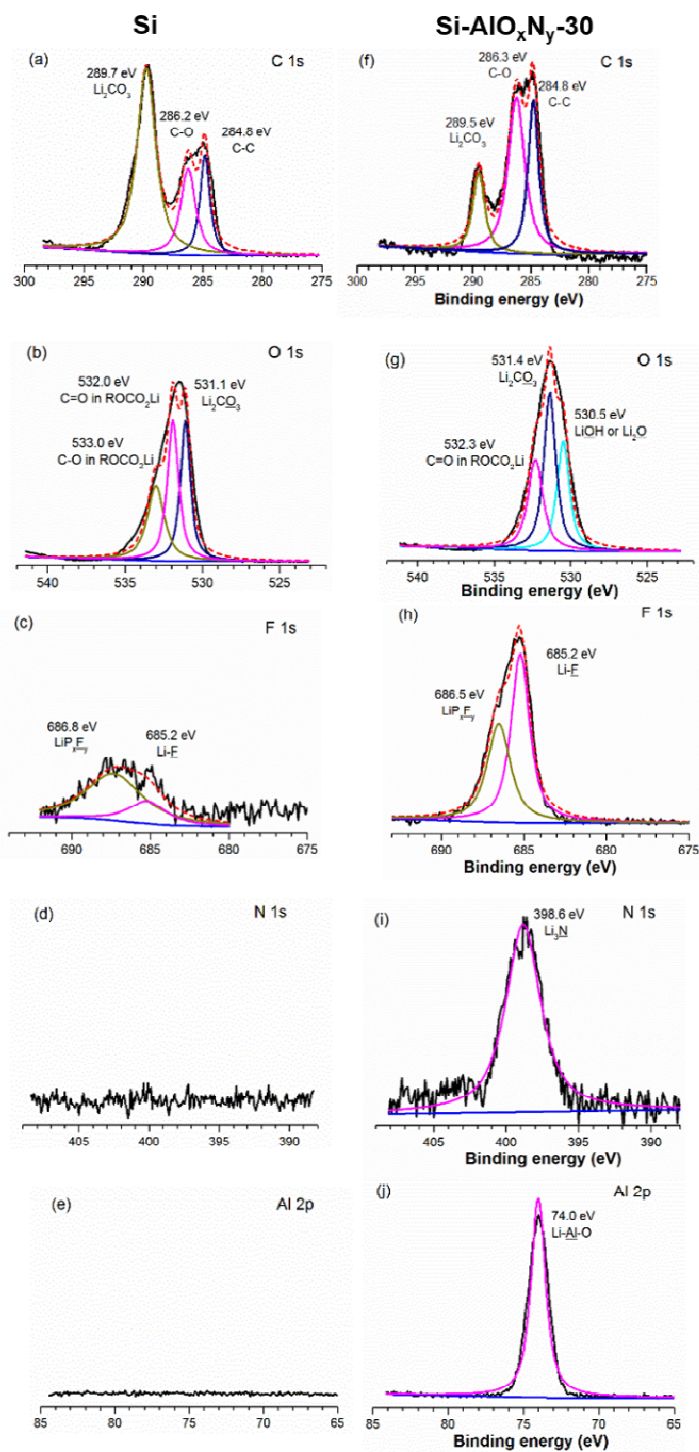
Figure 4-6: (a) C 1s, (b) O 1s, (c) F 1s, (d) N1s and (e) Al 2p spectra of Si electrode without coating after cycling; (f) C 1s, (g) O 1s, (h) F 1s, (i) N1s and (j) Al 2p spectra of Si electrode with AlO_xN_y coating after cycling.

The compositions of SEI layers on Si electrodes with and without AlO_xN_y coating are examined using XPS, and the results are presented in Figure 4-6. Figures 4-6a and 4-6f show the XPS results of the cycled Si electrode with and without AlO_xN_y coating for the C1s peak. The C1s peak can be split into three individual peaks located at Li_2CO_3 (289.7eV), C-O (286.2eV), C-C (284.8eV). Li_2CO_3 is a well-known electrolyte reduction product that comes from the irreversible formation of the SEI layer. Poor CE usually occurs with this reduction product [85]. Comparing the XPS result of the cycled Si electrode with and without AlO_xN_y coating, the AlO_xN_y coated one has a much less Li_2CO_3 than the non-coated one, agreeing with the conclusion from CE and cycling ability (Figure 4-3). As can be seen in Figures 4-6b and 4-6g, O 1s peak also demonstrates the existence of Li_2CO_3. Meanwhile, in the Si electrode with AlO_xN_y (Figure 4-6g), the Li_2O component is detected at 530.5 eV. However, the O peaks are not usually used for quantitative analysis, because the sample may absorb the extraneous oxygen contamination from atmosphere [113].

The signal for LiF in Figure 4-6c and Figure 4-6h is considered an electrolyte decomposition product from the $LiPF_6$ salt, which comes from battery cycling over time[114]. The LiF peak is relatively stronger in AlO_xN_y coated Si electrode than the bare Si electrode, attributed to the firm SEI layer on the electrode resulting in lower Si exposure. Figure 4-6d and 4-6i showed the high-resolution XPS spectra of N1s peak from Si electrode without and with AlO_xN_y after cycling. For the Si-AlO_xN_y electrode after cycling, one peak can be located at Li-N bonding (399.7 eV) [115]. Li-N bonding confirms the presence of Li_3N on AlO_xN_y coated Si after cycling. Li_3N is an ion conductor with very high Li-ion conductivity ($\sigma > 1x10^{-3}$ S cm^{-1}), which comes from a Li-ion transfer reaction through AlO_xN_y coating during cycling[116]. Meanwhile, Figure 4-6j also confirms the Li-Al-O bonding, a well-known excellent Li-ion

conductor [117]. The Li-Al-O comes from the Li-ion reaction with Al-O in AlO_xN_y coating. The artificial SEI layer contains Li_3N and Li-Al-O, which act as the Li-ion pathway to improve the ion transfers while maintaining the electrode mechanical/structural architecture, meanwhile reduces the silicon expansion and lower the interaction of electrode-electrolyte at their interfaces.
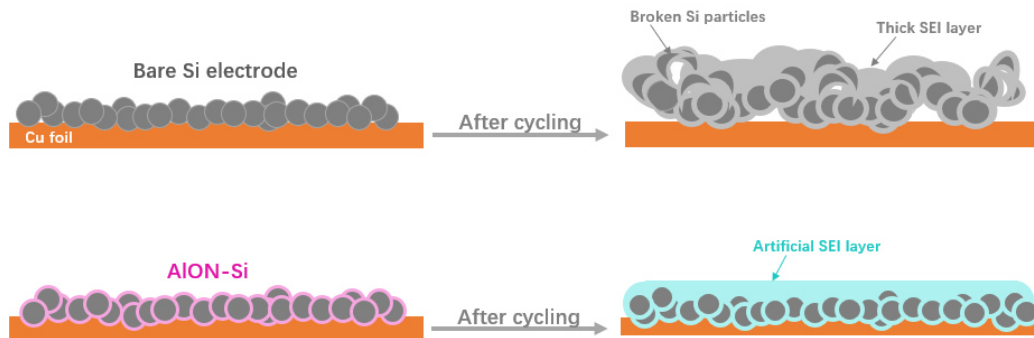
Figure 4-7: Mechanism of the coated and non-coated silicon electrode over cycling.

Figure 4-7 shows the schematic illustration of the coated and non-coated silicon electrode over cycling. The thick SEI layer, broken Si particles, and exfoliation of the Si electrode have been seen after cycling for the bare silicon electrode. For the non-coated electrode, silicon is in direct contact with the electrolyte, causing the electrolyte's rapid decomposition at their interface. This electrolyte decomposition creates an SEI layer, consisting of the electrolyte decomposition byproducts. During charge-discharge, silicon undergoes severe volume expansion, causes the breakage of the as-formed SEI layer and new exposure of silicon to the electrolyte. The exfoliation of the Si electrode from the Cu current collector and the silicon particle breakdown results from the above-mentioned phenomenon.

For the AlO_xN_y-coated Si electrode, the reaction of Li-ion and AlO_xN_y coating over cycles creates an artificial SEI layer contains Li_3N according to the reaction of $4Li+AlN \rightarrow Li_3N+LiAl$ [118]. Li_3N is an ion conductor with very high Li-ion conductivity ($\sigma > 1 \times 10^{-3}$ S cm^{-1}) [119]. The artificial SEI layer improved the coated Si electrode's capacity and kinetic, meanwhile reducing

69

the silicon expansion and lowering the interaction of electrode-electrolyte at their interfaces. The artificial SEI layer performs as the Li-ion pathway to improve the ion transfers while maintaining the electrode mechanical/structural architecture.
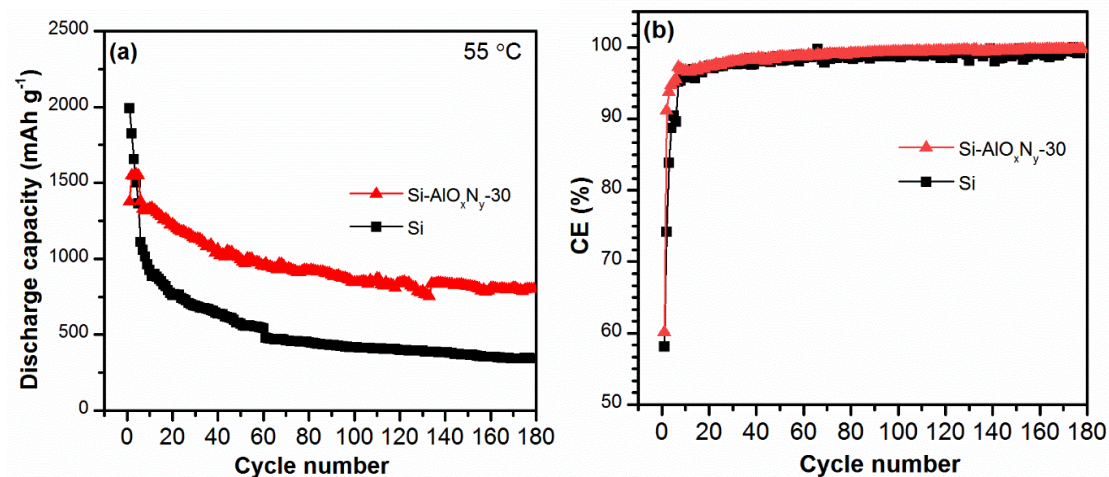
Figure 4-8: (a) Cycling stability and (b) CE of Si electrodes with and without 30-cycle AlO_xN_y coating measured at 55 °C.

The cycling stability of the Si electrode with and without AlO_xN_y coating was further examined at 55 °C, and the results are shown in Figure 4-8a. The bare Si electrode shows a rapid capacity decay in 50 cycles, which is caused by the severe side reaction between Si and the electrolyte at the raised temperatures. As a result, the un-coated Si has a capacity retention of 19.1% after 175 cycles. However, in contrast, Si-AlO_xN_y-30 exhibits much-improved cycle stability and capacity retention of 51.3% over 175 cycles. Furthermore, Si-30 possesses a relatively stable CE of 98-99% over cycling, while bare Si experiences a more fluctuated state in the CE. These results suggest the stable artificial SEI layers enabled by AlO_xN_y coating, which confirm the importance of AlO_xN_y coating to Si anode performances at higher temperatures.

In summary, Si electrodes were coated with AlO_xN_y thin films by PEALD for the first time and applied as the anode for lithium-ion batteries. The electrochemical performance was enhanced due to the electrochemical properties of AlO_xN_y film. The capacity retention of the

AlO_xN_y-coated Si electrode was elevated to 72.3%, compared to 13.3% of bare Si electrode. The capacity remained 1297 mAh g^{-1} at 140 cycles, and capacity retention of 51.3% over 175 cycles at 55 °C, indicating promising cycle stability capability of AlO_xN_y-coated Si electrode. The electrochemical reaction mechanism study and XPS analysis revealed that Li-ion interaction with AlO_xN_y coating over cycles led to the formation of an artificial SEI layer containing Li_3N and Li-Al-O. The artificial SEI layer performed as the Li-ion pathway to improve the ion transfers while maintaining the electrode mechanical/structural architecture and improved the capacity and kinetic of the coated Si electrode. It also suppressed the silicon volume change and lowered the side reactions at the electrode-electrolyte interfaces. This work might open a new pathway to design high-performance Si electrode materials for Li-ion batteries.

Chapter 5: Molecular-Layer-Deposited Tincone: a New Hybrid Organic-Inorganic Material for Protective Coating on Silicon Electrode in Lithium-ion Batteries [‡]

In the previous chapter, the effect of the AlO_xN_y layer coated by the PEALD on the performance of Si anode in LIBs was showed. This chapter aims at further advancing the development and application of multifunctional coating materials for Si anode. Molecular layer deposition (MLD) was adopted to fabricate tincone, a hybrid organic-inorganic material, on Si anode to tackle the Si-based electrode issues. Tin-based materials are well known for their Li-ion storage capability. Moreover, tincone by MLD has flexibility, an excellent feature of protecting films for addressing Si swelling issues.

This chapter is divided into two sections. Section 5.1 describes surface chemistry and process for tincone by MLD and structural and electrochemical properties of tincone alone as electrochemically active material in LIBs. Section 5.2 investigates the utilization of tincone as surface protection on Si anode to obtain enhanced battery stability in LIBs.

5.1 Molecular-Layer-Deposited Tincone: a Hybrid Organic-Inorganic and Electrochemically Active Material for Lithium-Ion Batteries

In this part, a new hybrid organic-inorganic film, tincone, was developed by using molecular layer deposition (MLD), and exhibited high electrochemical activity toward Li storage. The self-limiting growth behavior, high uniformity on various substrates and good Li-storage performance make tincone a promising new anode material for three-dimensional (3D) microbatteries and surface protecting material for LIBs.

3D microbatteries have drawn increasing attention as promising on-board energy storage systems for various emerging miniaturized devices, such as wireless sensors, micro-electromechanical systems, smart cards, and radio-frequency identification tags, due to their high energy density in a limited space and great flexibility in device design and integration [120-122]. Compared to 2D thin-film batteries, 3D microbatteries provide a much larger specific area for active material loading and for electrochemical reactions to occur. Thus, they have enhanced energy density while maintaining high power density due to short Li-ion and electron diffusion paths [120]. Fabrication of 3D microbatteries requires a thin film deposition technique capable of depositing uniform and pinhole-free electrode and electrolyte materials on high-aspect-ratio substrates [123]. ALD is an established thin film deposition method for fabricating conformal thin films on high-aspect-ratio substrates and can realize film thickness control with submonolayer accuracy [54, 124]. ALD is based on saturated gas-solid reactions on the substrates and is achieved by sequential exposure of gaseous precursors on a substrate surface. The past years have witnessed the exponential growth in research development and applications of ALD surface coatings (metal oxides, fluorides, phosphates, and solid electrolytes) to modify electrode-electrolyte interfaces in liquid- and solid-state Li-ion batteries (LIBs), in order to

alleviate side reactions, create stable solid-electrolyte interphase (SEI), and improve the overall electrochemical performance [28, 125-127]. For the manufacturing of 3D microbatteries by ALD, a few successful examples have been demonstrated to use ALD to achieve 3D microbatteries with either liquid [122, 128] or solid electrolytes [129, 130]. However, the limited ALD chemistry and processes for battery electrodes and electrolytes hinder the development of 3D microbatteries. Although research progress has been made to enrich the ALD material library [28], it is still desirable to broaden the ALD deposition processes for new electrode materials with high energy and stable performance for LIB applications.

Analogous to ALD, molecular layer deposition (MLD) is also a thin film technique with self-limiting growth nature but is intended for fabricating organic and organic-inorganic hybrid films, *i.e.* metalcone. Besides precise control over film thickness, MLD provides the advantages of fine-tuning the film's properties, such as chemical, optical, electrical, mechanical, photocatalytic *etc.*, by tailoring the organic chains used in the thin film deposition processes, thus opening a new avenue to design a new group of functional materials at a molecular scale [43, 131, 132]. For battery applications, MLD thin films have been demonstrated as either coating materials or active materials [126, 133]. For example, flexible Alucone coating has been applied on the nano-Si electrode to accommodate its large volume change during lithiation/de-lithiation process, resulting in capacities of nearly 900 mAh g^{-1} and Coulombic efficiency (CE) in excess of 99% over 100 cycles [51]. Moreover, Alucone has been reported as an effective artificial SEI on Li and Na metals to address the long-standing dendrite problem, thus enabling highly stable and efficient metal anodes for LIBs and Na-ion batteries [126]. MLD has also been explored to produce hybrid organic-inorganic anode (lithium terephthalate [134] and titanicones [135]) and cathode (vanadicones [136]) to host Li ions, as summarized in Table 3. Karppinen *et al.* first

reported the deposition of lithium terephthalate ($Li_2C_8H_4O_4$ or LTP) by MLD using Li(thd) and Benzene-1,4-dicarboxylic acid (TPA) as the precursors [134]. These LTP thin films exhibited a self-limiting growth behavior with a MLD window of 200−240°C and growth per cycle (GPC) of 3 Å. Moreover, the LTP thin-film as-deposited at 200°C possessed a crystalline structure and showed excellent rate capability in a $LiPF_6$-based liquid electrolyte [134]. Later on, Kerckhove *et al.* deposited titanicone films at 80-160°C by using tetrakisdimethylaminotitanium (TDMAT) and glycerol (GL) as MLD precursors [135]. The as-deposited titanicone film was in an amorphous state and showed no electrochemical activity towards Li storage, though. Post-treatment at 500°C in an inert (He) and oxidizing (air) atmosphere turned titanicone into an amorphous phase or anatase TiO_2 structure, respectively. The structures obtained by post-treatment in both conditions exhibited electrochemical activity towards Li storage in half-cell testing, *i.e.* using Li metal as the counter electrode. In another study, Kerckhove and co-workers further deposited vanadicone thin films by MLD using tetrakisethylmethylaminovanadium (TEMAV) and GL as the precursors [136]. Despite the success in the MLD process, the as-deposited vanadicone was inactive as a cathode for Li storage and required post-annealing in He and air to gain reversible lithiation/delitiation behaviours. However, post-annealing could easily destroy the film uniformity, which was the intention of using ALD or MLD for 3D microbatteries in the first place, and cause the formation of island structures on the substrates [137, 138]. Although post-annealing on MLD thin films can yield novel composite structures (carbon/metal oxides and carbon/metals) that might be beneficial for some applications (such as photocatalytic) [43, 131, 132], post-treatment in harsh conditions will jeopardize the uniformity of ALD or MLD thin films and should be discouraged for 3D microbatteries.

Table 3. Summary of deposition condition, post-annealing, and electrochemical activity towards Li storage for MLD films.

MLD Film (role in LIBs)	Metal precursor	Organic reactant	Deposition T (°C)	Growth per cycle (Å)	Post annealing	Film crystallinity	Electrochemical activity towards Li storage	Ref.
LTP (anode)	Li(thd)	TPA	200−240	3.0	As-deposited	Crystalline	~ 10 µAh cm^{-2} at 0.05C	[134]
Titanicone (anode)	TDMAT	GL	80-160	0.9-0.2	As-deposited	Amorphous	No	[135]
					Air, 500°C	Anatase TiO$_2$	~ 0.5 µAh cm^{-2} at 1µA	
					He, 500°C	Amorphous	~ 0.6 µAh cm^{-2} at 1µA	
Vanadicone (cathode)	TEMAV	GL	80-180	1.2-1.5	As-deposited	Amorphous	No	[136]
					Air, 500°C	Crystalline V$_2$O$_5$	~1.0 µAh cm^{-2} at 1C	
					He, 500°C	Amorphous	~1.2 µAh cm^{-2} at 1C	
tincone (anode)	TDMASn	GL	100	2.0	As-deposited	Amorphous	450 mAh g^{-1} for tincone/N-CNTs composite at 0.1 A g^{-1}	Herein

Lithium terephthalate – LTP; Benzene-1,4-dicarboxylic acid – TPA; Tetrakisdimethylaminotitanium – TDMAT; Glycerol – GL; Tetrakisethylmethylaminovanadium – TEMAV; Temperature – T; Benzene-1,4-dicarboxylic acid – TPA; Tetrakis(dimethylamino)tin (IV) – TDMASn.

Herein, MLD-deposited tincone was reported, without any post-treatment, exhibited excellent electrochemical activity for Li storage, making it a new promising organic-inorganic hybrid anode material for 3D microbatteries. tincone was deposited at 100 °C using tetrakis(dimethylamino)tin (IV) (TDMASn) and glycerol (GL) as MLD precursors. The film thickness of tincone had a linear dependence on MLD cycles, yielding a GPC of ~ 2.5 Å on the Si substrate. The tincone represents a new class of anode materials for LIBs and might find potential applications in 3D microbatteries. It is expected that this work will stimulate further research in the development of organic-inorganic hybrid materials by MLD for energy storage applications.

5.1.1 Experimental

5.1.1.1 Deposition of tincone by MLD

The deposition of tincone by MLD was performed at 100°C in a commercial ALD system (GEMStarTM XT Atomic Layer Deposition System, Arradiance, USA) using (tetrakis(dimethylamino)tin (IV), (TDMASn, Strem Chemicals) and Glycerol (GL, Sigma Aldrich) as the precursors. The details of MLD steps were illustrated in Chapter 2. Using this reaction sequence, the thickness of tincone deposited on N-CNTs was controlled by varying the number of MLD cycles. Si wafers, stainless steel (SS) current collectors, and nitrogen-doped carbon nanotubes (N-CNTs) were used as the substrates for tincone deposition. Si wafers and SS were used as received. N-CNTs were prepared by following a chemical vapor deposition process reported previously [139]. N-CNTs powders were first dispersed in an alcohol solution in an ultrasonic bath and then evenly dropped on an aluminum (Al) foil. After dried at room temperature, the N-CNTs coated Al foil was cut into pieces and put into the ALD chamber for tincone deposition. After the deposition, tincone/N-CNTs were carefully scraped off the aluminum foil for structural and electrochemical characterizations.

5.1.1.2 Material characterizations

The thickness of tincone on the Si substrate was obtained by taking an average of five measured data points on the Profilometer. The microstructure of tincone/N-CNTs was characterized using a high-resolution transmission electron microscope (FEI F30). Sn L_3-edge spectrum analysis was performed at the Soft X-ray Micro-characterization Beamline (SXRMB) of Canadian Light Source (CLS), and data were recorded using surface-sensitive total electron yield (TEY) method with a probing depth of 1–10 nm. After background correction, the spectra were normalized to the edge jump. The Near Edge X-Ray Absorption Fine Structure (NEXAFS) measurement of C and O K-edges was performed at the spherical grating monochromator (SGM) beamline of the CSRF in a vacuum chamber at 10^{-8} torr, and data were recorded using the TEY method. Tincone deposited on silicon wafers was used for the XAFS test. Commercial SnO_2, SnO, and Sn (VWR) were used for comparison with tincone. The XAFS test is done with the help of Keegan Adair, Zhiqiang Wang and Tsun-Kong Sham in the Department of Chemistry at the University of Western Ontario.

5.1.1.3 Electrochemical measurement

Electrochemical evaluation of tincone deposited on SS and N-CNTs substrates was carried out in coin cells (CR2032) using lithium metal foils as the counter electrode. tincone/SS was directly used as the electrode. To prepare the tincone/N-CNTs electrode, tincone/N-CNTs powders, Super P (TIMCAL), and carboxymethyl cellulose (CMC, 5 wt% aqueous solution, TIMCAL) with a weight ratio of 7:2:1 were mixed thoroughly in an agate mortar to form a uniform slurry. The slurry was then cast on a copper foil and dried at 60°C in a vacuum oven overnight. The dried electrode was cut into round shapes with a diameter of 1.27 cm. The electrolyte was 1.3M $LiPF_6$ in ethylene carbonate (EC)/diethylene carbonate (DEC) (3:7 *v/v*). The cycling performance of the assembled coin cells was evaluated in a voltage range of 0.01-

3.0 V on a Neware BTS 4000 battery tester. Cyclic voltammetry (CV) was measured at a sweep rate of 0.2 mV s^{-1} on a Biologic VSP electrochemical workstation. Electrochemical impedance spectroscopy (EIS) was measured over a frequency range of 100 kHz to 0.01 Hz.

5.1.2   Results and discussion

Figure 5-1 illustrates the proposed mechanism of TDMASn and GL half-reactions [136, 140]. In the half-reaction (a), TDMASn molecules react with hydroxyl (-OH) surface species, releasing dimethylamine as the reaction by-product. In half-reaction (b), GL molecules react with dimethylamido surface species to release the dimethylamine by-product and convert the surface functional groups back to hydroxyl species. The half-reactions (a) and (b) form one MLD cycle. The thickness of tincone films on the Si substrate shows a linear relation with MLD cycles (Figure 5-2a). By linearly fitting the data in Figure 5-2a, the growth per cycle (GPC) of tincone is determined to be 2.5 Å at 100 °C.
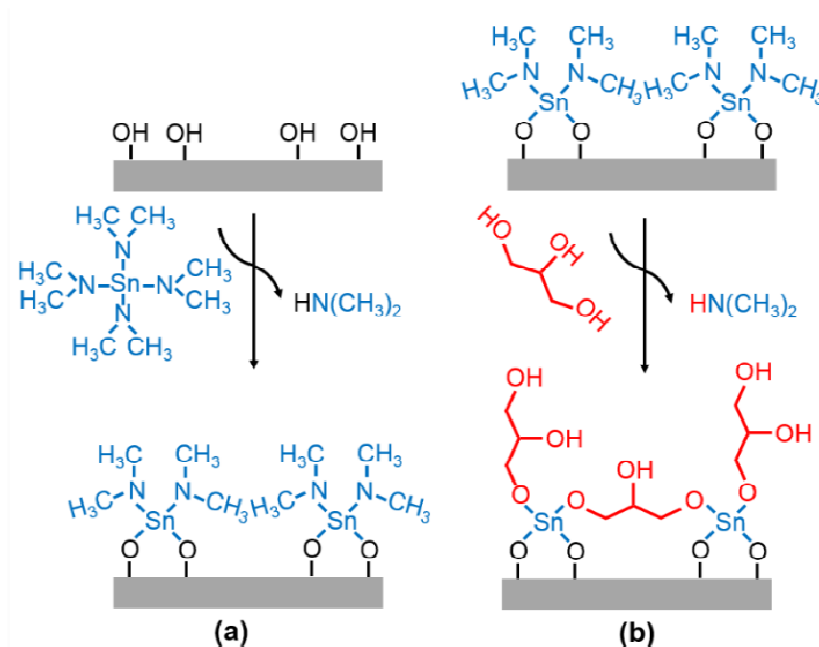
Figure 5-1: Proposed reaction mechanism of tincone deposited by MLD using (a) TDMASn half-reaction and (b) glycerol (GL) half-reaction in one MLD cycle.
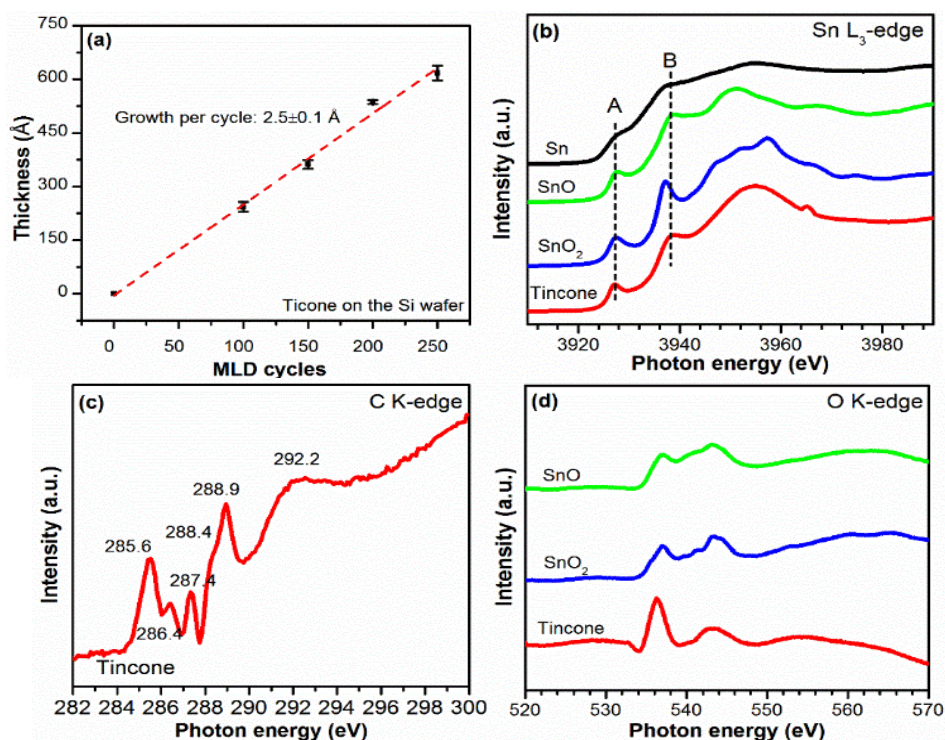
Figure 5-2: (a) Film thickness as a function of MLD cycles for tincone deposited on the Si substrate at 100 °C; (b) Sn L3-edge (c) C K-edge, and (d) O K-edge XANES of tincone on the Si substrate, in comparison with Sn, SnO, and SnO$_2$ reference samples (if applicable).

The chemical structure of tincone was analyzed by synchrotron radiation technique, and the results are presented in Figure 5-2b and d. Figure 5-2b shows the TEY spectrum of tincone at the Sn L$_3$-edge, in comparison with those of Sn, SnO, and SnO$_2$ reference samples. Sn metal shows no white line at the L$_3$-edge, due to the completely filled 4d and 5s atomic orbitals with the increase of the oxidation state of Sn, the first two features A and B become sharper. SnO$_2$ also shows more features than Sn and SnO. The TEY spectrum of tincone is obviously different from that of the Sn metal, suggesting an overall higher valence state of Sn ions in the organic-inorganic hybrid film than in metallic Sn [141]. Compared to SnO$_2$ and SnO, tincone is featured with two broader pre-edge peaks at ~ 3927.6 (peak A) and ~ 3937.4 eV (peak B), revealing a more disordered structure of Sn ions in tincone. The position of peak B in the Sn L$_3$-edge

80

XANES spectrum of tincone lies between those for SnO_2 and SnO, indicating the Sn oxidation state between 2+ and 4+ in the tincone film [142]. The interaction between Sn and GL molecular chains in tincone could be unveiled in the C K-edge and O K-edge spectra (Figure 5-2c and 5-2d), in which the change of electronic structure, the local chemistry environment, and several featured peaks are clearly observed. In Figure 5-2d, the XANES spectrum of the C K-edge can be divided into two parts. The peaks between 285.6 and 288.9 eV are related to $1s \rightarrow \pi^*$. The peaks at 285.6 and 286.4 eV are related to the $N\text{-}CH_3$ bond at the surface of tincone [143], the peak at 287.4 eV originates from the C-OH bond in GL molecular chains, and the peaks at 288-289 eV are due to C bound to CH, CH_2, and CH_3 [144]. In the second part, the broad peak centered at 292.2 eV is related to $1s \rightarrow \sigma^*$ [28] and can result from σ^* state C-C and C-O groups. Moreover, the O K-edge spectral shape at 536 eV for tincone is clearly different from that of SnO_2 and SnO and corresponds to the C-OH group [145]. Synchrotron radiation analysis confirms the successful deposition of tincone by MLD, illustrated in Figure 5-1.
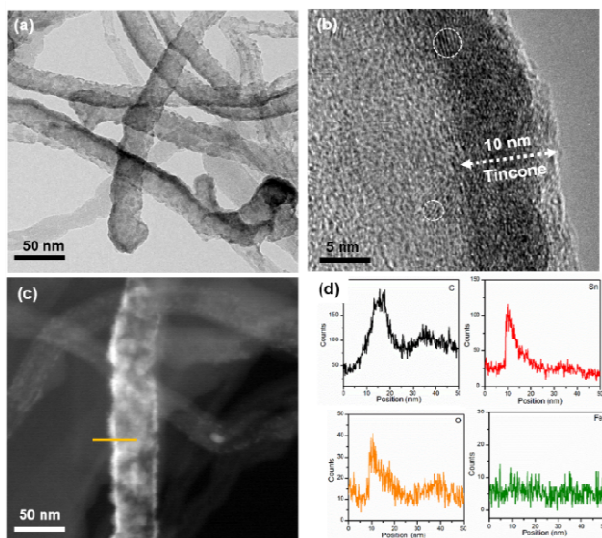
Figure 5-3: (a) TEM, (b) HRTEM, and (c) STEM images of tincone on NCNTs; (d) EDX line-scanning for C, Sn, O, and Fe in the location marked in (c) (Fe was the catalyst used for the growth of N-CNTs).

Tincone deposited on SS and N-CNTs substrates was used to assess its electrochemical

activity towards Li storage in half-cells. The morphology and structure of tincone/N-CNTs are shown in Figure 5-3. As seen in Figure 5-3a, tincone/N-CNTs have diameters of 30-50 nm, and tincone completely covers the surface of N-CNTs, due to the reaction mechanism of the MLD process (Figure 5-1). The thickness of tincone on N-CNTs is measured as about 10 nm under the HRTEM image (Figure 5-3b). Moreover, HRTEM observation shows no long-range ordering in the tincone, indicating its amorphous structure and consistent with the synchrotron radiation analysis (Figure 5-2). It is interesting to note that ultra-small clusters with short-range order showed up in the tincone matrix during the HRTEM operation, as circled in Figure5-3b. These crystalline clusters are believed to result from electron beam-induced crystallization of SnO or SnO_2 or both in the tincone film [140]. EDX line scanning under STEM mode reveals strong peaks of C, Sn, and O on the surface of N-CNTs, confirming the uniform deposition of tincone (Figure 5-3c and 5-3d).

The electrochemical performance of tincone on SS and N-CNTs substrates are shown in Figure 5-4. The CV curves of tincone/SS exhibit two pairs of reversible oxidation and reduction peaks located at ~ 0.8V/1.2V and 0.2V/0.5V, respectively, which are quite similar to those for SnO_2 [146-148]. The oxidation peak at 0.8V might be assigned to the conversion reaction of tincone to Sn ($4Li^+ + SnO_x + 4e^- \rightarrow Sn + 2Li_2O$), while the peak at 0.2V could be attributed to the alloying reaction of Sn and Li ($xLi + Sn + xe^- \rightarrow Li_xSn$) [146-148]. These reactions are reversed in the reduction process. Figure 5-4a reveals that the as-deposited tincone is electrochemically active for Li-ion storage, albeit the exact reaction mechanism of tincone needs to be clarified in the future.
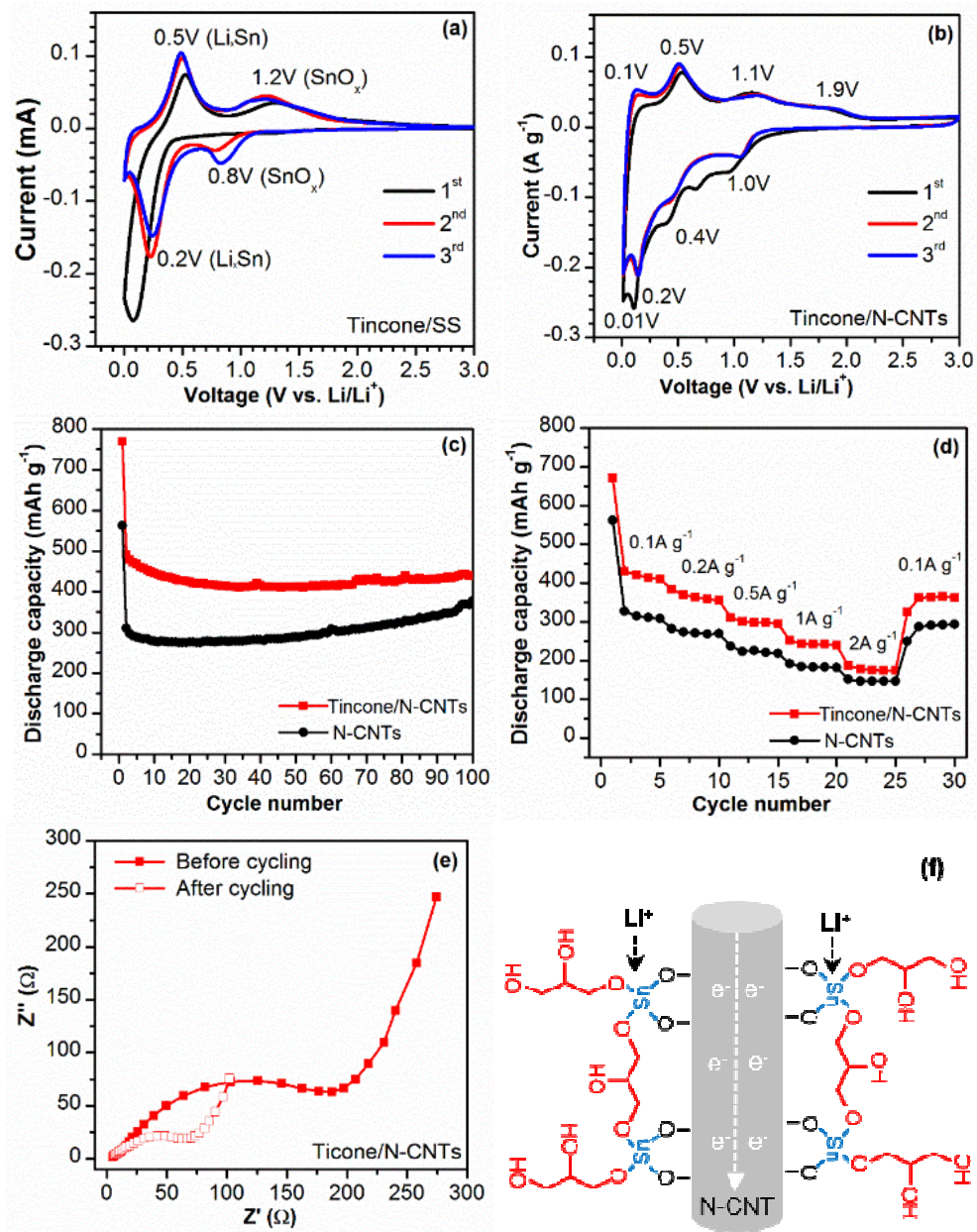
Figure 5-4: Cyclic voltammetry (CV) curves of (a) tincone/SS and (b) tincone/N-CNTs measured at 0.1 mV s-1; (c) cycling stability and (d) rate capability of tincone/N-CNTs, in comparison to N-CNTs; (e) Nyquist plots of tincone/N-CNTs before and after cycle; and (f) schematics of tincone/N-CNTs for Li storage.
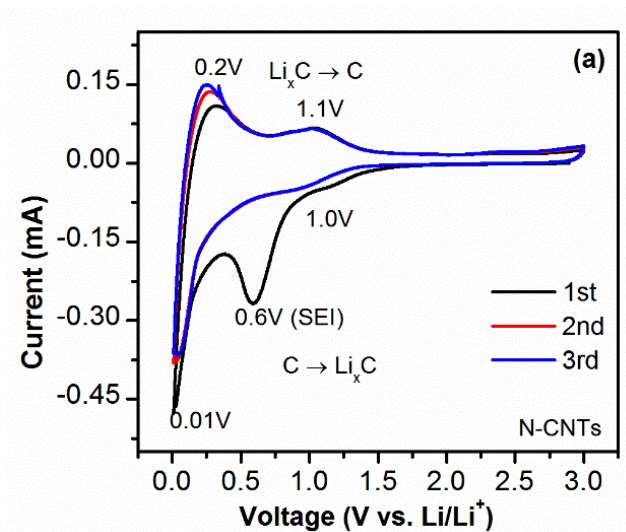
Figure 5-5: CV curves of N-CNTs measured at 0.1 mV s^{-1} in the first three cycles.
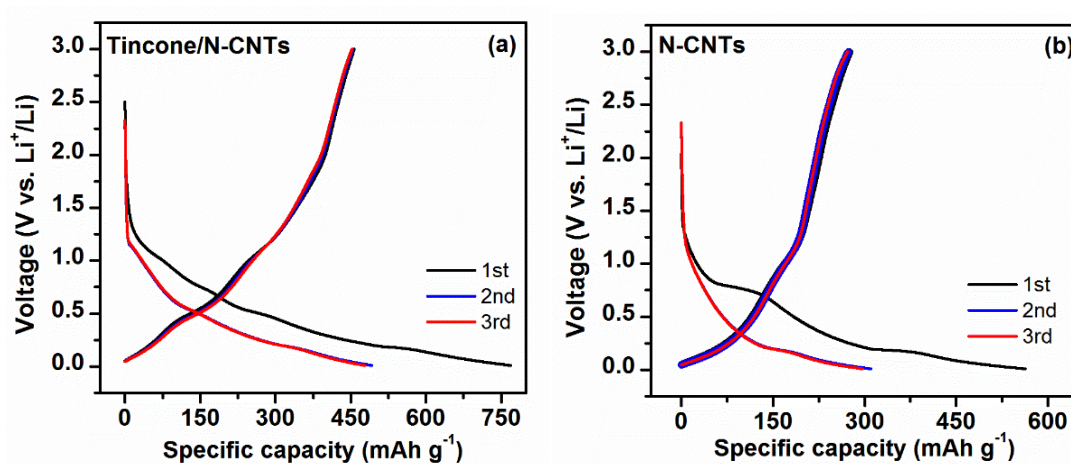
Figure5-6: Charge-discharge curves of (a) tincone/N-CNTs and (b) of N-CNTs measured at 0.1 A g^{-1} in the first three cycles.

The CV curves of tincone/N-CNTs indicate mixed oxidation and reduction peaks from both N-CNTs and tincone (Figure 5-4b), in comparison to Figure 5-4a and N-CNTs alone (Figure 5-5). This agrees with the multiple plateaus in the charge-discharge curves of tincone/N-CNTs (Figure 5-6). While tincone/N-CNTs show general consistency with tincone/SS in its electrochemical behavior, the oxidation and reduction peaks for tincone/N-CNTs are better resolved than those for tincone/SS. For example, during the reduction cycle, the peaks at 0.1 V

and 1.1V could be due to the de-lithiation of Li_xC (carbon nanotubes), while the one at 0.5 V corresponds to de-lithiation of Li_xSn to Sn and the ones at 1.1 V and 1.9 V might be attributed to the phase transition from Sn to SnO_x [146-148]. Moreover, tincone/N-CNTs exhibits a reversible capacity of 490.0 mAh g^{-1} in the second cycle and relatively stable performance over 100 cycles with 89% capacity retention (*vs.* the second-cycle discharge capacity), as seen in Figure 5-4c. The capacity of tincone/N-CNTs composite is much higher than that of N-CNTs alone, suggesting the excellent Li-ion storage performance of tincone. Furthermore, tincone/N-CNTs show good rate capability and can deliver a reversible capacity of 432.7, 368.7, 301.0, 242.1, and 173.2 mAh g^{-1}, at a current density of 0.1, 0.2, 0.5, 1.0, and 2.0 A g^{-1}, respectively.
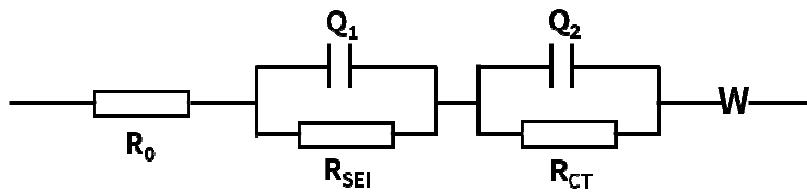
Figure 5-7: Equivalent circuit for fitting EIS data in Figure 5-4e. R_0: solution resistance; R_{SEI}: SEI resistance; R_{CT}: charge transfer resistance; W: Warburg impedance.

Table 4: Fitting result of EIS test for tincone/N-CNTs electrode before and after 100 cycles.

	$R_0 (\Omega)$	$R_{SEI} (\Omega)$	$R_{CT} (\Omega)$
Before cycling	2.6	12.5	125.4
After 100 cycles	3.4	24.3	27.6

Electrochemical impedance spectroscopy (EIS) measurement was performed on tincone/N-CNTs before cycling and after 100 cycles, and are shown in Figure 5-4e. The EIS curves consist of one semicircle in the high-frequency range, corresponding to the SEI resistance (R_{SEI}) and/or charge transfer resistance (R_{CT}), and an inclined line in the low-frequency region, assignable to

Warburg impedance related to the diffusion of Li ions into the electrode [149]. EIS fitting is using an equivalent circuit (Figure 5-7), Q_1 and Q_2 represent the constant phase element. The fitting result shows that R_{SEI} and R_{CT} are 24.3 and 27.6Ω, respectively, suggesting the good kinetics in tincone/N-CNTs (Table 4). The excellent cycling and rate capability of tincone/N-CNTs can be attributed to the three main reasons: (1) The Sn ions in tincone provide a high Li-ion storage capacity and contribute to the improvement of specific capacity in tincone/N-CNTs. It should be noted that the storage capacity could be further increased by applying more MLD cycles to increase the thickness of tincone on N-CNTs; (2) The unique organic-inorganic hybrid structure of tincone might provide a flexible matrix to accommodate the volume change of Sn (>300% volume variation) during the lithiation and de-lithiation process [150].

Previous studies have shown that the incorporation of polymer chains in Alucone added flexibility into the hybrid films, and thus could better buffer the mechanical stress induced by lithiation [51, 131]. Sn and SnO_2 are known for their high Li storage capacities but suffer from poor cycling stability due to large volume expansion resulting from lithiation. The bonding of Sn ions with GL molecular chains in the MLD tincone might provide a new pathway to address the volume change of Sn-based anode at the molecular level; (3) The N-CNTs provide excellent electronic diffusion pathways to tincone to allow fast electrochemical reactions to occur. It is expected that the MLD tincone can find applications as an anode material for 3D microbatteries.

In conclusion, organic-inorganic hybrid tincone thin film was deposited by MLD using TDMASn and glycerol as the precursors. The tincone film exhibited linear dependence on MLD cycles, giving a growth per cycle of 2.5Å at a deposition temperature of 100°C. The as-deposited tincone film was amorphous and possessed electrochemical activity towards Li storage on both SS and N-CNTs substrates. tincone/N-CNTs exhibited excellent cycling stability and rate

capability, and improved discharge capacity of 450 mAh g^{-1}, in comparison to 300 mAh g^{-1} for N-CNTs alone. MLD deposited tincone with good uniformity and electrochemical activity is expected to find potential application in 3D microbatteries as an anode material. Moreover, this work can be extended to synthesize other electrochemically active organic-inorganic hybrid films (such as Si-based metalcone) for battery applications.

5.2 Molecular-Layer-Deposited Tincone: a Multifunctional Coating Material for Silicon Anode in Lithium-ion Batteries

In the previous section, the MLD process for tincone was developed and confirmed the electrochemical activity of tincone for Li-ion storage. In the next step, evaluating tincone as a multifunctional protective coating on the Si electrode will be investigated. For this purpose, MLD was used to deposit tincone on the Si electrode and investigated the electrochemical performance of the battery. To the best of our knowledge, this is the first time tincone used as a protecting film for Si anode.

Previous studies of MLD protection of Si anode worked on alucone as the protecting agent. Piper *et al.* developed MLD alucone coating on Si using a different precursor, hydroquinone coupled with trimethylaluminum. They created novel coating chemistries to maintain the surface of silicon (Si) electrodes through MLD and accommodate volume fluctuations during electrochemical reactions. The coating's flexibility allows for volumetric variations to be accommodated while maintaining the mechanical integrity of the Si electrodes. They showed a reversible Si anode capable of high performance and rate by applying this durable and conductive trimethylaluminum-hydroquinone coating, reaching over 200 cycles with capacities of approximately 1500 mAh g^{-1} [52].

Another work by Ban *et al.* showed an *in situ* TEM study on both uncoated and alucone-coated Si nanoparticles to get a more profound knowledge of the effect of MLD coating on the performances of Si nanoparticles. Their findings show that alucone-coated Si nanoparticles exhibit rapid, thorough, and highly reversible lithiation behaviors linked with the alucone coating's mechanical flexibility and fast Li$^+$ conductivity [151, 152].

In our study, tincone was applied as a protective film for Si anode to test the battery

performance. In this section, the same MLD procedure was used as of section 5.1 and applied the tincone coating on the Si electrode. As a result, the tincone film enhanced the electrochemical properties of Si anode due to its multifunctional feature. Using tincone as a protective film for Si broadened the usage range of coating materials fabricated by the MLD method.

5.2.1   Experimental Section

5.2.1.1   Electrode fabrication

The Si electrodes were prepared by mixing Si nanoparticles (50 nm) with Super P and carboxymethyl cellulose/styrene-butadiene rubber (CMC/SBR) in water with the wt.% ratio 7:2:1 in an aqueous solution to form a uniform slurry. Then electrode slurry was painted on Cu-foil and dried overnight in a vacuum oven at 80°C.

5.2.1.2   MLD coating

The deposition of tincone by MLD was performed at 100°C in a commercial ALD system (GEMStarTM XT Atomic Layer Deposition System, Arradiance, USA) using (tetrakis(dimethylamino)tin (IV), (TDMASn, Strem Chemicals) and Glycerol (GL, Sigma Aldrich) as the precursors. The detail of the MLD process was explained in chapter 2. Using this reaction sequence, the thickness of tincone deposited on the Si electrode was controlled by varying the number of MLD cycles. For comparison and test purposes, steps are repeated for 10/30/50/100 cycles to deposit tincone films on the Si electrode, named as Si-tincone 10/30/50/100.

5.2.1.3   Battery assembling and measurement

After MLD coating, the electrode was cut into a round shape with a diameter of 12 mm and loaded into CR2032 cell configuration cells for electrochemical testing. The bare Si electrode and Si-10/30/50/100 were used as the cathode, Li metal as the anode, and polyethylene (Celgard) as the separator. The electrolyte was 1.3 M $LiPF_6$ in ethylene carbonate: diethyl carbonate (EC:

DEC, 3:7, *v/v*) with 13 vol.% of fluoroethylene carbonate as the additive. The cells were assembled in an Ar-filled glove box (H$_2$0~ 0.1 ppm, O$_2$ ~0.1 ppm). The cycling performance of the coin cells was evaluated on a Neware BTS 4000 battery tester, and electrochemical impedance spectroscopy (EIS) was measured on a potentiostat/galvanostat station (SP-150, Biologic). All the electrode was cycled in a voltage range of 0.01-1.5 V (1C = 3590 mA g^{-1}).

5.2.1.4 Characterization

The morphology and structure of Si and Si-tincone electrodes were characterized by using a SEM (Tescan MIRA3 FEG-ESEM) and high-resolution transmission electron microscopy (HRTEM, JEOL 2010F) analysis. The HRTEM test is done by Carmen Andrei at McMaster University. X-ray photoelectron spectroscopy (XPS) was measured on an Axis Ultra DLD (Kratos Analytical). The XPS test is done with the help of Michael Wang in 4D labs at Simon Fraser University.

5.2.2 Result and discussion

Figure 5-8a, illustrated the proposed reaction mechanism of tincone deposited on Si by MLD. The reaction mechanism of this procedure was discussed in section 5.1.2. 40 cycles tincone was deposited on the Si electrode for the usage of STEM investigation. Figure 5-8b shows the TEM image of the tincone coated Si particle. As seen, the Si particle was covered by uniform thin tincone film. In the STEM image (Figure 5-8c), the coating layer was estimated with a thickness of 10 nm, which agrees with the number of cycles in MLD. An elemental mapping test by energy-dispersive X-ray spectroscopy (EDS) was taken to further confirm the element distribution on Si particles. Figure 5-8 showed the uniform distribution of Sn and O elements on the surface of the Si electrode, confirming the formation of tincone coating. The XPS analysis is shown in Figure 5-8h. The results confirmed the existence of Sn, C, and O

elements from the tincone coating. The deconvolution of the Sn 3d peak has a peak located at 386.9 eV, which is related to the Sn-O bonding in tincone film. The O 1s spectrum also exhibited Sn-O bonding at 530.7 eV that agrees with the previous findings [153]. Further EDX line scanning under STEM mode (Figure 5-9) also verifies the distribution of Sn and O elements across the Si particles. The above results suggest the successful coating of the tincone layer on Si particles by the MLD method.
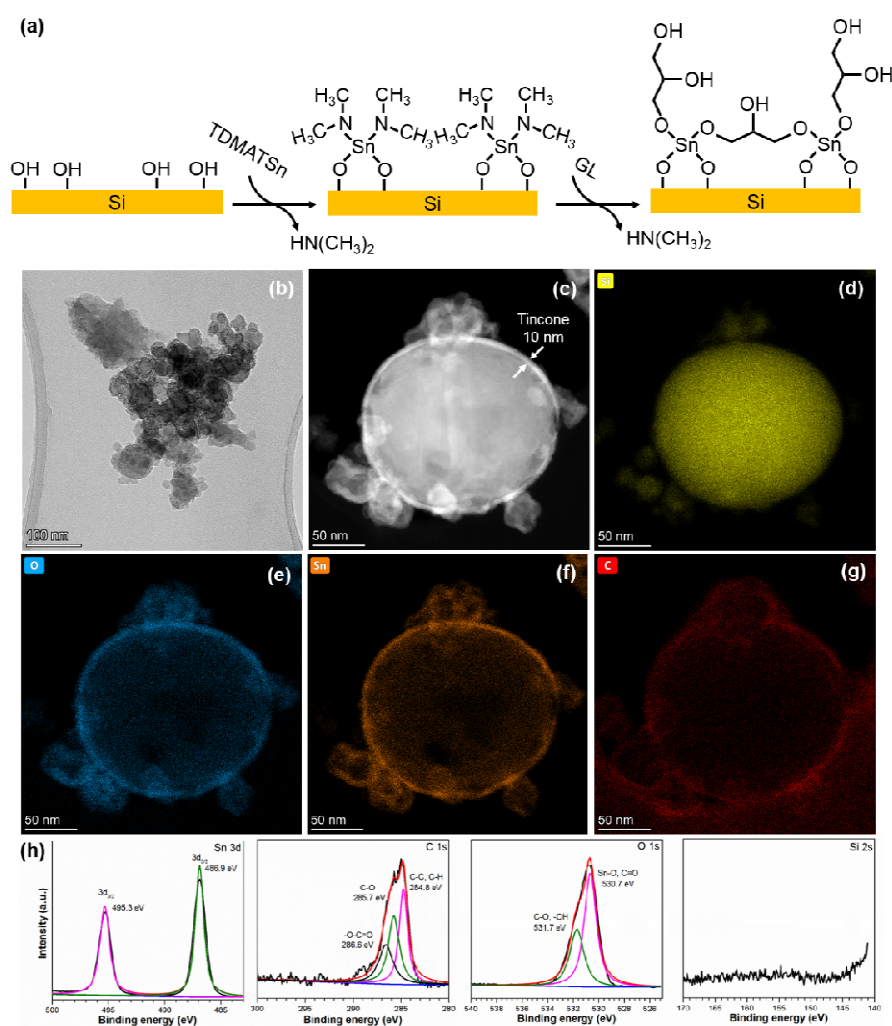
Figure 5-8: (a) Proposed reaction mechanism of tincone deposited on Si by MLD, (b) TEM image of tincone on Si particles, (c-g) STEM and elemental mapping of tincone coated Si particles, (h) XPS analysis of tincone coated Si electrode.
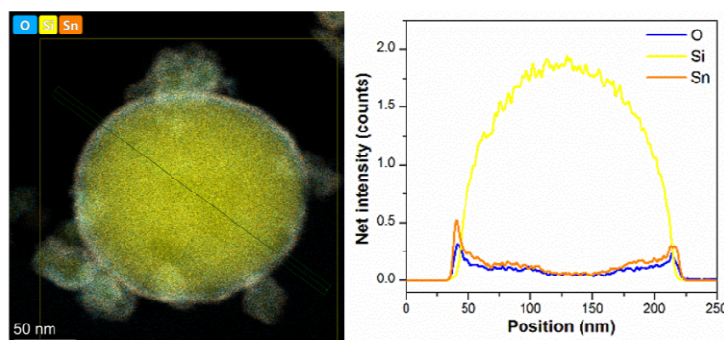
Figure 5-9: Elemental mapping and line scanning of tincone coated Si particles.

Figure 5-10 shows the high-resolution TEM images of Si nanoparticles coated with 40 cycles of tincone. The HRTEM images show an amorphous thin film distributed evenly over the Si particles, attributed to the formation of protecting layer of tincone with a thickness of about 10 nm. The inner part shows the lattice structure of the Si particle. The surrounding tincone film shows a short-range ordered lattice that is believed to have resulted from electron beam-induced crystallization of SnO/SnO_2 in the tincone film.
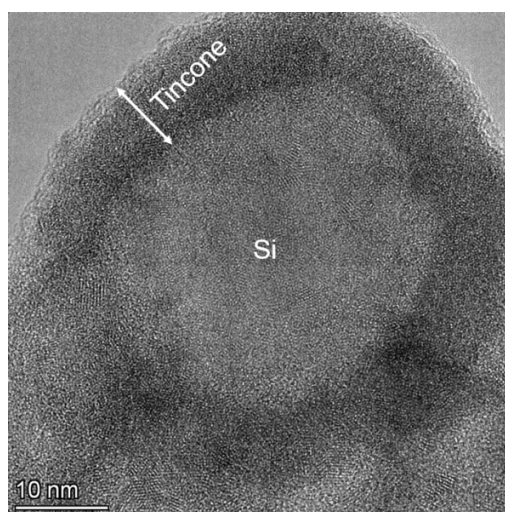
Figure 5-10: The HRTEM image of the tincone coated Si particles.

Figure 5-11 shows the cycling performance of the Si electrode with different thicknesses of tincone coatings. As can be seen in the result, the cycling performance of the Si electrode with

tincone coatings depends on the coating thickness, as illustrated in Figure 5-11a. Bare Si, Si-tincone-10, Si-tincone-30, Si-tincone-50, and Si-tincone-100 exhibit high discharge capacities of 1584.9, 2100.9, 2487.3, 1575.2, and 1584.4 mAh g^{-1}, respectively, after the first 3 initial cycles of activation. The Si-tincone-30 shows the highest discharge capacity in the first cycle among samples, revealing the prominent effect of tincone coating as artificial SEI film in less Li-ion consumption. The capacity retention for bare Si, Si-tincone-10, Si-tincone-30, Si-tincone-50, and Si-tincone-100 after 110 cycles is 23%, 73%, 70%, 81% and 53%, respectively. In summary, the optimal tincone coating thickness is ~ 8 nm reached by using 30 MLD cycles (Si-tincone-30).

The CE of all the samples is compared in Figure 5-11 b. The CE in the first cycle for bare Si and Si-tincone-30 is 66% and 57%, respectively. For the tincone coated Si, the CE is lower than the uncoated one because the tincone coating has Li-ion storage ability, in which more lithium ions are consumed in the discharge process. The CE was stabilized after 10 cycles, and the average CE is above 98% for all Si-tincone samples. The improved CE might be ascribed to the fact that the artificial SEI of tincone coatings could serve as a physical barrier, suppressing the structural degradation of the silicon. However, the bare Si electrode exhibited an unstable CE, which means that the Si electrode has more side reactions and decomposition.

Figure 5-11c presents the rate capabilities of all the samples at various current densities of 0.05 C, 0.1 C, 0.5 C, 1 C, 2 C, and 0.05 C again. Si-tincone-30 shows the best capability and delivers a reversible capacity of 1750, 1340, 1060, 650, and 220 mAh g^{-1}, at a current density of 0.05 C, 0.1 C, 0.5 C, 1.0 C, and 2.0 C, respectively. In comparison, the bare Si shows 1200, 850, 590, 340, and 65 mAh g^{-1} for the current densities of 0.05 C, 0.1 C, 0.5 C, 1.0 C, and 2.0 C, respectively. When the current density returns to 0.05 C, the Si-tincone-30 shows the highest discharge capacity of 1507 mAh g^{-1}.

The first cycle of charge and discharge profiles of Si anode with and without tincone coating has shown in Figure 5-12. The Si anode with tincone coating shows two plateaus at ~ 1.2 V related to the conversion reaction of tincone and at 0.5 V, attributed to the alloying reaction of tincone [153]. The charge-discharge curve results are aligned with the findings in tincone electroactivity properties.
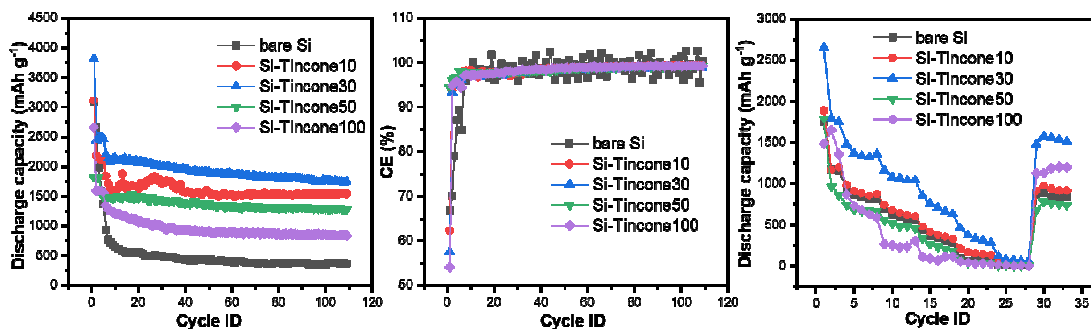
Figure 5-11: (a) cycling performance, (b) CE, and (c) rate test for the Si electrode with and without tincone coating.
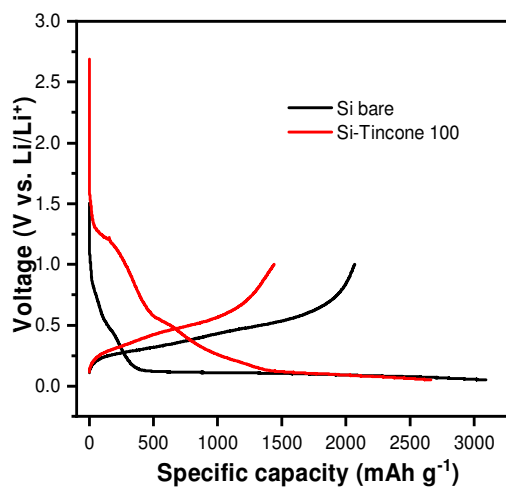
Figure 5-12: Charge-discharge curves of Si electrode with and without tincone coating in the first cycle.

Figure 5-13 illustrates the morphology of the Si electrodes with and without tincone coating before and after 100 charge-discharge cycles. Figures 5-13a and 5-13b show that during

94

the repeated process of charging and discharging, delamination of the electrode's surface occurs due to the silicon's swelling during the operation. In addition, figure 5-13b shows that the Si active material has been detached from the Cu current collector, causing the decay in the electrochemical performance of the battery. In contrast, the surface morphology of the cycled tincone-coated electrode (Figure 5-13c and 5-13d) was maintained as the original structure of the fresh electrode, with only tiny cracks. In the cross-section view of the uncoated Si electrode (Figure 5-13e and 5-13f), after 100 cycles, the Si electrode faced a huge swelling issue; however, the thickness of the tincone coated electrode did not change after cycling. Because of the confinement effect of tincone on Si volume change, the tincone coated electrode exhibits outstanding electrochemical performance.
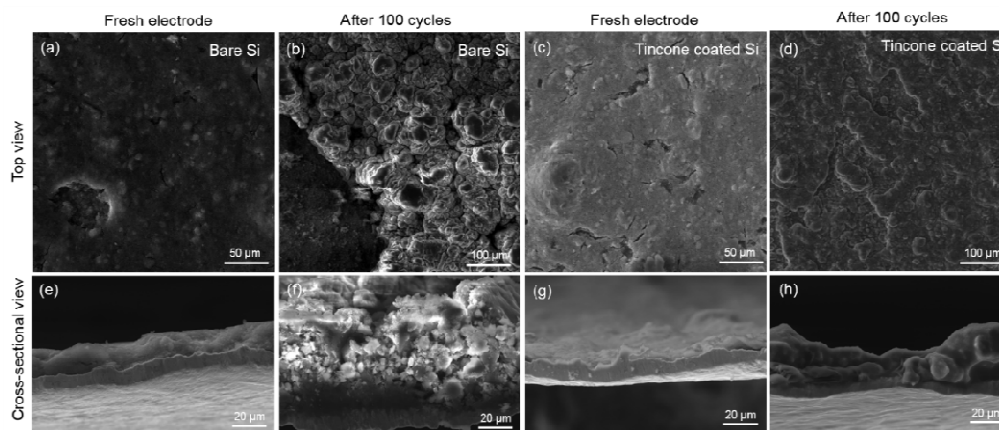
Figure 5-13: The top-view (a-d) and crosss-section (e-h) SEM images of bare Si and Si-tincone-30 before and after 100 cycles.

To have a deep understanding of the working mechanism of Si-tincone electrode, the electrochemical performance of the Si-tincone electrodes was explored by electrochemical impedance spectroscopy (EIS). The EIS curves consist of a semicircle in the high-frequency region, corresponding to the SEI resistance (R_f) and/or charge transfer resistance (R_{CT}), and an inclined line in the low-frequency region to Warburg impedance related to the diffusion of Li

ions into the electrode. Figure 5-14a shows Nyquist plots for Si-tincone electrodes before cycling. The bare Si electrode shows the lowest R_{CT}, suggesting that the tincone is not conducive to transferring ions on the electrode surface. However, after 100 cycles as shown in Figure 5-14b, the bare Si electrode shows the largest R_{CT} and R_f. The charge transfer resistance of tincone coated Si after cycling is much smaller than the uncoated sample and the electrode before cycling. This is due to that, after cycling, the tincone coating was activated by Li-ion and become an artificial SEI layer with Li-ion conductivity. The Si-tincone-30 shows the best lithiation kinetics, which might be due to the proper thickness of tincone coatings acts as both protective battier and Li-ion diffusion pathways.
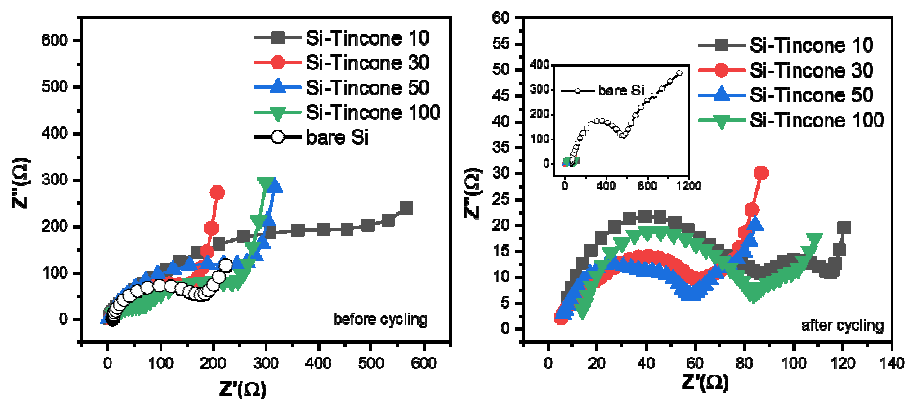
Figure 5-14: EIS test for the Si electrode with and without tincone coating before and after cycling.

The chemical compositions and chemical states of the tincone coating were investigated via XPS after cycling, as shown in Figure 5-15. In the C1s peaks fitting, the binding energies were approximately same between tincone-Si and bare Si electrodes (Figure 5-15a and b). However, in the O1s peak, the bare Si electrode shows additional peak at 533.8 eV (Figure 5-15d) corresponding for C-O-C of organic electrolytes, indicating that there are more absorption and side reaction between bare Si and electrolytes without the protection of Tincone coating.

Furthermore, the Sn 3d peaks in Figure 5-15e shows two distinctive binding energies, at 386.5 eV for Li_xSnO_y and at 487.1 eV for SnF_x. The Li_xSnO_y on the Si surface can be a good conductor, which offers superior conducting properties than the bare Si electrode [154].
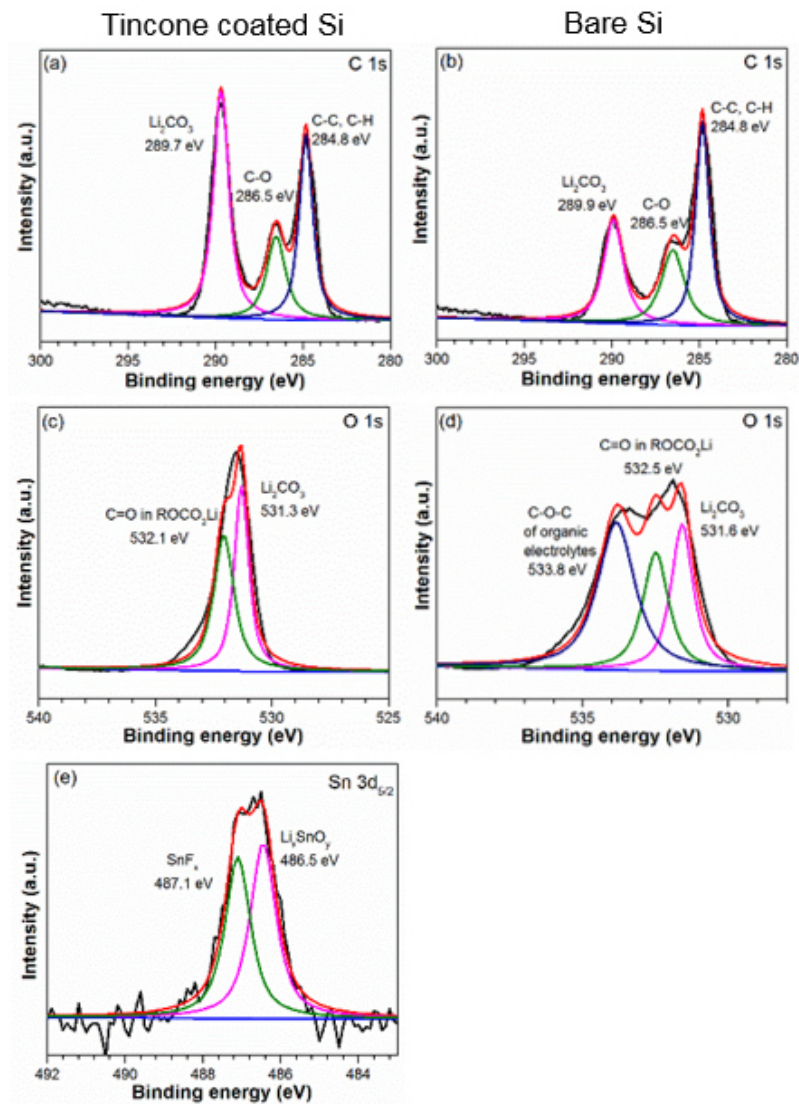
Figure 5-15: XPS analysis of Si electrode with and without tincone coating after cycling.

In conclusion, the tincone with the MLD method was successfully coated on the Si electrode. Tincone film could effectively work as a protecting material in LIBs because of its

flexibility and electrochemical activity. The Si-tincone-30 showed the best performance by delivering the capacity retention of 70% after 110 cycles due to its optimized thickness of tincone coating. Furthermore, the tincone layer worked as an artificial SEI film that could suppress the Si swelling problem by enhancing the kinetics of cell reaction.

Chapter 6: Conclusion, contribution, and perspective

6.1 Conclusion

This thesis mainly focused on developing novel coating materials and processes for surface engineering on Si electrodes in lithium-ion batteries and deepening a fundamental understanding of the correlation among surface coating, electrochemical properties, and working mechanisms in Si anodes. The overall electrochemical performance of Si-based anodes, such as specific capacity, cycling stability, and Coulombic efficiency, was improved by using various surface coating materials (Al_2O_3, AlO_xN_y, and tincone). Moreover, the electrochemical properties of Si-based anodes were dependent on the type and thickness of coating materials. The main reasons for the performance enhancement were due to the suppressed side reactions between Si electrode and electrolyte, stabilized solid electrolyte interphase, and reduced resistances at interfaces by artificial surface modifications. The conclusions specific to each work are summarized below.

In the first work, a low-cost and straightforward sol-gel technique was used to modify Si-based electrodes with Al_2O_3 coating. The findings showed that the Al_2O_3 coating significantly enhanced the cycle stability and Coulombic efficiency of the G/Si anode in Li-ion batteries. After 100 cycles, the capacity retention of the Al_2O_3-coated G/Si anode was 76.4 % at 25 ^{o}C, whereas the uncoated one was only 56.4 %. The Al_2O_3 coating as an artificial SEI layer could efficiently prevent the consumption of electrolytes during cycling. The sol-gel synthetic method for Al_2O_3 coating is low-cost and straightforward to scale up, making it a promise for practical commercial applications.

In the second study, Si electrodes were coated with AlO_xN_y thin films by advanced surface engineering technique, PEALD, for the first time and applied as the anode for lithium-ion batteries. The electrochemical performance was enhanced due to the electrochemical properties

of AlO_xN_y film. At 140 cycles, The AlO_xN_y-coated Si electrode retained 72.3 % of its capacity, compared to 13.3 % for the bare Si electrode, suggesting that the AlO_xN_y-coated Si electrode has promising cycle stability. The AlO_xN_y became an ion-conducting SEI layer and acted as a Li-ion diffusion pathway, improving ion transfers while preserving the electrode's mechanical and structural integrity, as well as the coated Si electrode's capacity and kinetics. It also reduced side reactions at the electrode-electrolyte interface and inhibited silicon volume change. This work explored the development and utilization of aluminum oxynitride, a representative example of metal oxynitride, as surface coating materials in lithium-ion batteries.

In the third step, tincone was successfully coated by another advanced coating method, MLD, on the Si electrode. In spite of the flexibility advantage of tincone film, it also found that tincone has the Li-ion storage ability, which makes it a multifunctional protective film for Si electrodes in LIBs. The Si-tincone-30 demonstrated the most outstanding performance, retaining 70 % of its capacity after 110 cycles. Tincone coating acts as both protective battier and Li-ion diffusion pathway, suppressing the structural degradation of the silicon and enhanced the battery performance.

6.2 Contribution

Throughout my Ph.D. study, I made contributions to the process and material development of novel surface coatings by various methods (sol-gel, PEALD, and MLD), and the application of these surface coating layers to stabilize electrode-electrolyte interfaces in Si anodes to enable high-performance lithium-ion batteries for electric vehicle applications. These contributions will help the battery community to advance battery technology development for clean transportation.

- A facile and low-cost sol-gel process was developed to apply Al_2O_3 coating on G/Si anode and improve its performance at both room and high temperatures. Even

though the sol-gel process had been used commonly to protect cathode materials, it is the first time to use and demonstrate its application in enhancing the properties of G/Si anode in LIBs. The sol-gel process is featured with low cost and good scalability and thus could be applied for large-scale production of surface coatings on Si-based anodes.

- The surface chemistry and deposition process of aluminum oxynitride (AlO_xN_y) was designed by PEALD. Moreover, the aluminum oxynitride was adopted as the coating material on Si anodes for LIBs for the first time. The main finding was that AlO_xN_y coating transformed to an SEI layer containing Li-ion conductors, which is an advantage of artificial coating films. This work not only opens the door to use metal oxynitride as surface coatings in LIBs but contributes to the surface chemistry of metal oxynitride by PEALD.

- The MLD deposition process of tincone was established, and for the first time, reported the electrochemical activity of tincone for Li-ion storage. Moreover, The tincone was used as a flexible, electrochemically active, and hybrid coating on Si anodes to address its significant volume change and unstable SEI problems. This work contributes to the development of organic-inorganic thin films by MLD, their application as surface coating in LIBs, and the design of multifunctional coating materials at the molecular level.

6.3 Perspective

Despite the advancement in the design and application of surface coatings for Si anodes, this Ph.D. research has some limitations due to some constraints on research or methodology. Therefore, the following directions are suggested for future research to advance Si anodes for

practical appliations further.

(1) More in-depth mechanistic study on the functions of surface coatings on Si through advanced *in-situ* or *ex-situ* characterization techniques

This Ph.D. research found that surface coating at the nanoscale level (2-15 nm) was critical for stabilizing Si anodes without block Li-ion and electron transport through the artificial SEI layers. The nature of these nanoscale coatings makes it challenging to characterize the structural change of the coating layers on the Si electrode after battery cycling. In particular, it would be interesting to investigate the evolution of the nanoscale coating layers during the battery cycling using *in-situ* HRTEM [151]. More in-depth knowledge on the structural change would be beneficial for understanding the working mechanism of surface coating on Si anode and guiding the design of better coatings in the future.

(2) Assessment of surface-coated Si anode in pouch cells

This research used half cells, *i.e.*, Si as the working electrode and Li metal as the counter electrode, to evaluate the influence of various surface coatings on the electrochemical properties of Si anode. Although the half cells revealed important information of the Si anode itself, they cannot simulate the working conditions of Si anode in real applications, such as in pouch cells. For example, the Si swelling issue was only investigated in this work by measuring the electrode thickness before and after battery cycling in coin cells. This problem could be more evident and better quantified in pouch cells due to accumulated thickness changes from several electrodes.

(3) Exploration of Si anodes in all-solid-state lithium-ion batteries (ASSLIBs)

The main problems in current Si anodes are caused by the unstable electrode-electrolyte interface, a solid-liquid interface in current liquid-electrolyte-based LIBs. The continuous decomposition of liquid electrolytes on the interface leads to repeated formation and breakdown

of the SEI layers. It would be fundamentally interesting to explore the Si anodes in ASSLIBs, in which the electrode-electrolyte interface is a solid-solid interface to avoid electrode interactions with any liquid electrolyte. Moreover, ASSLIBs provide several advantages over conventional liquid-based LIBs, such as higher energy density, faster charge/discharge rate, and better safety. They have lower potential safety risks, such as thermal runaway and explosion, due to the non-flammable nature of solid inorganic electrolytes employed. The complete preliminary research work was done to use the spark plasma sintering (SPS) method to sinter highly dense and ion-conducting lithium aluminum germanium phosphate (LAGP) solid electrolyte pellets (Appendix A). Future work could focus on the fabrication of LAGP, Si, and carbon composite pellets by SPS and investigate its applications as the anode in ASSLIBs.

References

[1] M.S. Ziegler and J.E. Trancik, *Energy & Environmental Science,* **14**, 1635 (2021).

[2] L. Lu, H. Yang and J. Burnett, *Renewable Energy,* **27**, 1 (2002).

[3] T.T. Chow, *Applied Energy,* **87**, 365 (2010).

[4] J. Xu, S. Dou, H. Liu and L. Dai, *Nano Energy,* **2**, 439 (2013).

[5] S. Zhang, *npj Computational Materials,* **3**, 1 (2017).

[6] C. Zhu, K. Han, D. Geng, H. Ye and X. Meng, *Electrochim. Acta,* **251**, 710 (2017).

[7] M. Armand and J.-M. Tarascon, *Nat.,* **451**, 652 (2008).

[8] P. Roy and S.K. Srivastava, *Journal of Materials Chemistry A,* **3**, 2454 (2015).

[9] B. Scrosati and J. Garche, *Journal of Power Sources,* **195**, 2419 (2010).

[10] J.-M. Tarascon and M. Armand, *Materials for sustainable energy: a collection of peer-reviewed research and review articles from Nature Publishing Group*, 171 (2011).

[11] W.-J. Zhang, *Journal of Power Sources,* **196**, 13 (2011).

[12] J.-Y. Li, Q. Xu, G. Li, Y.-X. Yin, L.-J. Wan and Y.-G. Guo, *Materials Chemistry Frontiers,* **1**, 1691 (2017).

[13] J.R. Szczech and S. Jin, *Energy & Environmental Science,* **4**, 56 (2011).

[14] H. Wu and Y. Cui, *Nano today,* **7**, 414 (2012).

[15] X. Zuo, J. Zhu, P. Müller-Buschbaum and Y.-J. Cheng, *Nano Energy,* **31**, 113 (2017).

[16] M. Obrovac and L. Christensen, *Electrochemical and solid state letters,* **7**, A93 (2004).

[17] M.W. Verbrugge, D.R. Baker, X. Xiao, Q. Zhang and Y.-T. Cheng, *The Journal of Physical Chemistry C,* **119**, 5341 (2015).

[18] H. Wu, G. Zheng, N. Liu, T.J. Carney, Y. Yang and Y. Cui, *Nano Lett.,* **12**, 904 (2012).

[19] F. Luo, B. Liu, J. Zheng, G. Chu, K. Zhong, H. Li, X. Huang and L. Chen, *J. Electrochem. Soc.,* **162**, A2509 (2015).

[20] J.W. Choi and D. Aurbach, *Nature Reviews Materials,* **1**, 1 (2016).

[21] E. Roduner, *Chem. Soc. Rev.,* **35**, 583 (2006).

[22] A.S. Arico, P. Bruce, B. Scrosati, J.-M. Tarascon and W. Van Schalkwijk, *Materials for sustainable energy: a collection of peer-reviewed research and review articles from Nature Publishing Group*, 148 (2011).

[23] L. Beaulieu, K. Eberman, R. Turner, L. Krause and J. Dahn, *Electrochemical and solid state letters,* **4**, A137 (2001).

[24] L. Beaulieu, T. Hatchard, A. Bonakdarpour, M. Fleischauer and J. Dahn, *J. Electrochem. Soc.,* **150**, A1457 (2003).

[25] W. Chen, Z. Fan, A. Dhanabalan, C. Chen and C. Wang, *J. Electrochem. Soc.,* **158**, A1055 (2011).

[26] Y. Yao, M.T. McDowell, I. Ryu, H. Wu, N. Liu, L. Hu, W.D. Nix and Y. Cui, *Nano Lett.,* **11**, 2949 (2011).

[27] D. Ma, Z. Cao and A. Hu, *Nano-Micro Letters,* **6**, 347 (2014).

[28] J. Liu and X. Sun, *Nanotechnology,* **26**, 024001 (2014).

[29] H. Wu, G. Chan, J.W. Choi, I. Ryu, Y. Yao, M.T. McDowell, S.W. Lee, A. Jackson, Y. Yang and L. Hu, *Nature nanotechnology,* **7**, 310 (2012).

[30] Y. Chen, L. Liu, J. Xiong, T. Yang, Y. Qin and C. Yan, *Adv. Funct. Mater.,* **25**, 6701 (2015).

[31] W.-R. Liu, J.-H. Wang, H.-C. Wu, D.-T. Shieh, M.-H. Yang and N.-L. Wu, *J. Electrochem. Soc.,* **152**, A1719 (2005).

[32] S.H. Ng, J. Wang, D. Wexler, K. Konstantinov, Z.P. Guo and H.K. Liu, *Angew. Chem. Int. Ed.,* **45**, 6896 (2006).

[33] Y.S. Hu, R. Demir-Cakan, M.M. Titirici, J.O. Müller, R. Schlögl, M. Antonietti and J. Maier, *Angew. Chem. Int. Ed.,* **47**, 1645 (2008).

[34] Z. Wen, J. Yang, B. Wang, K. Wang and Y. Liu, *Electrochem. Commun.,* **5**, 165 (2003).

[35] L. Zhang, R. Rajagopalan, H. Guo, X. Hu, S. Dou and H. Liu, *Adv. Funct. Mater.,* **26**, 440 (2016).

[36] P. Gu, R. Cai, Y. Zhou and Z. Shao, *Electrochim. Acta,* **55**, 3876 (2010).

[37] Y. Xu, G. Yin, Y. Ma, P. Zuo and X. Cheng, *Journal of Materials Chemistry,* **20**, 3216 (2010).

[38] W. Li, Y. Tang, W. Kang, Z. Zhang, X. Yang, Y. Zhu, W. Zhang and C.S. Lee, *Small,* **11**, 1345 (2015).

[39] L. Wang, B. Gao, C. Peng, X. Peng, J. Fu, P.K. Chu and K. Huo, *Nanoscale,* **7**, 13840 (2015).

[40] G. Hou, B. Cheng, Y. Cao, M. Yao, B. Li, C. Zhang, Q. Weng, X. Wang, Y. Bando and D. Golberg, *Nano Energy,* **24**, 111 (2016).

[41] J.-I. Lee, Y. Ko, M. Shin, H.-K. Song, N.-S. Choi, M.G. Kim and S. Park, *Energy & Environmental Science,* **8**, 2075 (2015).

[42] X. Meng, X.Q. Yang and X. Sun, *Advanced Materials,* **24**, 3589 (2012).

[43] P. Sundberg and M. Karppinen, *Beilstein journal of nanotechnology,* **5**, 1104 (2014).

[44] A. Paranjpe, S. Gopinath, T. Omstead and R. Bubber, *J. Electrochem. Soc.,* **148**, G465 (2001).

[45] N. Pinna and M. Knez, Atomic layer deposition of nanostructured materials, Wiley Online Library, 2012.

[46] O.-K. Kwon, S.-H. Kwon, H.-S. Park and S.-W. Kang, *J. Electrochem. Soc.,* **151**, C753 (2004).

[47] J. Musschoot, D. Deduytsche, H. Poelman, J. Haemers, R. Van Meirhaeghe, S. Van den Berghe and C. Detavernier, *J. Electrochem. Soc.,* **156**, P122 (2009).

[48] A. Ali, H. Madan, A. Kirk, D. Zhao, D. Mourey, M.K. Hudait, R. Wallace, T. Jackson, B. Bennett and J. Boos, *Appl. Phys. Lett.,* **97**, 143502 (2010).

[49] S. Sioncke, A. Delabie, G. Brammertz, T. Conard, A. Franquet, M. Caymax, A. Urbanzcyk, M. Heyns, M. Meuris and J. Van Hemmen, *J. Electrochem. Soc.,* **156**, H255 (2009).

[50] E.M. Lotfabad, P. Kalisvaart, A. Kohandehghan, K. Cui, M. Kupsta, B. Farbod and D. Mitlin, *Journal of Materials Chemistry A,* **2**, 2504 (2014).

[51] D.M. Piper, J.J. Travis, M. Young, S.B. Son, S.C. Kim, K.H. Oh, S.M. George, C. Ban and S.H. Lee, *Advanced Materials,* **26**, 1596 (2014).

[52] D.M. Piper, Y. Lee, S.-B. Son, T. Evans, F. Lin, D. Nordlund, X. Xiao, S.M. George, S.-H. Lee and C. Ban, *Nano Energy,* **22**, 202 (2016).

[53] H.C.M. Knoops, M.E. Donders, M.C.M.V.D. Sanden, P.H.L. Notten and W.M.M. Kessels, *Journal of Vacuum Science & Technology A Vacuum Surfaces & Films,* **30**, 010801 (2012).

[54] S.M. George, *Chemical Reviews,* **110**, 111 (2010).

[55] V. Miikkulainen, M. Leskelä, M. Ritala and R.L. Puurunen, *Journal of Applied Physics,* **113**, 430 (2013).

[56] P.W. Hawkes and J.C. Spence, Science of microscopy, Springer, 2007.

[57] V.K. Pecharsky and P.Y. Zavalij, *Fundamentals of powder diffraction and structural characterization of materials*, 99 (2003).

[58] G. Greczynski and L. Hultman, *Progress in Materials Science,* **107**, 100591 (2020).

[59] J.-K. Park, Principles and applications of lithium secondary batteries, John Wiley & Sons, 2012.

[60] N. Ogihara, Y. Itou, T. Sasaki and Y. Takeuchi, *The Journal of Physical Chemistry C,* **119**, 4612 (2015).

[61] J.B. Goodenough and Y. Kim, *Chem. Mater.,* **22**, 587 (2010).

[62] A. Kwade, W. Haselrieder, R. Leithoff, A. Modlinger, F. Dietrich and K. Droeder, *Nature Energy,* **3**, 290 (2018).

[63] S.A. Freunberger, *Nature Energy,* **2**, 1 (2017).

[64] T. Xiong, H. Su, F. Yang, Q. Tan, P. Appadurai, A. Afuwape, K. Guo, Y. Huang, Z. Wang and M.-S.J.T. Balogun, *Materials Today Energy,* **17**, 100461 (2020).

[65] Y. Huang, H. Yang, T. Xiong, D. Adekoya, W. Qiu, Z. Wang, S. Zhang and M.-S. Balogun, *Energy Storage Materials,* **25**, 41 (2020).

[66] R. Chandrasekaran, A. Magasinski, G. Yushin and T.F. Fuller, *J. Electrochem. Soc.,* **157**, A1139 (2010).

[67] N. Nitta, F. Wu, J.T. Lee and G. Yushin, *Mater. Today,* **18**, 252 (2015).

[68] M.T. McDowell, S.W. Lee, J.T. Harris, B.A. Korgel, C. Wang, W.D. Nix and Y. Cui, *Nano Lett.,* **13**, 758 (2013).

[69] S. Chae, M. Ko, K. Kim, K. Ahn and J. Cho, *Joule,* **1**, 47 (2017).

[70] S. Kalnaus, K. Rhodes and C. Daniel, *Journal of Power Sources,* **196**, 8116 (2011).

[71] R. Kumar, A. Tokranov, B.W. Sheldon, X. Xiao, Z. Huang, C. Li and T. Mueller, *ACS Energy Letters,* **1**, 689 (2016).

[72] Y. Li, S. Zhu, Q. Liu, J. Gu, Z. Guo, Z. Chen, C. Feng, D. Zhang and W.-J. Moon, *Journal of Materials Chemistry,* **22**, 2766 (2012).

[73] W. Luo, X. Chen, Y. Xia, M. Chen, L. Wang, Q. Wang, W. Li and J. Yang, *Advanced Energy Materials,* **7**, 1701083 (2017).

[74] I. Belharouak, J. Nanda, E. Self, W. Hawley, D. Wood III, Z. Du, J. Li and R.L. Graves, Operation, Manufacturing, and Supply Chain of Lithium-ion Batteries for Electric Vehicles, in, Oak Ridge National Lab.(ORNL), Oak Ridge, TN (United States), 2020.

[75] J.-B. Park, J.-S. Ham, M.-S. Shin, H.-K. Park, Y.-J. Lee and S.-M. Lee, *Journal of Power Sources,* **299**, 537 (2015).

[76] M. Winter, J.O. Besenhard, M.E. Spahr and P. Novak, *Advanced Materials,* **10**, 725 (1998).

[77] R. Petibon, V. Chevrier, C. Aiken, D. Hall, S. Hyatt, R. Shunmugasundaram and J. Dahn, *J. Electrochem. Soc.,* **163**, A1146 (2016).

[78] S.Y. Kim, J. Lee, B.-H. Kim, Y.-J. Kim, K.S. Yang and M.-S. Park, *ACS applied materials & interfaces,* **8**, 12109 (2016).

[79] S.J. An, J. Li, C. Daniel, H.M. Meyer III, S.E. Trask, B.J. Polzin and D.L. Wood III, *ACS applied materials & interfaces,* **9**, 18799 (2017).

[80] M. Wetjen, D. Pritzl, R. Jung, S. Solchenbach, R. Ghadimi and H.A. Gasteiger, *J. Electrochem. Soc.,* **164**, A2840 (2017).

[81] W.M. Dose, V.A. Maroni, M.J. Piernas-Muñoz, S.E. Trask, I. Bloom and C.S. Johnson, *J. Electrochem. Soc.,* **165**, A2389 (2018).

[82] M. Klett, J.A. Gilbert, K.Z. Pupek, S.E. Trask and D.P. Abraham, *J. Electrochem. Soc.,* **164**, A6095 (2016).

[83] S. Hao and C. Wolverton, *The Journal of Physical Chemistry C,* **117**, 8009 (2013).

[84] S.C. Jung and Y.-K. Han, *The journal of physical chemistry letters,* **4**, 2681 (2013).

[85] X. Xiao, P. Lu and D. Ahn, *Advanced Materials,* **23**, 3911 (2011).

[86] Y. He, X. Yu, Y. Wang, H. Li and X. Huang, *Advanced Materials,* **23**, 4938 (2011).

[87] H.T. Nguyen, M.R. Zamfir, L.D. Duong, Y.H. Lee, P. Bondavalli and D. Pribat, *Journal of Materials Chemistry,* **22**, 24618 (2012).

[88] K. Xu, Z. Zhang, W. Su, Z. Wei, G. Zhong, C. Wang and X. Huang, *Functional Materials Letters,* **10**, 1650073 (2017).

[89] K. Kim, M.-S. Kim, H. Choi, K.-S. Min, K.-D. Kim and J.-H. Kim, *Electronic Materials Letters,* **13**, 152 (2017).

[90] D. Lin, Z. Lu, P.-C. Hsu, H.R. Lee, N. Liu, J. Zhao, H. Wang, C. Liu and Y. Cui, *Energy & Environmental Science,* **8**, 2371 (2015).

[91] S. Jeong, X. Li, J. Zheng, P. Yan, R. Cao, H.J. Jung, C. Wang, J. Liu and J.-G. Zhang, *Journal of Power Sources,* **329**, 323 (2016).

[92] Y.N. Jo, Y. Kim, J.S. Kim, J.H. Song, K.J. Kim, C.Y. Kwag, D.J. Lee, C.W. Park and Y.J. Kim, *Journal of Power Sources,* **195**, 6031 (2010).

[93] S. Ma, M. Jiang, P. Tao, C. Song, J. Wu, J. Wang, T. Deng and W. Shang, *Progress in Natural Science: Materials International,* **28**, 653 (2018).

[94] H. Park, S. Choi, S.-J. Lee, Y.-G. Cho, G. Hwang, H.-K. Song, N.-S. Choi and S. Park, *Nano Energy,* **26**, 192 (2016).

[95] J.R. Owen, *Chem. Soc. Rev.,* **26**, 259 (1997).

[96] J.H. Ryu, J.W. Kim, Y.-E. Sung and S.M. Oh, *Electrochemical and solid state letters,* **7**, A306 (2004).

[97] J.W. Wang, Y. He, F. Fan, X.H. Liu, S. Xia, Y. Liu, C.T. Harris, H. Li, J.Y. Huang and S.X. Mao, *Nano Lett.,* **13**, 709 (2013).

[98] M. Gu, Y. Li, X. Li, S. Hu, X. Zhang, W. Xu, S. Thevuthasan, D.R. Baer, J.-G. Zhang and J. Liu, *ACS nano,* **6**, 8439 (2012).

[99] X.H. Liu, L. Zhong, S. Huang, S.X. Mao, T. Zhu and J.Y. Huang, *ACS nano,* **6**, 1522 (2012).

[100] S.B. Son, S.C. Kim, C.S. Kang, T.A. Yersak, Y.C. Kim, C.G. Lee, S.H. Moon, J.S. Cho, J.T. Moon and K.H. Oh, *Advanced Energy Materials,* **2**, 1226 (2012).

[101] D.M. Piper, T.A. Yersak and S.-H. Lee, *J. Electrochem. Soc.,* **160**, A77 (2012).

[102] E.M. Lotfabad, P. Kalisvaart, A. Kohandehghan, K. Cui, M. Kupsta, B. Farbod and D. Mitlin, *J. Mater. Chem. A,* **2**, 2504 (2014).

[103] S. Yang, H. Chen, J. Li, H. Guo, X. Mao, R. Tian, J. Zhang and S. Wang, *J. Am. Ceram. Soc.,* (2021).

[104] J.W. McCauley, P. Patel, M. Chen, G. Gilde, E. Strassburger, B. Paliwal, K. Ramesh and D.P. Dandekar, *Journal of the European Ceramic Society,* **29**, 223 (2009).

[105] J.C.S. Fernandes and M.G.S. Ferreira, *Surface and Coatings Technology,* **56**, 75 (1992).

[106] J.C.S. Fernandes, R. Picciochi, M. Da Cunha Belo, T. Moura e Silva, M.G.S. Ferreira and I.T.E. Fonseca, *Electrochimica Acta,* **49**, 4701 (2004).

[107] J. Borges, C. Fonseca, N.P. Barradas, E. Alves, T. Girardeau, F. Paumier, F. Vaz and L. Marques, *Electrochimica Acta,* **106**, 23 (2013).

[108] X. Han, Z. Zhang, R. You, G. Zheng, C. Li, S. Chen and Y. Yang, *Journal of Materials Chemistry A,* **6**, 7449 (2018).

[109] K.J. Chen and S. Huang, *Semicond. Sci. Technol.,* **28**, 074015 (2013).

[110] A.P. Perros, H. Hakola, T. Sajavaara, T. Huhtio and H. Lipsanen, *J. Phys. D: Appl. Phys.,* **46**, 505502 (2013).

[111] Y. Zhang, Y. Wu, H. Ding, Y. Yan, Z. Zhou, Y. Ding and N. Liu, *Nano Energy,* **53**, 666 (2018).

[112] K. Feng, W. Ahn, G. Lui, H.W. Park, A.G. Kashkooli, G. Jiang, X. Wang, X. Xiao and Z. Chen, *Nano Energy,* **19**, 187 (2016).

[113] M. Smith, L. Scudiero, J. Espinal, J.-S. McEwen and M. Garcia-Perez, *Carbon,* **110**, 155 (2016).

[114] K. Xu, *Chemical Reviews,* **104**, 4303 (2004).

[115] C.-H. Chang, S.-H. Chung, P. Han and A. Manthiram, *Materials Horizons,* **4**, 908 (2017).

[116] T. Lapp, S. Skaarup and A. Hooper, *Solid State Ionics,* **11**, 97 (1983).

[117] S.C. Jung and Y.-K. Han, *The Journal of Physical Chemistry Letters,* **4**, 2681 (2013).

[118] T. Kusunose and T. Sekino, *Ceramics International,* **42**, 13183 (2016).

[119] Z. Yan, X.-Y. Niu, X.-Q. Du, Q.-C. Wang, X.-J. Wu and Y.-N. Zhou, *Rare Metals,* **37**, 625 (2018).

[120] J.F. Oudenhoven, L. Baggetto and P.H. Notten, *Advanced Energy Materials,* **1**, 10 (2011).

[121] J.I. Hur, L.C. Smith and B. Dunn, *Joule,* **2**, 1187 (2018).

[122] C. Liu, E.I. Gillette, X. Chen, A.J. Pearse, A.C. Kozen, M.A. Schroeder, K.E. Gregorczyk, S.B. Lee and G.W. Rubloff, *Nature nanotechnology,* **9**, 1031 (2014).

[123] J.W. Long, B. Dunn, D.R. Rolison and H.S. White, *Chem. Rev.,* **104**, 4463 (2004).

[124] V. Miikkulainen, M. Leskelä, M. Ritala and R.L. Puurunen, *J. Appl. Phys.,* **113**, 2 (2013).

[125] W. Lu, L. Liang, X. Sun, X. Sun, C. Wu, L. Hou, J. Sun and C. Yuan, *Nanomaterials,* **7**, 325 (2017).

[126] Y. Zhao, K. Zheng and X. Sun, *Joule,* **2**, 2583 (2018).

[127] X. Han, Y. Gong, K.K. Fu, X. He, G.T. Hitz, J. Dai, A. Pearse, B. Liu, H. Wang and G. Rubloff, *Nature materials,* **16**, 572 (2017).

[128] J. Liu, B. Wang, Q. Sun, R. Li, T.K. Sham and X. Sun, *Advanced Materials Interfaces,* **3**, 1600468 (2016).

[129] A. Pearse, T. Schmitt, E. Sahadeo, D.M. Stewart, A. Kozen, K. Gerasopoulos, A.A. Talin, S.B. Lee, G.W. Rubloff and K.E. Gregorczyk, *ACS nano,* **12**, 4286 (2018).

[130] A.J. Pearse, T.E. Schmitt, E.J. Fuller, F. El-Gabaly, C.-F. Lin, K. Gerasopoulos, A.C. Kozen, A.A. Talin, G. Rubloff and K.E. Gregorczyk, *Chem. Mater.,* **29**, 3740 (2017).

[131] B.H. Lee, B. Yoon, A.I. Abdulagatov, R.A. Hall and S.M. George, *Adv. Funct. Mater.,* **23**, 532 (2013).

[132] X. Meng, *Journal of Materials Chemistry A,* **5**, 18326 (2017).

[133] C. Ban and S.M. George, *Advanced Materials Interfaces,* **3**, 1600762 (2016).

[134] M. Nisula and M. Karppinen, *Nano Lett.,* **16**, 1276 (2016).

[135] K. Van de Kerckhove, F. Mattelaer, D. Deduytsche, P.M. Vereecken, J. Dendooven and C. Detavernier, *Dalton Transactions,* **45**, 1176 (2016).

[136] K. Van de Kerckhove, F. Mattelaer, J. Dendooven and C. Detavernier, *Dalton Transactions,* **46**, 4542 (2017).

[137] E. Kazyak, K.-H. Chen, K.N. Wood, A.L. Davis, T. Thompson, A.R. Bielinski, A.J. Sanchez, X. Wang, C. Wang and J. Sakamoto, *Chem. Mater.,* **29**, 3785 (2017).

[138] J. Liu, M.N. Banis, Q. Sun, A. Lushington, R. Li, T.K. Sham and X. Sun, *Advanced Materials,* **26**, 6472 (2014).

[139] M. Arjmand, K. Chizari, B. Krause, P. Pötschke and U. Sundararaj, *Carbon,* **98**, 358 (2016).

[140] K. Van de Kerckhove, J. Dendooven and C. Detavernier, *Journal of Vacuum Science & Technology A: Vacuum, Surfaces, and Films,* **36**, 051506 (2018).

[141] Z. Liu, K. Handa, K. Kaibuchi, Y. Tanaka and J. Kawai, *J. Electron. Spectrosc. Relat. Phenom.,* **135**, 155 (2004).

[142] D. Wang, X. Li, J. Yang, J. Wang, D. Geng, R. Li, M. Cai, T.-K. Sham and X. Sun, *PCCP,* **15**, 3535 (2013).

[143] A. Olivos Suarez, V. Lyaskovskyy, J. Reek, J. van der Vlugt and B. de Bruin, *Angew. Chem. Int. Ed.,* **52**, 12510 (2013).

[144] D. Tonti, A. Sorrentino, M. Olivares-Marín and E. Pereiro, (2017).

[145] J.W. DuMont, *Graduate Thesis, University of Colorado Boulder,* (2016).

[146] Q. Tian, Y. Tian, Z. Zhang, L. Yang and S.-i. Hirano, *Journal of Power Sources,* **269**, 479 (2014).

[147] X. Zhang, X. Huang, X. Zhang, L. Xia, B. Zhong, T. Zhang and G. Wen, *Electrochim. Acta,* **222**, 518 (2016).

[148] S. Zhu, J. Liu and J. Sun, *Applied Surface Science,* **484**, 600 (2019).

[149] J. Liang, W. Wei, D. Zhong, Q. Yang, L. Li and L. Guo, *ACS applied materials &*

interfaces, **4**, 454 (2012).

[150] M. Zhao, Q. Zhao, J. Qiu, H. Xue and H. Pang, *RSC Advances,* **6**, 95449 (2016).

[151] Y. He, D.M. Piper, M. Gu, J.J. Travis, S.M. George, S.-H. Lee, A. Genc, L. Pullan, J. Liu and S.X. Mao, *ACS nano,* **8**, 11816 (2014).

[152] L. Luo, H. Yang, P. Yan, J.J. Travis, Y. Lee, N. Liu, D. Molina Piper, S.-H. Lee, P. Zhao and S.M. George, *ACS nano,* **9**, 5559 (2015).

[153] G. Ferraresi, C. Villevieille, I. Czekaj, M. Horisberger, P. Novák and M. El Kazzi, *ACS applied materials & interfaces,* **10**, 8712 (2018).

[154] D. Bauer, T. Bunjaku, A. Pedersen and M. Luisier, *J. Appl. Phys.,* **122**, 055105 (2017).

[155] C. Guan and J. Wang, *Advanced science,* **3**, 1500405 (2016).

[156] S. Kim, W. Cho, X. Zhang, Y. Oshima and J.W. Choi, *Nature communications,* **7**, 13598 (2016).

[157] Y. Liu, C. Li, B. Li, H. Song, Z. Cheng, M. Chen, P. He and H. Zhou, *Advanced Energy Materials,* **8** (2018).

[158] S. Abada, G. Marlair, A. Lecocq, M. Petit, V. Sauvant-Moynot and F. Huet, *Journal of Power Sources,* **306**, 178 (2016).

[159] Z. Deng, Y. Mo and S.P. Ong, *NPG Asia Materials,* **8**, e254 (2016).

[160] M. Weiss, D.A. Weber, A. Senyshyn, J. Janek and W.G. Zeier, *ACS applied materials & interfaces,* **10**, 10935 (2018).

[161] C. Sun, X. Huang, J. Jin, Y. Lu, Q. Wang, J. Yang and Z. Wen, *Journal of Power Sources,* **377**, 36 (2018).

[162] Y.-C. Jung, M.-S. Park, C.-H. Doh and D.-W. Kim, *Electrochimica Acta,* **218**, 271 (2016).

[163] E. Kazyak, K.-H. Chen, K.N. Wood, A.L. Davis, T. Thompson, A.R. Bielinski, A.J. Sanchez, X. Wang, C. Wang, J. Sakamoto and N.P. Dasgupta, *Chemistry of Materials,* **29**, 3785 (2017).

[164] Z. Dong, C. Xu, Y. Wu, W. Tang, S. Song, J. Yao, Z. Huang, Z. Wen, L. Lu and N. Hu, *Nanomaterials,* **9** (2019).

[165] H. Nguyen, S. Hy, E. Wu, Z. Deng, M. Samiee, T. Yersak, J. Luo, S.P. Ong and Y.S. Meng, *Journal of The Electrochemical Society,* **163**, A2165 (2016).

[166] E.E. Jay, M.J.D. Rushton, A. Chroneos, R.W. Grimes and J.A. Kilner, *Physical Chemistry Chemical Physics,* **17**, 178 (2015).

[167] K.-B. Kim, N.A. Dunlap, S.S. Han, J.J. Jeong, S.C. Kim, K.H. Oh and S.-H. Lee, *Journal of The Electrochemical Society,* **165**, A1903 (2018).

[168] A. Unemoto, K. Yoshida, T. Ikeshoji and S.-i. Orimo, *Materials Transactions,* **57**, 1639 (2016).

[169] F. Kaneko, S. Wada, M. Nakayama, M. Wakihara, J. Koki and S. Kuroki, *Advanced Functional Materials,* **19**, 918 (2009).

[170] Y. Masuda, M. Nakayama and M. Wakihara, *Solid State Ionics,* **178**, 981 (2007).

[171] Z. Lin, Z. Liu, W. Fu, N.J. Dudney and C. Liang, *Angewandte Chemie,* **52**, 7460 (2013).

[172] T. Asano, A. Sakai, S. Ouchi, M. Sakaida, A. Miyazaki and S. Hasegawa, *Advanced Materials,* **30** (2018).

[173] H.S. Jadhav, R.S. Kalubarme, A.H. Jadhav and J.G. Seo, *Electrochimica Acta,* **199**, 126 (2016).

[174] U. Ulissi, M. Agostini, S. Ito, Y. Aihara and J. Hassoun, *Solid State Ionics,* **296**, 13 (2016).

[175] M. Nagao, Y. Imade, H. Narisawa, T. Kobayashi, R. Watanabe, T. Yokoi, T. Tatsumi and R. Kanno, *Journal of Power Sources,* **222**, 237 (2013).

[176] T. Kobayashi, A. Yamada and R. Kanno, *Electrochimica Acta,* **53**, 5045 (2008).

[177] T. Kobayashi, Y. Imade, D. Shishihara, K. Homma, M. Nagao, R. Watanabe, T. Yokoi, A. Yamada, R. Kanno and T. Tatsumi, *Journal of Power Sources,* **182**, 621 (2008).

[178] N. Kuganathan, L.H. Tsoukalas and A. Chroneos, *Solid State Ionics,* **335**, 61 (2019).

[179] R. Yu, Q.-X. Du, B.-K. Zou, Z.-Y. Wen and C.-H. Chen, *Journal of Power Sources,* **306**, 623 (2016).

[180] F. Lalere, J.B. Leriche, M. Courty, S. Boulineau, V. Viallet, C. Masquelier and V. Seznec, *Journal of Power Sources,* **247**, 975 (2014).

[181] Y. Noguchi, E. Kobayashi, L.S. Plashnitsa, S. Okada and J.-i. Yamaki, *Electrochimica Acta,* **101**, 59 (2013).

[182] M.M. Mahmoud, Y. Cui, M. Rohde, C. Ziebert, G. Link and H.J. Seifert, *Materials,* **9** (2016).

[183] Y. Liu, C. Li, B. Li, H. Song, Z. Cheng, M. Chen, P. He and H. Zhou, *Advanced Energy Materials,* **8**, 1702374 (2018).

[184] X. Wei, J. Rechtin and E. Olevsky, *Metals,* **7**, 372 (2017).

[185] B. Yan, Y. Zhu, F. Pan, J. Liu and L. Lu, *Solid State Ionics,* **278**, 65 (2015).

[186] L.Z. Huang, Z.Y. Wen, J. Jin and Y. Liu, *Journal of Inorganic Materials,* **27**, 249 (2012).

[187] Q. Guo, Y. Han, H. Wang, S. Xiong, Y. Li, S. Liu and K. Xie, *ACS applied materials & interfaces,* **9**, 41837 (2017).

[188] K. Kerman, A. Luntz, V. Viswanathan, Y.-M. Chiang and Z. Chen, *Journal of The Electrochemical Society,* **164**, A1731 (2017).

[189] H. Zhu and J. Liu, *Journal of Power Sources,* **391**, 10 (2018).

[190] S. Duan, H. Jin, J. Yu, E.N. Esfahani, B. Yang, J. Liu, Y. Ren, Y. Chen, L. Lu, X. Tian, S. Hou and J. Li, *Nano Energy,* **51**, 19 (2018).

[191] E. Dumont-Botto, C. Bourbon, S. Patoux, P. Rozier and M. Dolle, *Journal of Power Sources,* **196**, 2274 (2011).

[192] A. Aboulaich, R. Bouchet, G. Delaizir, V. Seznec, L. Tortet, M. Morcrette, P. Rozier, J.-M. Tarascon, V. Viallet and M. Dollé, *Advanced Energy Materials,* **1**, 179 (2011).

[193] M. Pérez-Estébanez, J. Isasi-Marín, A. Rivera-Calzada, C. León and M. Nygren, *Journal of Alloys and Compounds,* **651**, 636 (2015).

[194] Y.-X. Gao, X.-P. Wang, Q.-X. Sun, Z. Zhuang and Q.-F. Fang, *Frontiers of Materials Science,* **6**, 216 (2012).

[195] R. Kali and A. Mukhopadhyay, *Journal of Power Sources,* **247**, 920 (2014).

[196] Y. Cui, M.M. Mahmoud, M. Rohde, C. Ziebert and H.J. Seifert, *Solid State Ionics,* **289**, 125 (2016).

[197] E. Zhao, F. Ma, Y. Guo and Y. Jin, *RSC Advances,* **6**, 92579 (2016).

[198] Y. Meesala, C.-Y. Chen, A. Jena, Y.-K. Liao, S.-F. Hu, H. Chang and R.-S. Liu, *The Journal of Physical Chemistry C,* **122**, 14383 (2018).

[199] Z. Zhang, S. Chen, J. Yang, G. Liu, X. Yao, P. Cui and X. Xu, *Electrochimica Acta,* **297**, 281 (2019).

Appendices

Appendix A: Spark Plasma Sintering of Lithium Aluminum Germanium Phosphate Solid Electrolyte and its Electrochemical Properties [§]

NASICON-type lithium aluminum germanium phosphate (LAGP) has attracted increasing attention as a solid electrolyte for all-solid-state lithium-ion batteries (ASSLIBs), due to the good ionic conductivity and highly stable interface with Li metal. However, it still remains challenges to achieve high density and good ionic conductivity in LAGP pellets by using conventional sintering methods because they required high temperatures (> 800 °C) and long sintering time (> 6 h), which could cause the loss of lithium, the formation of impurity phases, and thus the reduction of ionic conductivity. Herein, the utilization of a spark plasma sintering (SPS) method to synthesize LAGP pellets with a density of 3.477 g cm^{-3} was reported, a relatively high density up to 97.6%, and a good ionic conductivity of 3.29×10^{-4} S cm^{-1}. In contrast to the dry-pressing process followed with high-temperature annealing, the optimized SPS process only required a low operating temperature of 650 °C and a short sintering time of 10 min. Despite the least energy and short time consumptions, the SPS approach still could achieve LAGP pellets with high density, little voids and cracks, intimate grain-grain boundary, and high ionic conductivity. These advantages suggest the great potential of SPS as a fabrication technique for preparing solid electrolytes and composite electrodes used in ASSLIBs.

The utilization of rechargeable lithium-ion batteries (LIBs) has been increasingly expanded from consumer devices to plug-in or hybrid electric vehicles, and smart grid energy storage systems, in order to alleviate the dependence on fossil fuels, decrease greenhouse gas emissions, and realize clean transportation [155, 156]. However, traditional LIBs utilize liquid organic electrolytes that could cause catastrophic disasters (such as fire and explosion) upon exposure to the air, due to their flammable and volatile nature [157-159]. Moreover, the energy densities of current LIBs are gradually approaching their theoretical limits and cannot meet the increasing demands from end-users for higher-performance LIBs. From this aspect, all-solid-state lithium-ion batteries (ASSLIBs) have recently been revisited as promising next-generation battery systems because of their significantly improved energy density and safety [157, 160-162]. The major difference between ASSLIBs and conventional LIBs is the use of solid-state electrolytes (SSEs), rather than liquid organic electrolytes in the design and fabrication of battery systems. The adoption of SSEs not only can significantly reduce the safety risks associated with the flammable, volatile, and toxic liquid organic electrolytes, but also could potentially address Li dendrite growth problem and make it possible for the utilization of Li metal with a high theoretical capacity of 3860 mAh g^{-1} as the anode, therefore substantially elevating energy densities and the safety of ASSLIBs.

Among different kinds of SSEs, including garnet [163, 164], perovskite [165, 166], sulfides [167], hydrides [168], borate or phosphate [169-171], halides [172], LiPON [173], LISICON [174-177] and other Li-based ceramic [178], (NASICON)-typed sodium superionic conductor is one of the most popular solid electrolytes, due to its high ionic conductivity and good chemical and thermal stability with lithium anode [179-182]. In particular, lithium aluminum germanium phosphate (LAGP) has a NASICON-type structure and possesses several

advantages for materials preparation and practical applications in ASSLIBs. First, the high stability of LAGP SSEs against O_2 and H_2O means that the synthesis of materials and the assembly of batteries could be performed in an ambient atmosphere, therefore simplifying the manufacturing processes and requirements [157-159]. Secondly, the predominant ionic conductivities of LAGP SSEs are in the order of $10^{-3} – 10^{-5}$ S cm^{-1} at room temperature (RT), which are relatively high compared with other ceramic electrolytes [183, 184]. Thirdly, LAGP SSEs exhibit a large electrochemical stability window (1.8–7 V *vs.* Li$^+$/Li), good chemical compatibility with cathode materials at different charge states, and excellent interfacial stability towards Li metal anode [160, 185, 186]. Nevertheless, it was also reported that short-circuit occurred in SSEs because the deposited lithium grew along with voids among grains, and an effective approach to suppress lithium dendrites was to enhance the density and the mechanical strength of SSEs and create stable grain-grain interfaces in the solid electrolytes [187]. Therefore, it is imperative to develop methods to fabricate SSE pellets with high density and free of voids and through-holes. However, conventional sintering methods usually require high temperatures (> 800 °C) and long sintering time (> 6 h), which could easily result in grain coarsening, formation of impurity phases, and thus reduced ionic conductivity [188].

In recent years, spark plasma sintering (SPS) are attracting increasing attention from researchers to fabricate solid electrolytes and electrodes with densities close to their theoretical values in a short sintering time [189, 190]. During SPS processes, uniaxial force and pulsed direct electrical current are simultaneously applied to the powders and thus can rapidly consolidate the powders into dense pellets. The use of microscopic electrical current allows the sintering to complete in a few minutes because of the very high heating rates and the localized high temperatures between particles. In the meantime, the water-cooling system in SPS allows a

very high cooling rate. Compared to the conventional heat treatment, the effective heating and cooling systems in SPS enhanced the densification of SSE powders through grain diffusion mechanisms and avoided grain coarsening to maintain the intrinsic merits of nano-powders [191, 192]. Indeed, the SPS technique with the advantages of a flash and short processing time improves the sintering ability of various powder materials and creates intimate solid-solid interfaces in solid electrolytes and electrodes for ASSLIBs [184, 193].

In this work, high-densified LAGP pellets with high ionic conductivity of 3.29×10^{-4} S cm^{-1} was successfully produced by using SPS. Owing to the advantage of minimum energy and time consumptions of SPS, the highly-dense LAGP without microcracking resulted in the reduced resistance at grain boundaries, due to the removal of the pores/voids/cracks at a proper sintering temperature, thus improving the overall ionic conductivity of LAGP. At the same time, the low operating SPS temperature avoided the formation of nonconductive impurities, which usually appeared in the grain boundaries for traditionally high-temperature sintered samples, and resulted in blocking of Li-ion transport pathways.

Materials and Methods

LAGP powders with a stoichiometric formula of $Li1_{.5}Al_{0.5}Ge_{1.5}(PO_4)_3$ were placed in a graphite tooling (1 mm die) of the SPS chamber (Thermal Technologies 10-3 SPS system) and heated up to the target sintering temperature in an argon atmosphere. The SPS sintering pressure was 60 MPa, the sintering temperatures were changed from 600 °C to 750 °C, and the sintering time was varied between 1 min and 10 min for all the experiments. The SPS heating rate was set to 100 °C min^{-1}. Upon the completion of SPS sintering, the samples were cooled down to RT naturally. In addition to the SPS, LAGP pellets were also made by a conventional dry-pressing method, where 0.5 g of LAGP powders were placed into a stainless-steel die with 10 mm

diameter and pressed at 200 MPa for 2 min. The obtained pellets were then placed into a tube furnace and annealed at 800 °C for 6 h under a nitrogen atmosphere. The sintering process was done with the help of Anil Prasad at UBCO.

The phase structure of the starting LAGP powders and the LAGP pellets were characterized by X-ray diffraction (XRD, Bruker D8-Advance X-ray diffractometer) with Cu $K_{\alpha 1}$ & $K_{\alpha 2}$ radiation sources. The XRD test was done with the help of Anita Lam at the UBC Vancouver Chemistry Department. The LAGP microstructure was observed by field-emission SEM (Tescan MIRA3 FEG-SEM). The density of the LAGP pellets was measured by Archimedes' method. For ionic conductivity measurement, the surface of the LAGP pellets was first polished with sandpapers to remove carbon residual from the graphite die during the SPS process and then coated with 100-nm Au layers on both sides as blocking electrodes. Electrochemical impedance spectroscopy (EIS) test of Au-coated LAGP pellets was conducted on a Potentiostat/Galvanostat Station (Biologic VSP) in a frequency range of 0.1 Hz-1 MHz at different temperatures of –10 °C to 80 °C.
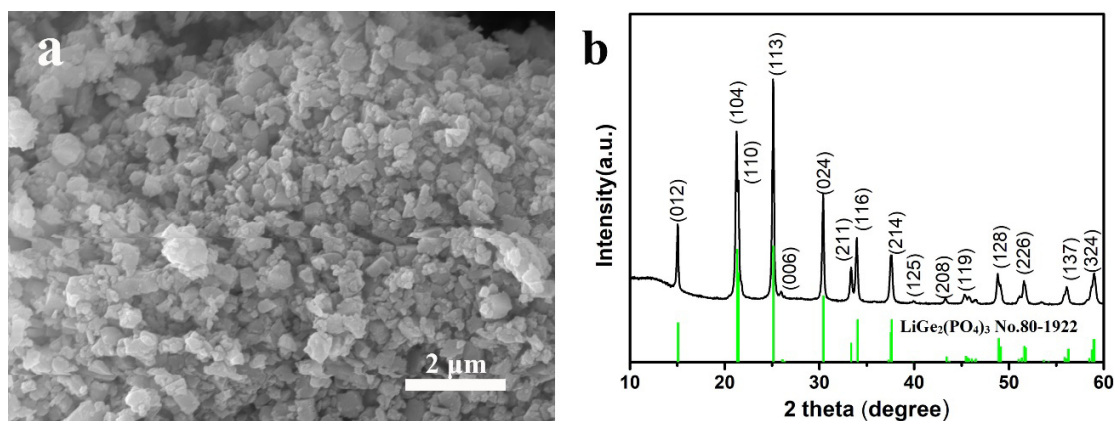
Results and Discussion

Figure A-1: (a) SEM image and (b) XRD pattern of LAGP powders.

As the starting material, LAGP powders were characterized by SEM for the morphology and by XRD for the phase structure, and the results are presented in Figure A-1. As shown in Figure A-1a, the diameter of LAGP particles is about 400 − 800 nm. The XRD pattern of LAGP powders (Figure A-1b) shows strong diffraction peaks, which could be well indexed to $LiGe_2(PO_4)_3$ with a NASICON-type structure (JCPDS PDF No. 80-1922). No other peaks of impurities are observed in the XRD pattern, indicating the high purity of the starting LAGP powders.
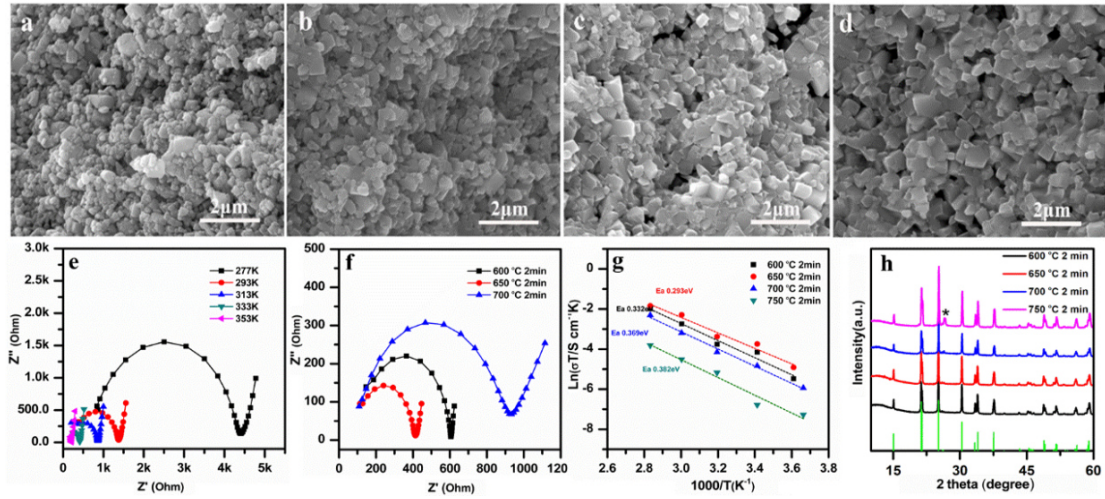

Figure A-2: SEM images at cross-sections of the LAGP pellets sintered by SPS for 2 min at (a) 600 °C, (b) 650 °C, (c) 700 °C, and (d) 750 °C; (e) Nyquist plots of the LAGP pellet sintered at 650 °C for 2 min; (f) Nyquist plots at RT, (g) Arrhenius curves, and (h) XRD patterns of LAGP pellets sintered by SPS for 2 min at 600 °C, 650 °C, 700 °C, and 750 °C.

The effects of SPS sintering temperatures (600 – 750°C) on the morphology, ionic conductivity, and phase structure of LAGP pellets were studied first. Figure A-2a-A-2d present the SEM images of the cross-sectional view of LAGP pellets sintered by SPS at different temperatures of 600 °C, 650 °C, 700 °C, and 750 °C for 2 min. It can be observed that the grain size in all the LAGP pellets is below 800 nm, similar to that of the starting LAGP powders (Figure A-1a). The LAGP grain size remains almost unchanged at sintering temperatures of 600

°C – 750 °C, due to the short SPS sintering time (2 min). As seen in Figures A-2a and A-2b, LAGP pellets fabricated at 600 °C and 650 °C are dense with minimal visible porosity. In contrast, the sample sintered at 700 °C in Figure A-2c exhibits enlarging pores at grain boundaries, and the one sintered at 750 °C in Figure A-2d possesses large cracks in the pellet's cross-section, as seen in Figure A-3. The high temperature at 750 °C possibly resulted in rapid grain growth, leading to the relatively high thermal expansion anisotropy of LAGP. Thus, the growing pores and voids likely coalesced and gradually emerged on the sample's surfaces.

The Nyquist plots of the LAGP pellets were measured by EIS, and fitted by using an equivalent circuit of $R_1(R_2 /\!/ CPE)W$ to obtain their ionic conductivities. As illustrated in Figures A-2e and A-2f, a typical Nyquist plot consists of one semicircle in the high-frequency region and a large spike in the low-frequency region. In general, the intercept of the high-frequency semicircle with the real axis stands for the total resistance of $R_2 = (R_{bulk} + R_{interface})$, where R_{bulk} and $R_{interface}$ represent the bulk resistance and grain-interface resistance, respectively. The spike in the low-frequency domain is known as Warburg diffusion impedance, which is due to the polarization resulting from Li-ion conduction at the electrolyte/Au electrode interface [194]. Figure A-2e shows one EIS example of LAGP sintered at 650 °C measured at different temperatures between –10 °C and 80 °C. The complex Nyquist plots of the LAGP pellets prepared between 600°C and 750 °C are shown in Figure A-2f. As supported by the SEM images (Figure A-2e, A-2d, and Figure A-3), the appearance of voids and cracks in the LAGP pellets sintered at high temperatures (700 °C and 750 °C) likely caused the increase in the resistance and the reduction in ionic conductivity.

The values of ionic conductivities can be determined from $\sigma = d/AR$, in which d and A stands for the thickness and the area of the pellet, respectively, and R is the total resistance (R_2)

obtained above, and the results are given in Figure A-2g. Among all the samples, the LAGP pellet sintered at 650°C for 2 min exhibited the highest conductivity of 8.09×10^{-5} S cm^{-1} at RT. The plots of *log(σT) vs. 1000/T* show a linear relation and fit well with the Arrhenius equation, *σ = A exp (-E$_a$/kT)*, in which *A*, *E$_a$*, and *k* represent the pre-exponential factor, the activation energy for conduction, and the Boltzmann constant, respectively. As seen from the Arrhenius plots (Figure A-2e), the slope of 650 °C sample is the lowest. The activation energies (*E$_a$*) are calculated from the rates of slopes, and 650 °C sample's *E$_a$* is 0.293 eV. In Figure A-2h, the XRD patterns of the SPS pellet sintered at different temperatures are given. All of the LAGP pellets sintered at 600 °C to 700 °C maintain pure NASICON-type phase (JCPDS PDF No. 80-1922). When the temperature increases to 750 °C, the peak intensity increases at 26.4°, which corresponds to the (006) crystal plane of the NASICON-type phase. This might be due to the reorientation of LAGP grains caused by the high pressure during the SPS process. For the whole heat treatment, the width of the diffraction peaks did not change, implying that the average crystallite size of LAGP remains unchanged.
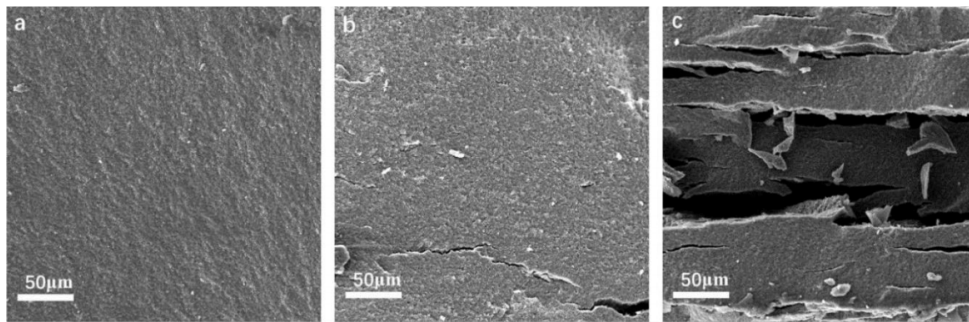

Figure A-3 : Low-magnification SEM images of SPS pellets sintered for 2 min at different temperatures of (a) 650 °C, (b) 700 °C, and (c) and 750 °C.

LAGP SSEs sintered by the SPS method could usually reach a very high density in relatively low temperatures (600 – 750 °C) and short time (2 min). The density of LAGP SSEs

sintered at 600 °C is 3.219 g cm^{-3}, as seen in Table 5. When the sintering temperature increases to 650 °C, the density increases up to 3.477 g cm^{-3}. However, when the temperature further elevates to 700 °C and 750 °C, the density decreases to 2.495 and 2.430 g cm^{-3}, respectively, most likely due to the formation of voids and microcracks in the pellets. The relative density of LAGP SSEs is determined to be 90.4%, 97.6%, 70.1%, and 68.2%, for the LAGP pellets sintered at 600 °C, 650 °C, 700 °C, and 750 °C, respectively. Therefore, the SPS sintering temperature is a key parameter to determine the density and ionic conductivity of LAGP pellets.

Table 5: Comparison of the measured densities and the relative densities of LAGP sintered by SPS method at different temperatures.

SPS sintering temperature (°C)	600	650	700	650
Measured density (g cm^{-3})	3.219	3.477	2.495	2.430
Relative density (%)*	90.4	97.6	70.1	68.2

*Note: Relative density = measured density/theoretical density × 100. LAGP has a theoretical density of 3.5615 g cm^{-3}.

The SEM images of LAGP pellets subjected to 650 °C SPS sintering temperature for different times from 1 min, 2 min, 5 min, to 10 min are shown in Figure A-4a to A-4d, respectively. The microstructure of LAGP starts to reorganize after 5 min of sintering due to the melting occurring at grain boundaries (Figure A-4c). Most of the LAGP particles are fully joined after 10 min of sintering, and a highly densified structure is finally obtained (Figure A-4d). SPS has a totally different densification mechanism compared to conventional heating treatment. During the SPS process, Joule heating was introduced at the physical contact points of different particles, causing localized heating and possibly melting to facilitate the densification of the LAGP powders [195].

The EIS results for the samples obtained at 650 °C for 10 min are presented in Figure A-

4e, and the Nyquist plots of the samples sintered at 650 °C with different SPS times are shown in Figure A-4f. It is obvious that the resistance of LAGP pellets decreases as the sintering time increases, as reflected by the reduction of the high-frequency semicircles in Figure A-4f. When the sintering time reaches 10 min, the LAGP pellet exhibits the highest ionic conductivity of 3.29×10^{-4} S cm^{-1} at RT. This result is consistent with the SEM microstructure observation (Figure A-4d), which discloses the melting of grain boundaries. The high densification and well-jointed grain boundaries reduce the total resistance of the LAGP pellets. The E_a calculation of the SPS samples processed at different times reveals that the 650 °C 10 min sample has a minimum E_a of 0.239 eV, suggesting the lowest diffusion barrier for Li-ions in SSEs. No impurity phases are detected in the XRD pattern for the LAGP pellet sintered at 650 °C for 10 min.
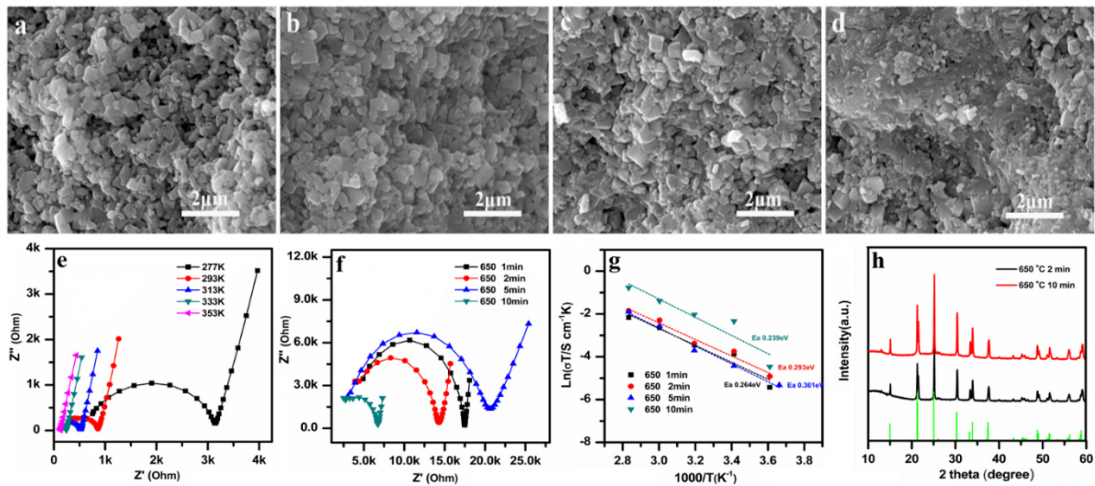

Figure A-4: SEM images at cross-sections of the LAGP pellets sintered at 650 ℃ for different sintering times: (a) 1 min, (b) 2 min, (c) 5 min, and (d) 10 min; (e) Nyquist plots of LAGP pellet (650 ℃, 10 min) measured at different temperatures; (f) Nyquist plots, (g) Arrhenius plots, and (h) XRD patterns of the LAGP fabricated at 650 ℃ for 2 min and 10 min.

In order to validate our sintering approach, it is necessary to investigate the impacts of the SPS compared with other conventional sintering methods. Therefore, the LAGP pellet was also synthesized by a dry-pressing method followed by heat treatment at 800 °C for 6 h, which was an optimal condition reported in a previous study [196]. Figures A-5a and A-5c show the SEM

124

images of the samples obtained using the conventional sintering approach. It can be seen that the grain size of conventionally-sintered LAGP pellet is in a range of 1.0 – 1.5 μm, which is much larger than that of SPS-sintered LAGP pellet (0.4 – 0.8 μm), as shown in Figure A-5b and A-5d.
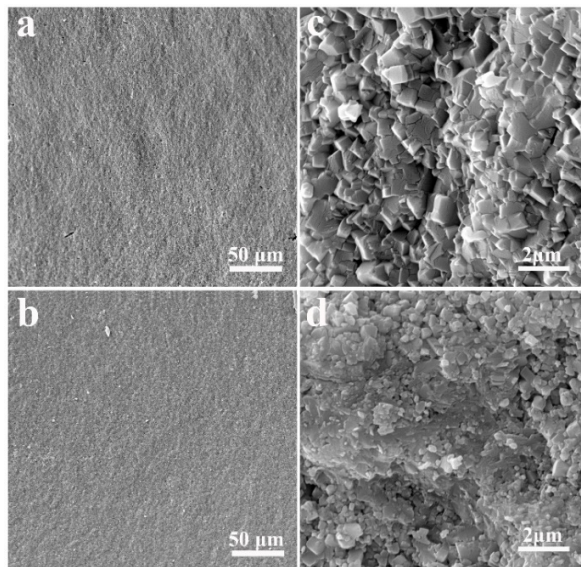

Figure A-5: Cross-sectional SEM images of (a, c) conventionally-sintered LAGP pellet and (b, d) SPS-sintered LAGP pellet.

Table 6 summarizes the correlations of preparation methods and conditions with the final density, relative density, ionic conductivity, and activation energy for LAGP SSEs. In conventional sintering approaches, high-temperature heat treatment is usually required to improve grain-grain interfaces and minimize grain-boundary resistance [185], [196-199]. While low-temperature annealing leads to a low ionic conductivity, such as glassy LAGP sample annealed at 500 °C, which is lower than its crystallization temperature. This showed that the glassy phase of LAGP is not a good Li-ion conductor as the crystallized one. However, two detrimental effects, *i.e.,* the loss of lithium and formation of second phases, are usually concurrent for high-temperature heat treatment and could cause the reduction of ionic conductivity in LAGP SSEs [185], [196-199]. In our optimal SPS process, the sintering

temperature is only 650 °C, which is much lower than other reported sintering methods, and yet the ionic conductivity remains high. Last but not least, the LAGP pellet fabricated by SPS possesses the highest relative density of 97.6% (Table 6).

Table 6: Summary of the density, relative density, ionic conductivity, and activation energy for LAGP pellets fabricated using different methods.

SSEs	Preparation method	Preparation condition	Density (g cm^{-3})	Relative density (%)	Ionic conductivity (S cm^{-1})	Activation energy (eV)	Ref.
$Li_{1.5}Al_{0.5}Ge_{1.5}(PO_4)_3$	hot press + post-calcination	600 °C, 1 h, 200 MPa + 800 °C, 5h	3.33	93.5	1.64×10^{-4}	0.299	[185]
$Li_{1.3}Al_{0.3}Ge_{1.7}(PO_4)_3$	dry-pressing + post-calcination	5 min, 20 MPa + 750°C, 5 h	3.18	89.3	3.4×10^{-4}	0.330	[197]
$Li_{1.70}Al_{0.61}Ge_{1.35}P_{3.04}O_{12.0}$	cold press + sintering	800°C, 6 h	3.02	84.8	2.3×10^{-4}	0.320	[196]
$Li_{1.31}Al_{0.42}Ge_{1.52}P_{3.09}O_{12.1}$	quenched glass piece + sintering	500°C, 1 h	3.08	86.5	Too low to be measured	N/A	[196]
$Li_{1.5}Al_{0.5}Ge_{1.5}(PO_4)_3$	melt-quench + post crystallization	800 °C, 8 h	N/A	N/A	5×10^{-4}	0.280	[198]
$Li_{1.5}Al_{0.5}Ge_{1.5}(PO_4)_3$	cold press + sintering	200 MPa + 850 °C, 5 h	N/A	N/A	2.99×10^{-4}	N/A	[199]
$Li_{1.5}Al_{0.5}Ge_{1.5}(PO_4)_3$	SPS	650 °C, 10 min, 100 MPa	3.48	97.6	3.29×10^{-4}	0.239	This work

N/A: not available.

In summary, highly densified LAGP pellets were fabricated by using the SPS technique and exhibited high ionic conductivity at room temperature. The influences of SPS sintering temperatures (600 – 750 °C) and times (1–10 min) on the microstructure, density, and ionic conductivity of the LAGP pellets were studied in detail. It can be concluded that the optimal SPS condition for LAGP pellets was 650 °C and 10 min, and the synthesized LAGP pellets are dense with minimal visible porosity. The density of the LAGP pellets is as high as 3.477 g cm^{-3}, a relative density of 97.6%, and the ionic conductivity is 3.29×10^{-4} S cm^{-1}, with an activation energy of 0.239 eV at RT. Sintering temperatures higher than 650 °C caused the formation of

voids and microcracks in the LAGP pellets, negatively affecting the density and ionic conductivity. These results clearly demonstrate that the potential of the SPS approach to synthesize solid electrolytes used in ASSLIBs, owing to the drastic reduced sintering temperature and time compared to conventional sintering processes. The SPS technique could be further expanded to develop Si/LAGP composite anode for all-solid-state lithium-ion batteries.

Appendix B:

Permission from IOP Publishing for Published Article

Published article: <u>Hongzheng Zhu,</u> Mohammad Hossein Aboonasr Shiraz, Liang Liu, Yuhai Hu, Jian Liu. Facile and Low-Cost Al_2O_3 Coating as an Artificial Solid Electrolyte Interphase Layer on Graphite/Silicon Composites for Lithium-Ion Batteries. *Nanotechnology*, Volume 32, Number 14, 144001, 2021 (https://iopscience.iop.org/article/10.1088/1361-6528/abd580)

Upon transfer of copyright, IOP and/or the copyright owner grants back to authors a number of rights. <u>These include the right to include the Final Published Version of the article in your research thesis or dissertation.</u> Please include citation details and, for online use, a link to the Version of Record. IOP's permission will be required for commercial use of an article published as part of your thesis. IOP does not allow ProQuest to publish or sell the article as part of your dissertation.

(Source: https://publishingsupport.iopscience.iop.org/permissions-faqs/)

Permission from Royal Society of Chemistry (RSC) for Published Article

Published article: <u>Hongzheng Zhu</u>, Mohammad Hossein Aboonasr Shiraz, Lu Yao, Keegan Adair, Zhiqiang Wang, Huan Tong, Xueyang Song, Tsun-Kong Sham, Mohammad Arjmand, Xiping Song and Jian Liu. Molecular-Layer-Deposited tincone: a New Hybrid Organic-Inorganic Anode Material for Three-Dimensional Microbatteries. *Chemical Communications*, Volume 56, 13221, 2020. (https://pubs.rsc.org/en/content/articlelanding/2020/cc/d0cc03869e#!divAbstract)

Material published by the Royal Society of Chemistry (RSC) and other publishers is subject to all applicable copyright, database protection and other rights. The graphic below outlines the steps to obtain permission to reuse RSC materials, where required:

(Source: https://www.rsc.org/journals-books-databases/journal-authors-reviewers/licences-copyright-permissions/#deposition-sharing)
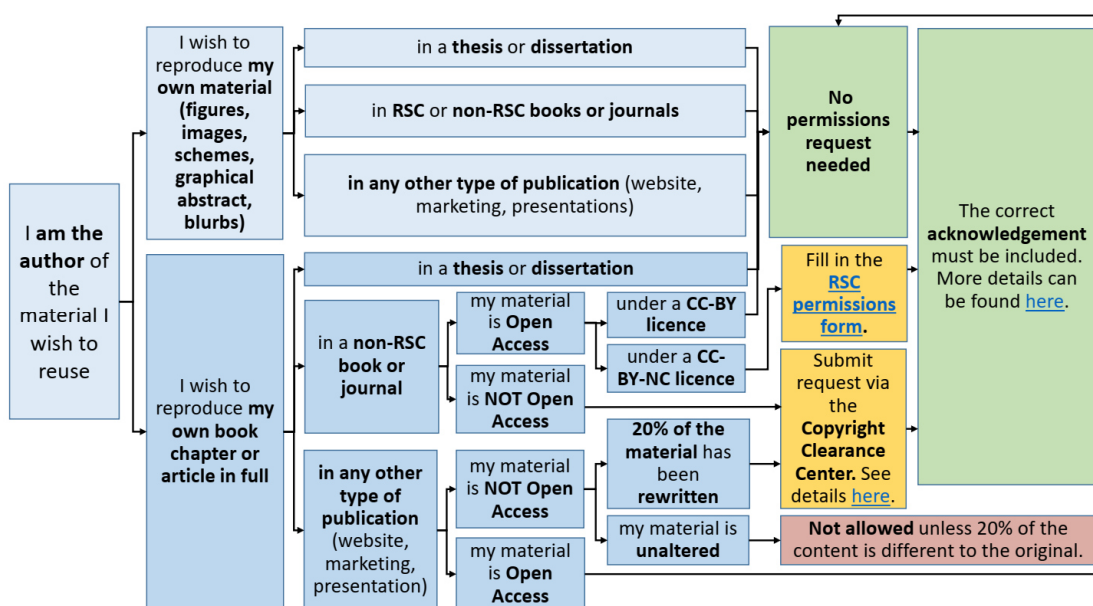
Permission from MDPI Journals for Published Article

Published article: <u>Hongzheng Zhu</u>, Anil Prasad, Somi Doja, Lukas Bichler and Jian Liu. Spark Plasma Sintering of Lithium Aluminum Germanium Phosphate Solid Electrolyte and its Electrochemical Properties. *Nanomaterials*, Volume 9, Issue 8, 2019

Permission from Elsevier for Published Article

Published article: <u>Hongzheng Zhu</u>, Jian Liu. Emerging applications of spark plasma sintering in all solid-state lithium-ionbatteries and beyond. *J. Power Sources* 2018, 391, 10-25. (Special Issue: Solid State Batteries: From Fundamentals to Applications)

Permission guidelines: For further guidelines about obtaining permission, please review our Frequently Asked Questions below:

Can I include/use my article in my thesis/dissertation? Yes. <u>Authors can include their articles in full or in part in a thesis or dissertation for non-commercial purposes.</u>

(Source: https://www.elsevier.com/about/policies/copyright/permissions)

Appendix C: Permissions from publishers to reuse figures/tables in thesis/dissertation

- **Elsevier-Ref. #3** J. Xu, S. Dou, H. Liu and L. Dai, *Nano Energy,* **2**, 439 (2013).

License Number	5115990767797
License date	Jul 25, 2021

☑ Licensed Content

Licensed Content Publisher	Elsevier
Licensed Content Publication	Nano Energy
Licensed Content Title	Cathode materials for next generation lithium ion batteries
Licensed Content Author	Jiantie Xu,Shixue Dou,Huakun Liu,Liming Dai
Licensed Content Date	Jul 1, 2013
Licensed Content Volume	2
Licensed Content Issue	4
Licensed Content Pages	4

- **Springer Nature-Ref. #4** S. Zhang, *npj Computational Materials,* **3**, 1 (2017).

Chemomechanical modeling of lithiation-induced failure in high-volume-change electrode materials for lithium ion batteries

SPRINGER NATURE

Author: Sulin Zhang
Publication: npj Computational Materials
Publisher: Springer Nature
Date: Feb 17, 2017

Copyright © 2017, The Author(s)

Creative Commons

This is an open access article distributed under the terms of the Creative Commons CC BY license, which permits unrestricted use, distribution, and reproduction in any medium, provided the original work is properly cited.

You are not required to obtain permission to reuse this article.

To request permission for a type of use not listed, please contact Springer Nature

- **Springer Nature-Ref. #18** J.W. Choi and D. Aurbach, *Nature Reviews Materials,* **1**, 1 (2016).

License Number	5116001343492
License date	Jul 25, 2021

☑ Licensed Content

Licensed Content Publisher	Springer Nature
Licensed Content Publication	Nature Reviews Materials
Licensed Content Title	Promise and reality of post-lithium-ion batteries with high energy densities
Licensed Content Author	Jang Wook Choi et al
Licensed Content Date	Mar 31, 2016

- **IOP Publishing-Ref. # 26** J. Liu and X. Sun, *Nanotechnology,* **26**, 024001 (2014).

Order Details

1. Nanotechnology

Billing Status: Open

Order License ID	1135755-1
Order detail status	Completed
ISSN	0957-4484
Type of use	Republish in a thesis/dissertation
Publisher	IOP Publishing
Portion	Chart/graph/table/figure

0.00 CAD
Republication Permission

LICENSED CONTENT

Publication Title	Nanotechnology	Country	United Kingdom of Great Britain and Northern Ireland
Author/Editor	Institute of Physics (Great Britain)		
Date	01/01/1990	Rightsholder	IOP Publishing, Ltd
Language	English	Publication Type	Journal

- **Beilstein-Institut-Ref. # 41** P. Sundberg and M. Karppinen, *Beilstein journal of nanotechnology,* **5**, 1104 (2014)

- **Wiley Ref. # 48** D.M. Piper, J.J. Travis, M. Young, S.B. Son, S.C. Kim, K.H. Oh, S.M. George, C. Ban and S.H. Lee, Advanced Materials, 26, 1596 (2014)

License Number	5116270444623
License date	Jul 25, 2021
☑ Licensed Content	
Licensed Content Publisher	John Wiley and Sons
Licensed Content Publication	Advanced Materials
Licensed Content Title	Reversible High-Capacity Si Nanocomposite Anodes for Lithium-ion Batteries Enabled by Molecular Layer Deposition
Licensed Content Author	Daniela Molina Piper, Jonathan J. Travis, Matthias Young, et al
Licensed Content Date	Dec 18, 2013
Licensed Content Volume	26
Licensed Content Issue	10
Licensed Content Pages	6

- **American Chemical Society-Ref. #53** N. Ogihara, Y. Itou, T. Sasaki and Y. Takeuchi, *The Journal of Physical Chemistry C,* **119**, 4612 (2015)

Impedance Spectroscopy Characterization of Porous Electrodes under Different Electrode Thickness Using a Symmetric Cell for High-Performance Lithium-Ion Batteries

ACS Publications
Most Trusted. Most Cited. Most Read.

Author: Nobuhiro Ogihara, Yuichi Itou, Tsuyoshi Sasaki, et al
Publication: The Journal of Physical Chemistry C
Publisher: American Chemical Society
Date: Mar 1, 2015

Copyright © 2015, American Chemical Society